SANDIA REPORT

SAND2006-7028
Unlimited Release
Printed December 2006

Modeling of Friction-Induced Deformation and Microstructures

Somuri V. Prasad, Joseph R. Michael, Bhaskar S. Majumdar, Corbett C. Battaile, Neville R. Moody, Megan J. Cordill, John M. Jungk, and Doug J. Bammann

Sandia National Laboratories

Modeling of Friction-Induced Deformation and Microstructures

Somuri V. Prasad (01824), Joseph R. Michael (01822), Bhaskar S. Majumdar (New Mexico Institute of Mining and Technology), Corbett C. Battaile (01814), Neville R. Moody (08758), Megan J. Cordill (University of Minnesota), John M. Jungk (01824), Doug J. Bammann (08776)
Sandia National Laboratories
P.O. Box 5800
Albuquerque, New Mexico 87185-MS 0889

Abstract

Frictional contact results in surface and subsurface damage that could influence the performance, aging, and reliability of moving mechanical assemblies. Changes in surface roughness, hardness, grain size and texture often occur during the initial run-in period, resulting in the evolution of subsurface layers with characteristic microstructural features that are different from those of the bulk.

The objective of this LDRD funded research was to model friction-induced microstructures. In order to accomplish this objective, novel experimental techniques were developed to make friction measurements on single crystal surfaces along specific crystallographic surfaces. Focused ion beam techniques were used to prepare cross-sections of wear scars, and electron backscattered diffraction (EBSD) and TEM to understand the deformation, orientation changes, and recrystallization that are associated with sliding wear. The extent of subsurface deformation and the coefficient of friction were strongly dependent on the crystal orientation. These experimental observations and insights were used to develop and validate phenomenological models.

A phenomenological model was developed to elucidate the relationships between deformation, microstructure formation, and friction during wear. The contact mechanics problem was described by well-known mathematical solutions for the stresses during sliding friction. Crystal plasticity theory was used to describe the evolution of dislocation content in the worn material, which in turn provided an estimate of the characteristic microstructural feature size as a function of the imposed strain. An analysis of grain boundary sliding in ultra-fine-grained material provided a mechanism for lubrication, and model predictions of the contribution of grain boundary sliding (relative to plastic deformation) to lubrication were in good qualitative agreement with experimental evidence.

A nanomechanics-based approach has been developed for characterizing the mechanical response of wear surfaces. Coatings are often required to mitigate friction and wear. Amongst other factors, plastic deformation of the substrate determines the coating-substrate interface reliability. Finite element modeling has been applied to predict the plastic deformation for the specific case of diamond-like carbon (DLC) coated Ni alloy substrates.

(This page involuntarily left blank.)

Table of Contents

List of Figures

6

List of Tables

1. Introduction and Background

Tribological issues (e.g. friction, wear and lubrication) play a dominant role in governing the performance and reliability of moving mechanical systems involving contacting sliding surfaces. In view of their high surface to volume ratio, tribological problems become even more predominant in microelectromechanical systems, MEMS. The properties of bulk materials are often used for the design of mechanical components, and for predicting the long-term performance and reliability of the assembled system. However, in ductile materials, sliding contact is often accompanied by severe plastic deformation localized to a small volume of material adjacent to the surface. This results in changes in the surface roughness, hardness, grain size and texture during the initial "run-in" period culminating in the evolution of a subsurface layer with characteristic features [1.1]. Tribology is therefore a systems property involving at least two surfaces that come into sliding contact and the environment. Once the steady state is reached, the contacts are predominantly amongst the wear surface with friction-induced substructures, transfer film on the counterface and the wear debris, as shown schematically in Fig. 1.1.

Our previous research on electron backscattered diffraction (EBSD) analysis of wear scar cross-sections on electroplated nickel showed bending of columnar grains in the direction of sliding [1.2], and at higher contact pressures, formation of nanocrystalline zones have been observed. Clearly, it is this friction-induced subsurface layer, whose microstructure is determined by the combined effects of the bulk microstrucure and the operating conditions, that controls the friction, evolution of wear debris, and coating-substrate interface reliability.   It is therefore important to understand the friction-induced microstrucural changes and also the manner in which the microstructure is modified by interaction with the environment (e.g. oxidation) or by mechanical mixing. In FY2004, a three-year LDRD project was initiated to gain a fundamental understanding of the phenomena governing the formation of friction-induced substructures in metallic materials, and use this knowledge to model the friction-induced deformation and microstructure. The results of this LDRD project are given in this SAND report.
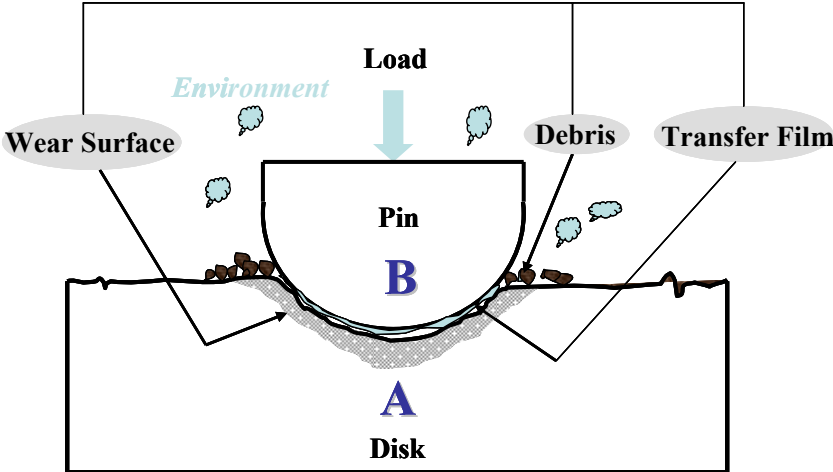
Figure 1.1. Schematic illustration of a tribological contact showing friction-induced subsurface, transfer film and wear debris.

We proposed to develop novel experimental techniques for tribological evaluation and microstructural characterization in regimes relevant to microsystems operation, and use the data to guide and validate the modeling efforts. The first phase of this project was focused on friction induced microstructural changes in single crystals. We used this study to understand the origin of the evolution of dislocations, low angle grain boundaries, high angle grain boundaries and wear debris generation. In order to accomplish this objective, we developed novel experimental techniques to make friction measurements on single crystal surfaces along specific crystallographic directions; these are described in Chapter 2. These results were interpreted by analyzing the stress fields under the sliding indenter, and their relationships to the slip system geometries (Chapter3). With the help of focused ion beam microscopy we were able to prepare cross sections of wear scars generated on single crystal Ni surfaces along specific crystallographic directions. The evolution of friction-induced recrystallization and grain structures as a function of crystallography and contact stress has been analyzed by EBSD and transmission electron microscopy (Chapter 4). We developed a numerical model of the plastic deformation, microstructure formation, and friction evolution during sliding contact. The model is sensitive to crystallographic effects, and provides insight into the relationships between friction and microstructure in the context of grain boundary sliding in ultra-fine-grained material. Nanomechanics-based approach was developed to analyze the mechanical response of wear surfaces (with friction-induced substructures). This approach has been applied to both single crystals (Chapter 6) and electrodeposited materials with strong crystallographic texture (Chapter 7). Tribological coatings are often required to mitigate friction between metallic contacts. The final phase of this study was directed to model the role of substrate deformation on substrate-coating interface reliability. Finite element modeling (with FIB microscopy validation) was used for the specific case of diamond-like carbon coating on Ni alloy substrates to estimate friction-induced substrate deformation and how this would influence on the tribological behavior of the coated material (Chapter 8).

2. Techniques for the Visualization of Friction-Induced Microstructural Changes

2.1. Introduction

There have been many studies that have characterized the sub-surface microstructural changes resulting from sliding wear. These studies generally rely on transmission electron microscopy (TEM) as a tool for the characterization of the deformed material below the wear scar. Preparation of samples from the desired location on the sample through either electropolishing or broad beam ion milling is difficult and very time consuming and more often than not, not successful. This is due primarily to the lack of final sample location specificity using techniques like electropolishing and broad beam ion milling. As part of the current study, electron backscatter diffraction (EBSD) and automated orientation mapping was to be used to characterize the degree of sub-surface deformation that was associated with the sliding wear. The small size of the wear scars generated in this study made the use of metallographic techniques inappropriate. In this section we discuss the development of techniques that allow samples to be prepared in cross section from precise locations. In addition, we will discuss how these samples are applicable to correlative analysis via scanning electron microscopy, EBSD and TEM.

2.2. Sample Requirements for TEM and EBSD

The first and foremost requirement for TEM and EBSD analyses is the sample preparation. First, the sample must be representative of the bulk materials. The best samples for TEM are very thin to allow the electrons to penetrate trough the sample and to be collected to form an image. Also, thinner samples allow higher spatial resolution microanalytical information to be collected. The sample preparation technique should not substantially modify the sample and should not introduce detectable amounts of deformation or surface damage. EBSD has similar requirements for samples. EBSD relies on the diffraction of electrons from near surface regions of the sample. If these surface layers are damaged by sample preparation, the diffraction patterns will be reduced in quality or be made entirely invisible. Also, sample preparation induced deformation may mask the deformation induced by wear testing. EBSD orientation maps have been almost exclusively obtained from metallographically prepared bulk samples. Use of bulk samples has limited the spatial resolution of EBSD to about 100 nm. The use of thin samples allows better spatial resolution which can approach 10 nm in Ni. Resolution is important for the study of wear scars as the worn regions may have grain sizes that approach the nm scale.

2.3. Focused Ion Beam Sample Preparation

Focused ion beam systems (FIB) have been used for the past few years to produce site specific samples for both SEM and TEM analysis. The recent combination of SEM with FIB allows precise sample areas to be targeted for preparation with FIB. The interaction of energetic ions with matter can result in materials removal via sputtering. In the FIB, the ion beam is highly focused and can be controlled to remove material in very specific local areas. Cross sections for simple SEM imagining can be prepared very quickly by using the ion beam to remove material to expose a cross section of the surface. Site specific samples for TEM are prepared by milling two stair step trenches leaving a thin free standing membrane that is thin and ideal for TEM imaging and analysis. FIB sample preparation of wear scars was demonstrated recently [2.1]. Figure 2.1a shows a schematic of the FIB process for producing thin samples. Figure 2.1b shows a typical wear scar for this study and the location of the thin membrane prepared by FIB before it was extracted and mounted on a TEM support film.

The preparation of cross sections for SEM or TEM involves a number of steps. First, the stair step trenches are milled using large ion beam currents. The large ion beam currents allow fast material removal rates, but the associated beam size does not produce good sections. After the stair step trenches are milled, then a line raster is used which is sequentially advanced into the cross section. During the process, lower beam currents are utilized to produce better polished surfaces and the electron beam is used to monitor the polishing process and to determine when to stop at the desired section position. Generally, the samples produced are about 20-40 µm in length and 10 µm deep.

EBSD requires samples with surfaces that are clean and free of sample preparation related deformation. An example of how poorly EBSD works on wear scars is shown in Figure 2.2. Figure 2.2a shows an SEM image wear the forward scattered electron signal has been used to form an image. Here EBSD orientation data was taken across the surface of a wear scar (plan view).   EBSD works by taking diffraction patterns pixel-by-pixel across the area to be mapped. For each pixel the diffraction pattern is indexed and the orientation of the crystal calculated. If the diffraction patterns are poor the system will not be able to index the pattern and this is indicated by a black pixel in the displayed map. Note in Figure 2.2b that the wear scar itself is black indicating that there were very few pixels that could be successfully indexed. In selected materials FIB has been shown to produce samples with these characteristics.[2.2] The geometry EBSD requires demands that a thin sample similar to those used for TEM be prepared. This study has demonstrated that EBSD of FIB prepared Ni samples are suitable for analysis with EBSD. A typical EBSD orientation map of a FIB prepared cross section of a wear scar is shown in Figure 2.3. Figure 2.3a shows band contrast map. This image scales the quality of the individual EBSD patterns to a gray level. These images are quite useful for visualizing the microstructure of an orientation map. Figure 2.3b shows the corresponding orientation map of the same area as shown in Figure 2.3a. Note that the EBSD system can now map the sub-surface deformation that has been induced by sliding wear. Thus, FIB preparation of thin samples allows TEM imaging and analysis and EBSD orientation mapping to be obtained from identical areas of a sample providing complimentary information.

Ion imaging of deformed or polycrystalline samples can provide very important information through channeling contrast imaging (CCI). In this imaging mode the secondary electrons generated by the ions are used to form an image. As ions tend to channel more strongly in specific crystallographic directions than do electrons, small changes in orientation (channeling contrast can be sensitive to changes in orientation of less than 1 degree) are readily observed as changes in signal level. Figure 2.3 shows an example of a channeling contrast image from a cross section of a worn single crystal Ni surface. Although these images do show the deformation that has occurred they are not quantitative and very little quantitative information can be inferred from the gray levels present in the image.

2.4. Orienting and Marking of Ni Single Crystals

In order to perform tribological measurements in specific directions on single crystals, the crystals must be appropriately marked. In this study a novel technique has been developed to orient and mark Ni single crystals to allow wear tests to be conducted in specific crystallographic directions. The dual beam FIB used in this study is equipped with an EBSD system. The Ni single crystals were mounted in the FIB and the SEM and the EBSD system were used to determine the orientation of the single crystal. Once the orientation of the single crystal was known, the FIB was used to write these directions on the surface of the single crystal, large enough to be easily recognized in an optical microscope to allow the wear test to be conducted correctly. These marks are used for alignment of the single crystals for wear testing. The constraints imposed by crystallography allow only certain crystallographic directions to exist parallel to the surface of the Ni single crystals. For a direction to lie in the plane of the single crystal surface, the dot product between the surface normal and the direction must be equal to 0. Thus, for a {001} single crystal only directions of the type <UV0> will lie in the plane of the surface. Similarly, for a {111} single crystal, directions of the type <-U U 0> or any direction in which U + V is equal to −W and for a {110} single crystal <U −U W>.
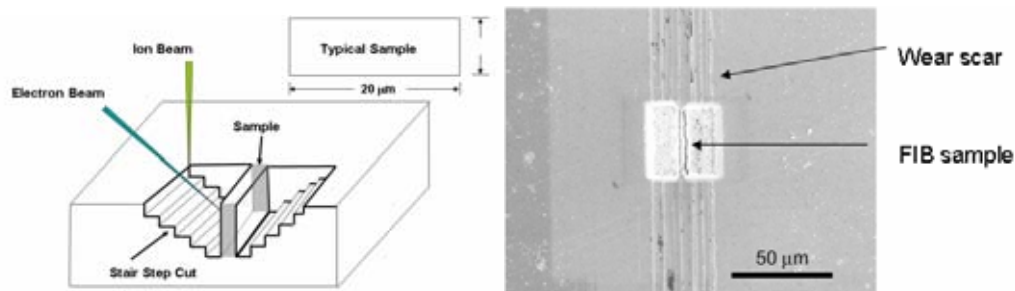
Figure 2.1. FIB method for producing thin samples from wear scars. a) Schematic of the milling steps required. b) Example of FIB cross section prepared from a wear scar.
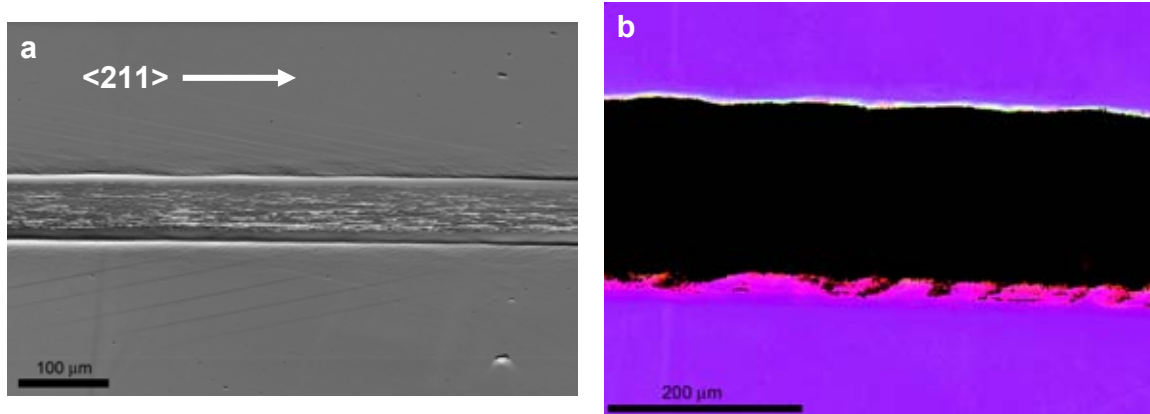
Figure 2.2. SEM and EBSD maps of the surface of a wear scar in a {111} single crystal (plan view). a) Forward scattered electron image of the wear scar. b) EBSD map that demonstrates the inability of the technique to obtain good diffraction patterns from the surface of the wear scar due to the deformation present.
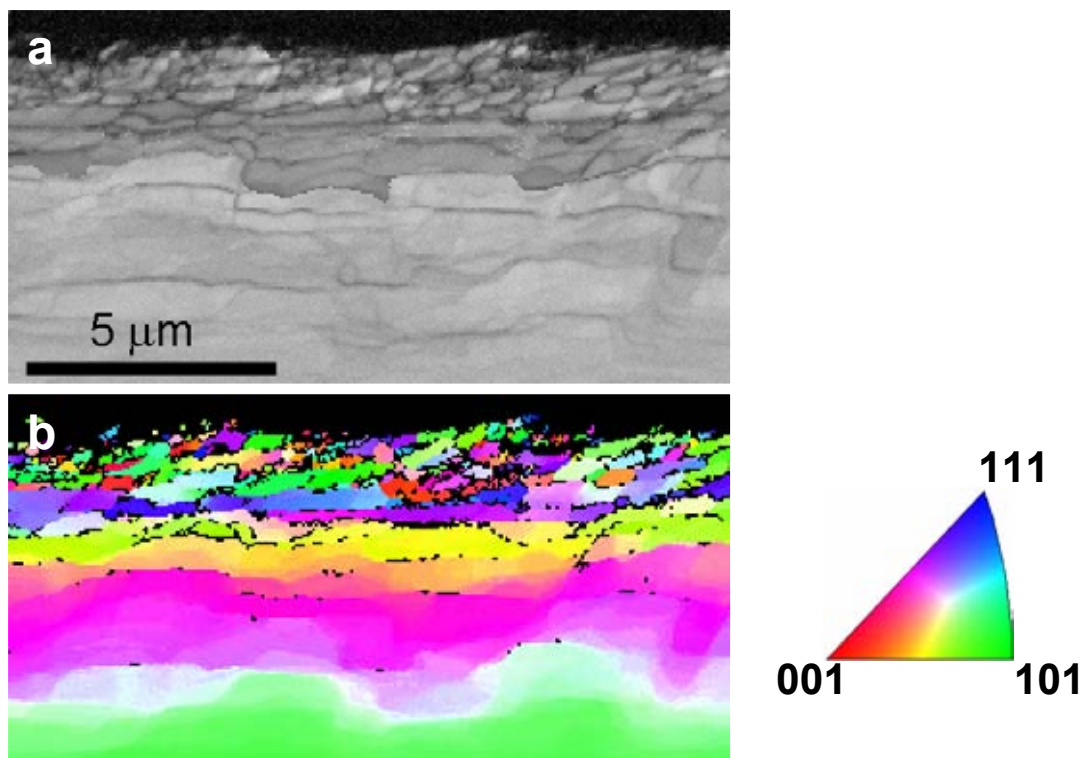
Figure 2.3. EBSD of FIB prepared cross section of the wear scar shown in Figure 2.2. a) Band contrast image produced from the quality of the EBSD patterns at each pixel, b) EBSD orientation map color coded with respect to the normal to the sliding direction. The colors represent directions as shown by the stereographic triangle to the right.

2.5. Rotary Module for Tribometer

The issues become complex in single crystals while attempting to make wear tracks in specific crystallographic directions. Most commercial pin-disc machines do not have the provision to accurately orient the crystals along specific crystallographic directions marked by the EBSD/FIB techniques described above. A rotary stage module was designed and built for this purpose (Fig. 2.4a). The module consists of a chuck for holding the crystal in place and a rotary stage for aligning the crystal surface with an accuracy of ± 0.5 °. The crystal was first fixed in the chuck and the whole rotary stage assembly was viewed in a low-powered optical microscope. The crystal was rotated till a particular crystallographic (FIB) marking (e.g. 001) is aligned in a specific direction on the rotary stage. The stage is locked before inserting into the tribometer. The module is designed in such a way that when the rotary stage is inserted into the tribometer, this particular crystallographic direction will be parallel to the load arm.

Friction measurements were made using a ball-on-disk linear wear tester. To avoid environmental reactions, the tribometer was housed in an environmental chamber (Figure 2.5). Tests were performed in unidirectional sliding mode. Oxygen content in the chamber was measured using a Delta F Platinum Series oxygen monitor, and the humidity was monitored by measuring the dew point. Tests were conducted in dry nitrogen (<1% RH, <10 ppm O_2 and <100 ppm H_2O environment with a 3.175 mm diameter Si_3N_4 (Cerbec) ball. Normal loads (L) were applied by deadweights. A 500mN transducer (Sensotec) in the load arm measured the tangential (friction) force (W) over a track distance of 1.6 mm, which was dependent on the size of the test coupon. The sliding speed was 3.7 mm/s. The ratio of tangential to normal load is the coefficient of friction (COF).
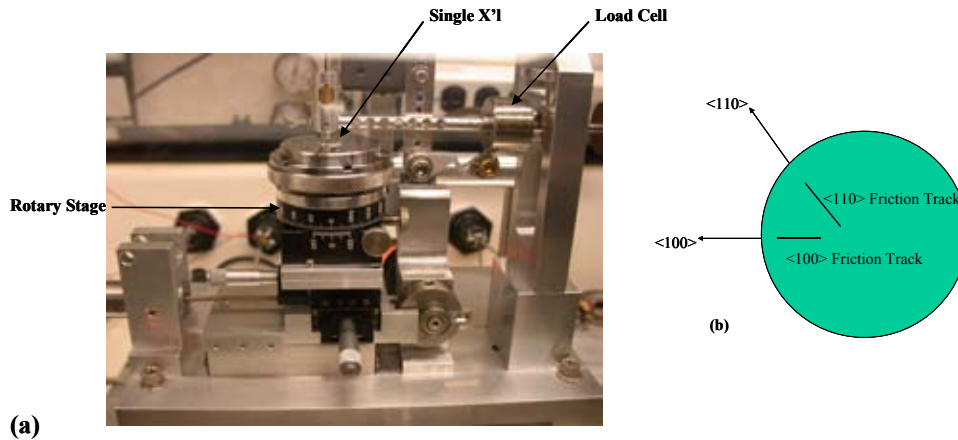
Figure 2.4. (a) Rotary stage for alignment of single crystals, (b) Schematic illustration of friction track orientations on (100) surface in two crystallographic directions: <100> and <110>. The crystal has a <001> normal to the polished surface.
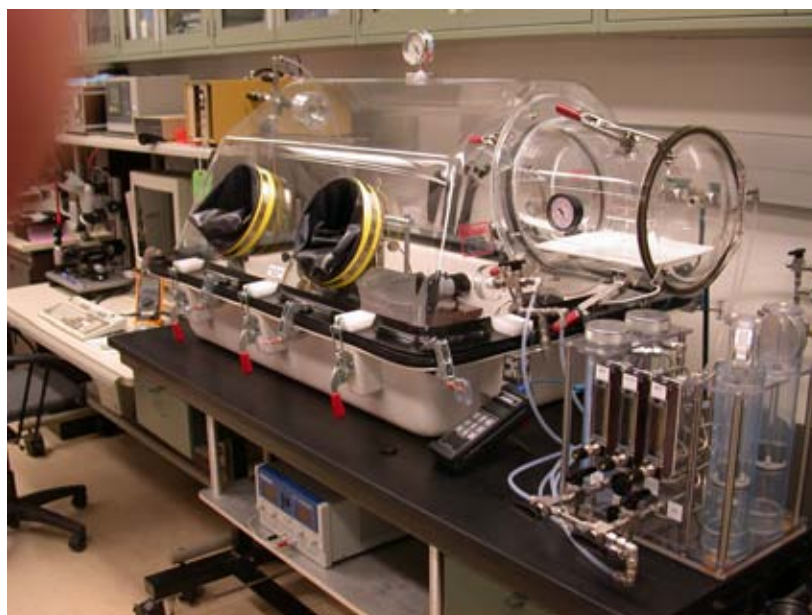
Figure 2.5. Environmental chamber for the tribometer.

3. Plastic Slip in Single Crystals Under a Sliding Indenter

3.1. Introduction

Before attempting an interpretation of the experimental evidence, it is useful to perform an analysis of the mechanical response of the worn material. Under the action of frictional contact, the material immediately adjacent to the area of contact is subjected to localized plastic deformation. Understanding the deformation behavior beneath a sliding indenter is crucial to modeling the friction-induced microstructures. The focus of this chapter is on the mechanics of slip, and how crystal orientation plays a role in determining the depth of slip and the evolution of near surface microstructure. As will be discussed in Chapter 4, the friction coefficient, μ, tends to evolve with the number of contact cycles for certain crystallographies, and reflects changes in surface morphology and microstructure associated with this deformation process. While the initial increase in friction coefficient may be associated with break down of surface asperities leading to greater adhesion through plastic deformation, it is the evolution of μ after the attainment of the peak value that is of significant interest. This evolution must be associated with changes in the sub-surface microstructural conditions, consisting either of characteristic dislocation substructures, crystal rotations and texturing, and possible recrytallization and grain growth.

While the literature on wear is voluminous, relatively few studies have concentrated on texture changes and crystal rotations immediately below a sliding indenter. Farhat et al [3.1] conducted texture measurements of polycrystalline Al samples, and showed that grains near the indenter tended to take on a texture, with a substantial number of grains oriented such that their <111> (slip-plane normal) directions were aligned along the surface normal of the specimen. Wheeler and Buckley [3.2] observed that in a polycrystalline fcc alloy, the <111> plane normals were tilted about 10 degrees towards the sliding direction. Similar behavior was observed in stainless steel and Al by Hirth and Rigney [3.3]. Farhat [3.1] observed that the friction coefficient did not decrease for a Ti alloy that had a basal texture, i.e., when the (0001) plane was parallel to the specimen surface. On the other hand, there was appreciable decrease in μ for prismatic texture, i.e., when the prismatic $(1\bar{1}00)$ plane was preferentially oriented parallel to the surface. In this regard, it may be noted that the slip system for Ti-alloys is principally $(1\bar{1}00)[11\bar{2}0]$, so that a high resolved shear stress can be obtained with prismatic texture. The effect of crystal orientation was also observed by Gwathmey at al. [3.4], who observed that μ between the sliding (100) faces of a two Cu crystals was significantly larger than the case of rubbing (111) faces.

All these studies indicate that the initial crystal orientation can have a significant effect on μ and wear rates. In particular, a slip plane closely parallel to the sliding surface, such that the slip plane has a high resolved shear stress (τ_{rss}), appears to produce a low final value of μ. This orientation may evolve through texture changes near the surface, or it may be present initially. However, this scenario may not be the complete story. For example, if two slip systems are

equally stressed to a high level, and if the systems produce strongly intersecting slip, then it is possible that easy shear can be terminated. Recalling that $\mu = F_S/F_N$, where F_N is the normal load and F_S is the shear load, an increasing value of F_S will act to retain a high value of μ, i.e., the top curve in Figure 3.1. A second possibility is that a large amount of shear strain near the surface, particularly under easy shear conditions (Stage I of work hardening), can lead to formation of fine dislocation substructures and possibly recrystallization of small or nano-sized grains. The associated grain boundaries can act as excellent sources and sinks for vacancies, and thereby can promote deformation through grain boundary sliding of the new nano-sized grains. Grain boundary sliding (without formation of cracks) requires the macroscopic motion of atoms, which in turn requires the reverse movement of vacancies (similar to Coble creep). These vacancies move from one part of the boundary to another (in particular from regions that have a high tensile mean stress to those that have a low or even negative mean stress), and this can only occur if the grain boundary acts as perfect source or sink for vacancies; otherwise sliding is stopped. Rather than vacancy concentration (which is largely dictated by temperature), the more important parameter is the rate of vacancy migration. If the boundary were coherent, then it would not act as a good source or sink for vacancies, and sliding would not be able to take place. The shear stress to cause such sliding will scale with the grain size, and can become well below the critical resolved shear stress (CRSS) of the bulk material if the new grain size is retained to less than 100 nm. The reason is that the time needed for diffusion will be smaller as the distance between the source and the sink decreases. This phenomenon, where slip can occur at low stresses due to sliding of nano-sized grains rather than bulk deformation, can also lead to lowering of μ.

In this portion of the work, the focus was on the mechanics of slip, and how crystal orientation played a role in determining the depth of slip and the evolution of near surface microstructure. The experimental work was conducted on a Ni single crystal that had been polished to remove the Bilby layer. Different surface normals and sliding directions were utilized in the work. The magnitude of strain can be interpreted from changes in surface texture. This can be understood by reference to Figure 3.2, which shows a simple case of the *slip plane* parallel to the surface and the *slip direction* coinciding with the direction of sliding. The geometry shows that the simple slip can be broken up into a shear strain component and a rotation component. The rotation will be a function of strain, and consequently a function of position below the surface. Thus, if one were to track the orientation of the <001> axis of small regions (pixels) on a (001) pole figure, that has the center along the surface normal, then changes in texture would be observed as a function of wear cycles. In particular, an initial [uvw]=[001] axis for a crystal with [001] surface normal would rotate towards the slip direction, see red arrow in Figure 3.2. The larger the extent of rotation, as measured by the EBSD technique, the larger would be the estimated strain at a given location. The depth of slip penetration can also be interpreted by noting the depth to which the crystal axes deviates from the bulk orientation of the Ni single crystal.

The mechanics analysis focused on the magnitude of resolved shear stress and the multiplicity of slip. The rational was that strongly interacting slip would lead to enhanced hardening, thereby hindering any decrease of μ following an initial hardening stage. The calculations were performed on Ni single crystal, with [001] and [101] surface normals.

3.2. Analytical Procedure

The approach in this investigation was to study the plastic deformation under an indenter by considering resolved shear stresses in different slip planes, and developing contours that reflected regions of constant maximum resolved shear stress (RSS) on the fcc {111}<101> slip systems. If more than one slip system exhibited the same highest resolved shear stress at a given location under the indenter, then the number of multiple systems was noted. These were quantified by the multiplicity of slip; i.e., a multiplicity of 4 would imply that a given location had four slip systems that had the same highest RSS. This multiplicity of slip is important because it determines the hardening characteristic. Thus, a multiplicity of two or more would offer greater hardening than a single slip system. The underlying assumption here is that multiple slip systems can lead to locking mechanisms on intersecting slip planes. Since hardening also depends on the interacting slip systems, in terms of whether interacting dislocations produce a kink or a jog, the analysis also kept track of the specific slip systems. In this way, the extent of slip could be estimated, and compared with the zone of plastic deformation interpreted from EBSD measurements. As mentioned earlier, this interpretation of experimental data is based on the understanding that plastic slip is associated with rotations, which can be measured using EBSD techniques.

In all the calculations, the resolved shear stresses were determined from stress field based on elastic deformation under a cylindrical indenter, see for example Johnson [3.5]. The geometry is illustrated in Figure 3.3. The cylindrical indenter provides a 2-dimensional stress field, making it easier to keep track of the slip directions and slip planes. Obviously this is a simplification, but nevertheless it appears to provide significant physical insight on the deformation process. In Figure 3.3, the value of sliding force, Q, was selected as 0.8P, where P is the normal load. This value of μ=0.8 was selected based on preliminary experiments (see Chapter 4), as will be discussed later. The consideration of an elastic field was one of convenience, and also was guided by previous rigorous elastic-plastic studies [8,9], which indicate that although there are stress redistributions due to plastic deformation, the overall contours of plastic strains are not significantly different from elastic ones. Note that these assumptions were made primarily to aid physics based interpretations. At a more rigorous level, what is needed is crystal plasticity based finite element method (FEM) analysis of the region below a sliding spherical indenter. This analysis is significantly more complex, and was outside the scope of investigation here.

3.3. Results and Discussion

Figure 3.4 illustrates contours of von-Mises effective stress and the shear stress, τ_{xy}, for the loading shown in Figure 3.3. The magnitudes for the contours represent the intensity of the von-Mises stress or the τ_{xy} stress. The figure shows that when Q=0, the maximum von-Mises stress occurs at a depth of around 0.5a, where '2a' is the width of the line of contact. In the case of τ_{xy}, the stresses are antisymmetric, being negative for the left lobe and positive for the right lobe.

Figure 3.5 shows the stress contours when Q=0.8 P. The most notable difference is that the maximum stresses now occur at the surface rather than at a finite depth below the indenter. Indeed, the presence of even a small sliding force Q, always moves the maximum stress location to the surface. Figure 3.5 also shows that the difference between the J2 plot and τ_{xy} plot are now relatively small, at least close to the top surface. The values of the J2 contours are important, since the macroscopic condition for yielding can be compared with microscopic conditions based on the resolved

In order to track the slip planes and slip directions for the fcc lattice, the slip systems were numbered, as shown in Figure 3.6. Both positive and negative slip directions were considered, in order to keep track of which system possessed the highest resolved shear stress. Thus, there is a total of 24 {111}<110> slip systems rather than 12.

Figure 3.7 shows contour maps for the systems with highest resolved shear stress. Thus, a contour with high value implies that the particular region has a high magnitude for the maximum τ_{RSS}. The system to which these belong will be discussed shortly. Figure 3.7 shows that the depth of penetration for contours with values up to 0.30 are relatively insensitive to whether sliding takes place along [100] or [101] on a [010] surface. Closer to the surface, however, the [100] sliding direction leads to slightly higher values of resolved shear stress compared to sliding along [101]. Assuming that the magnitude of slip would scale with the resolved shear stress, based on an elastic stress field, the implication would be greater strain in the near surface region for the [100] sliding direction. Of course, as the contour plots indicate, the highest value of 0.6 is the same for both slip directions.

In order to obtain insight on the hardening behavior once slip is initiated, the multiplicity of slip is plotted in Figure 3.8. By multiplicity we imply the number of slip systems that have the same highest value of τ_{RSS} at a given location. The numbers are superimposed on the contour plots of Figure 3.7, thereby allowing us to determine which locations are critical. Figure 3.8 shows that near the top surface immediately below the indenter (that has contact over the zone -1 to +1), the multiplicity is two for both slip directions. However, further out, the multiplicity becomes 4 for [100] sliding direction, whereas it remains 2 throughout the volume for the [101] sliding direction. In this analysis, it is estimated that the magnitude of hardening would increase with the multiplicity of slip. In addition, even for the same multiplicity of slip, the sliding direction that gives rise to strong dislocation interactions will lead to greater hardening compared to one with weak interactions. The latter could, for example, be two slip directions on the same slip plane.

Figure 3.9 shows the slip systems operating for the [100] slip direction. The maximum stress contours correspond to slip systems 9 and 16. The sketch on the right shows these slip system. Interaction of dislocations on these systems will lead to strong interaction and formation of jogs. Thus, although the contours have higher values below the surface, as seen in Figure 3.7a, the interactions will lead to hardening and increase in the shear stress required for sliding. Referring to Figure 3.1, such interactions will not be conducive to the reduction of the friction coefficient.

Figure 3.10 shows the slip systems for the [101] sliding direction. As shown in the bottom two figures on the right, the most highly stressed systems are 1 and 5. These slip are sketched, and show that both slip systems possess the same slip plane. Consequently, hardening will be minimal for this sliding direction. Further, it may be noted that the second most highly stressed locations have slip systems 9 and 21. These slip systems share a common slip direction, and will allow easy cross slip from one slip system to another. Thus, although there may be some hardening, the magnitude will be considerably much lower than the [100] sliding direction.

Thus, comparison of the plots and sketches in Figures 3.7-3.10 suggest lower hardening and consequently greater accumulation of plastic deformation with the number of wear traces for [101] sliding direction compared to [100] sliding direction. This will lead to grater crystal rotation, as illustrated in Figure 3.2. In addition, a lower hardening in the near surface region will also lead to greater penetration of slip below the surface.

As a final example, we consider the case of sliding in the $[1\bar{1}2]$ direction on a [110] surface normal. Figure 3.11 shows the stress contours, and they are nominally similar to the contours shown earlier. More interestingly, Figure 3.11b shows that there is only one slip system operating in different regions of the crystal. This is a rather unique situation, since it is well known that the extent of Stage I hardening (low hardening) is most extended for single slip conditions. However, it must be noted that the slip systems are different in different regions. This is shown clearly in Figure 3.12. Just beneath the indenter, slip system 13 is operative. To the right, the slip is dominated by shear on slip system 21.

The above slip systems are shown in Figure 3.13, where it may be noted that the slip direction along 21 has a fairly large component along the sliding direction. The edge on view is illustrated at the bottom of the figure. The component 13 corresponds to a vertical shear stress, although the plane is at an angle to the plane of the page. This stress would carry the normal component of the load. On the other hand, the shear component would be carried by slip system 21. Because of operation of a single slip system, hardening would be low, and slip penetration would exist to greater depths of the sample.

3.4. Summary and Conclusions

A model is proposed to describe the depth of penetration of slip and the relative intensity of plasticity below an indenter sliding on an fcc single crystal. This model is based on estimation of resolved shear stresses (RSS) on the {111}<101> system, and on the nature of interaction of dislocations when multiple slip systems have identical highest RSS. Those combination of surface normal and sliding direction that yield multiple slip on strongly interacting slip systems are predicted to show minimum depth of penetration of slip. Conversely, those combinations that favor single slip, or multiple slip with weak interactions between dislocations, are predicted to exhibit greatest plastic penetration as well as largest intensity of plasticity in the near surface region.

The predictions of the model are in excellent qualitative agreement with the experimental evidence, as discussed in Chapter 4. Implicit was our understanding that regions with dislocation slip are always accompanied with crystal rotation, which can be determined using EBSD technique. Thus, we conclude that the depth of penetration of slip from the surface, as well as the intensity of plastic slip in the near surface region are primarily controlled by the multiplicity of slip, and by the type of interactions between dislocations on those systems.

The results on the (101)[1-12] system showed the least resistance to plastic deformation, with only one slip system being operative at any location below the indenter. Based on this, we anticipate (correctly, as detailed hereafter), that this orientation should exhibit the largest depth of deformation below the surface.

μ

Sliding Distance or the Number of
Wear Traces at a Given Location
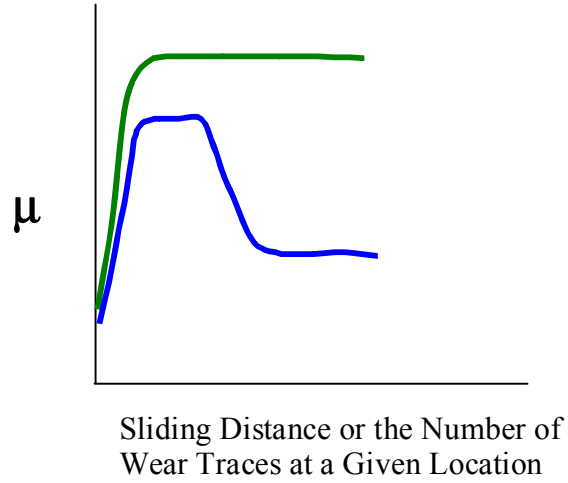
Figure 3.1. Sketch illustrating the evolution of friction coefficient, μ, as a function of the number of wear traces or sliding distance. The decrease of μ is of particular interest.
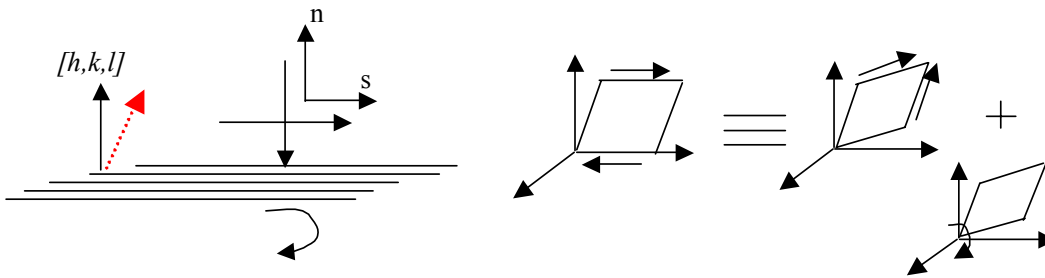
Figure 3.2. Illustration of slip under a sliding indenter. The crystallographic slip leads to both shear strain and crystal rotation, as shown on the right of this figure. The rotation would result in change in orientation. Thus, if [hkl] = [001] on a (001) pole figure was initially concentrated along n, this direction would move away from the surface normal, n, see red arrow.

23
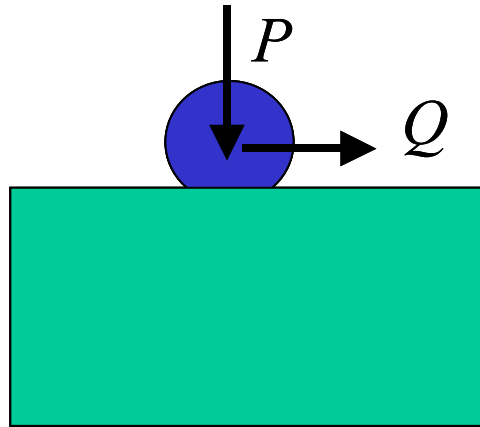
Figure 3.3. 2-dimensional geometry of loading by a cylindrical indenter. The horizontal component of the force, Q, was taken as 0.8 in the calculation, based on initial results for a Si3N4 ball sliding on a Ni single crystal.

Loading, Q=0
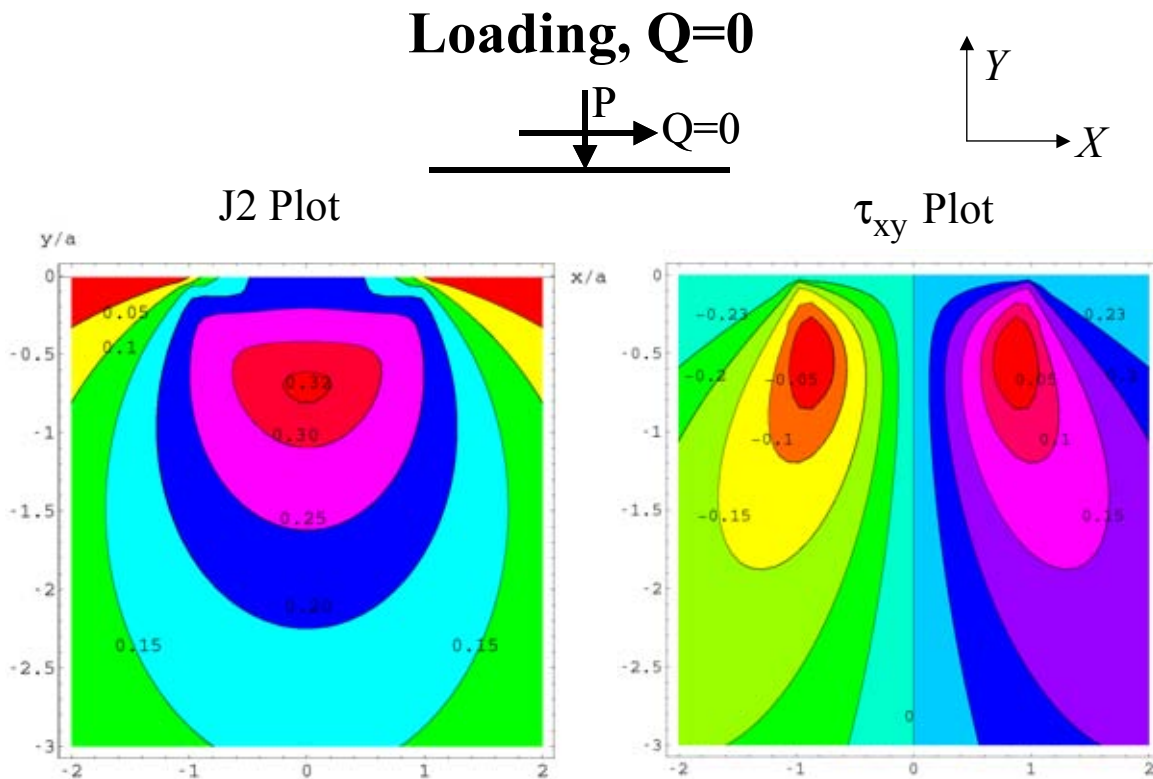
Figure 3.4. Contour plots of J2 (or von Mises stress) and txy, for the case of Q = 0. The stresses have been normalized with respect to the load P. Only the relative values of the contours are important here. Note that the maximum von-Mises stress occurs at a finite depth below the indenter, approximately a/2. Here, '2a' is the width of contact, and the lengths are normalized with respect to 'a'. In the figures, the line of contact is at the top, between -1 and +1.

Sliding Contact, Q=0.8P

J2 τ_{xy}
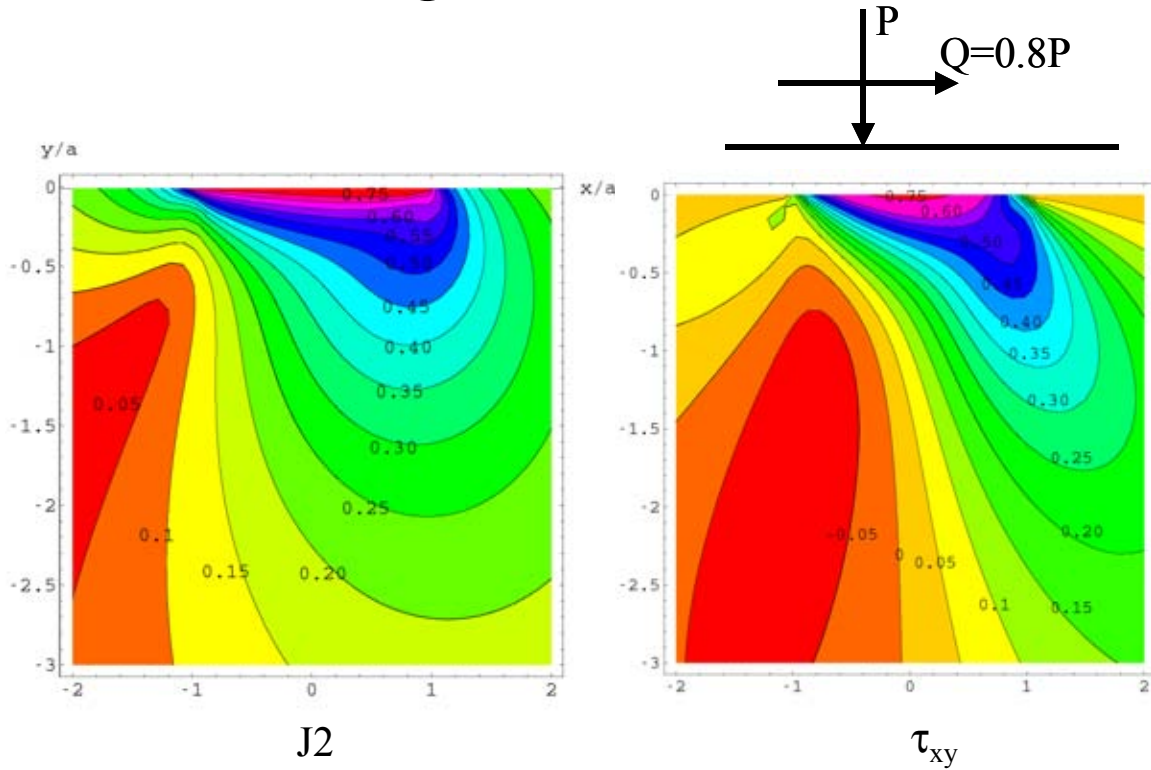
Figure 3.5. Contour plots of J2 (or von Mises stress) and τ_{xy}, for the case of Q = 0.8P. The stresses have been normalized with respect to the load P. Note that the maximum shear stress locations have moved to the surface.

1	(-1, 1, 0)	(1, 1, 1)
2	(1, -1, 0)	(1, 1, 1)
3	(-1, 0, 1)	(1, 1, 1)
4	(1, 0, -1)	(1, 1, 1)
5	(0, 1, -1)	(1, 1, 1)
6	(0, -1, 1)	(1, 1, 1)
7	(1, 1, 0)	(-1, 1, 1)
8	(-1, -1, 0)	(-1, 1, 1)
9	(1, 0, 1)	(-1, 1, 1)
10	(-1, 0, -1)	(-1, 1, 1)
11	(0, 1, -1)	(-1, 1, 1)
12	(0, -1, 1)	(-1, 1, 1)
13	(-1, -1, 0)	(-1, 1, -1)
14	(1, 1, 0)	(-1, 1, -1)
15	(-1, 0, 1)	(-1, 1, -1)
16	(1, 0, -1)	(-1, 1, -1)
17	(0, -1, -1)	(-1, 1, -1)
18	(0, 1, 1)	(-1, 1, -1)
19	(-1, 1, 0)	(1, 1, -1)
20	(1, -1, 0)	(1, 1, -1)
21	(1, 0, 1)	(1, 1, -1)
22	(-1, 0, -1)	(1, 1, -1)
23	(0, -1, -1)	(1, 1, -1)
24	(0, 1, 1)	(1, 1, -1)
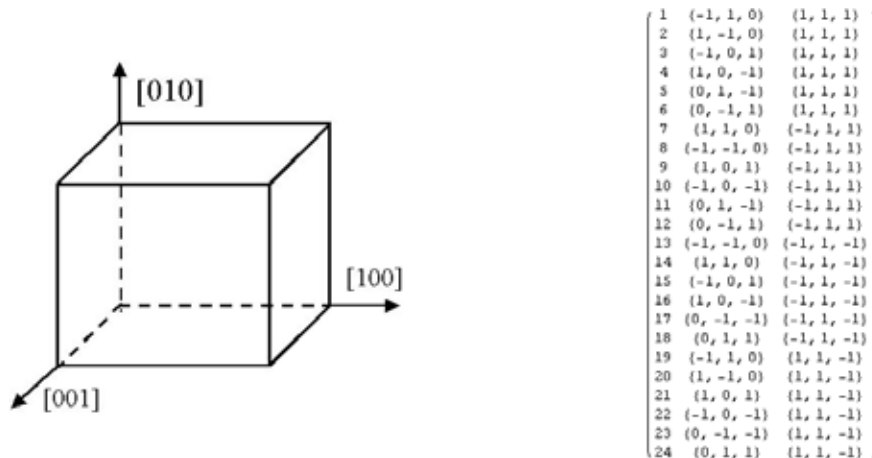
Figure 3.6. An illustration of the crystal axes, and the nomenclature for the slip systems. Thus, slip system 5 corresponds to the (111)[01-1] system. Both positive and negative slip directions are included to keep track of slip direction with respect to loading direction, thereby resulting in 24 systems rather than 12.

[100] Sliding Direction   *[101] Sliding Direction*
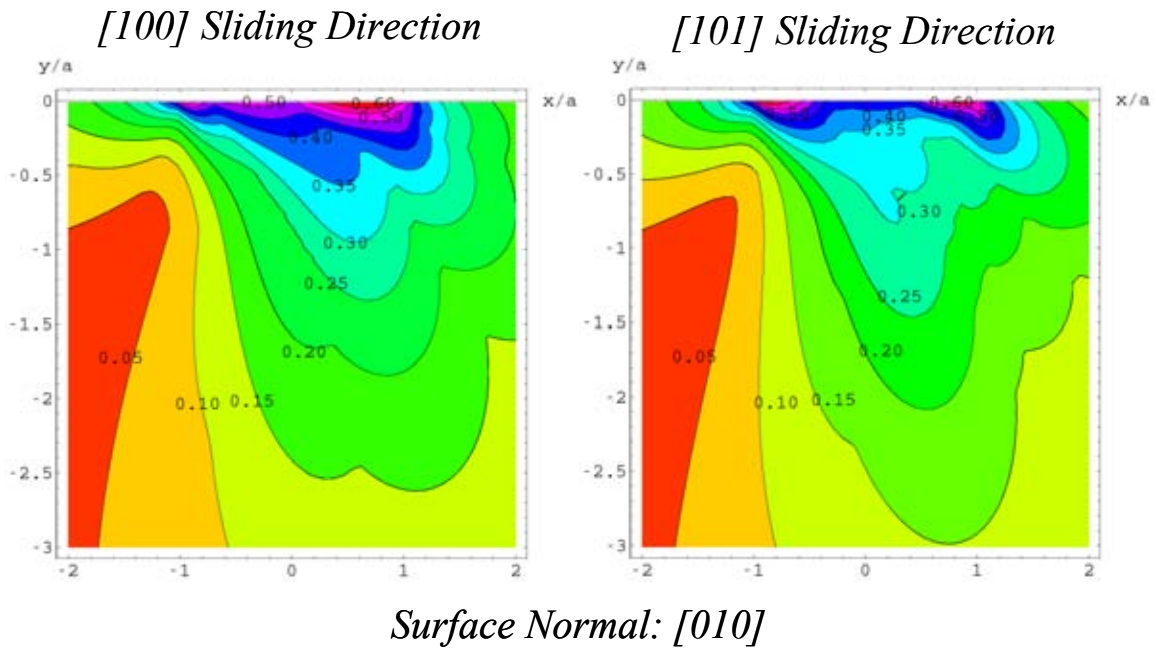
Surface Normal: [010]

Figure 3.7. Contours of slip for [100] and [101] sliding directions, for the crystal with surface normal [010]. The magnitude of resolved shear stress is represented by the values of the contours, with a high value implying greater magnitude of τ_{RSS}. Note that there is relatively small difference in the depth of the contours for the two sliding directions.
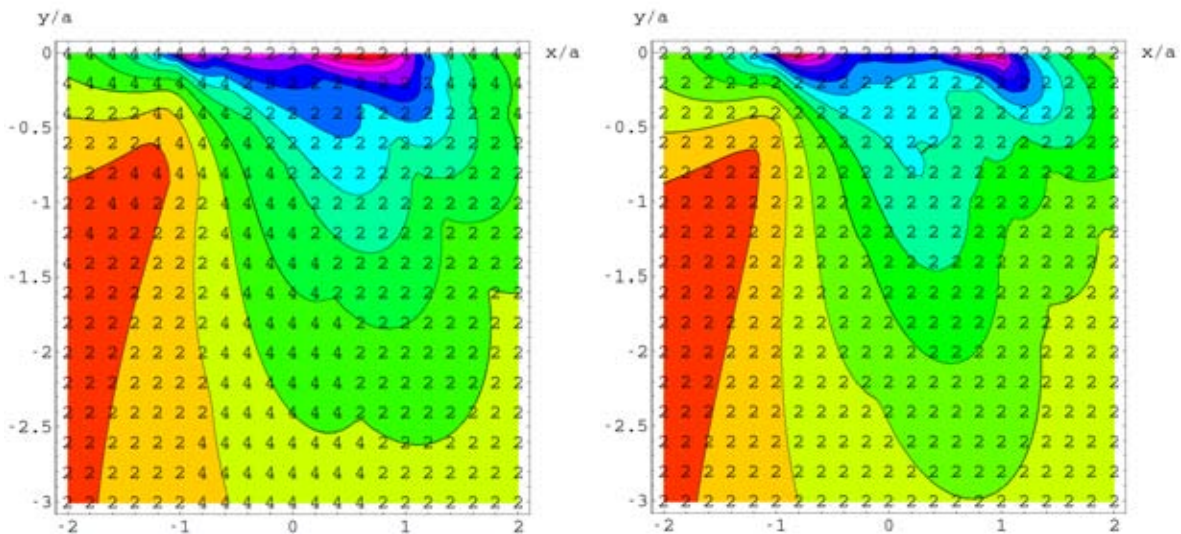
Figure 3.8. Schematic showing the multiplicity of slip below the sliding indenter for the crystal with [010] surface normal. The left figure corresponds to sliding along [100] while the right figures correspond to sliding along [101].

Operating systems near surface:

(a)   ABC plane and AB direction, (-1 1 1)[101]

(b)   DEF plane and DE direction, (-1 1 -1)[10-1]

Strong dislocation interaction.
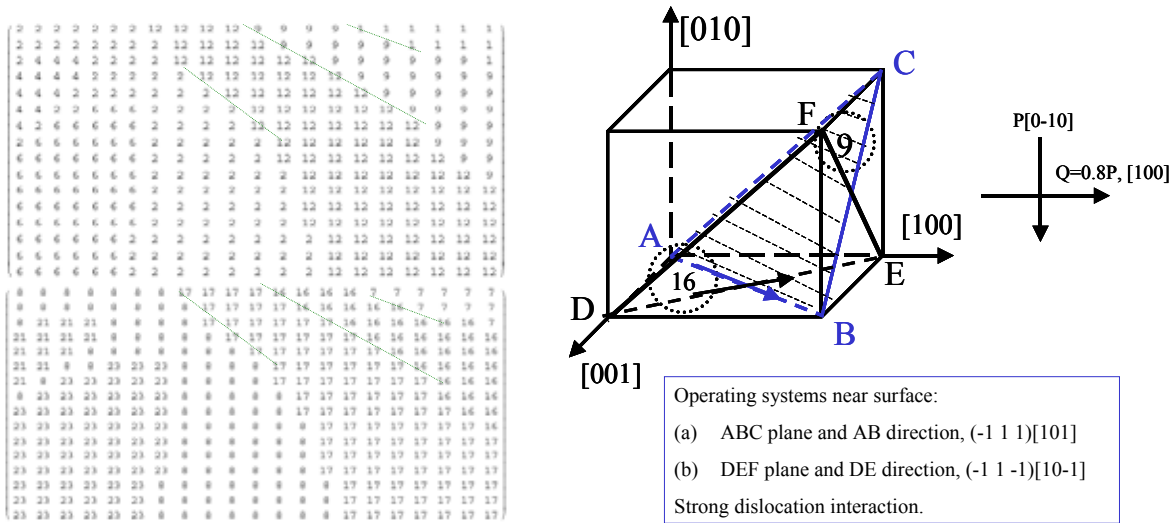
Figure 3.9. Slip systems operating for the [100] slip direction for [010] surface normal. The slip systems 9 and 16 have the highest values of maximum resolved shear stress. The sketch on the right shows the systems, indicating strong dislocation interaction through jog formation.
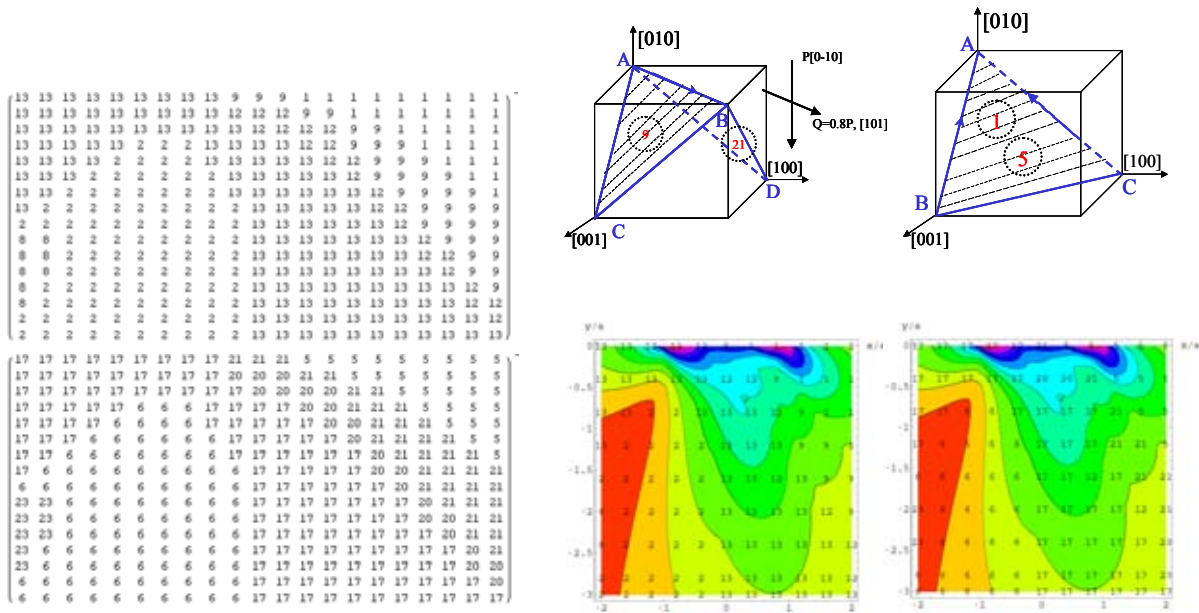
Figure 3.10. Slip systems operating for the [101] slip direction with [010] surface normal. The slip systems 1 and 5 have the highest values of maximum resolved shear stress. The sketch on the right shows these systems have the same slip plane, and consequently minimum hardening. Just below the indenter and slightly to the right, the operating systems are 9 and 16. These systems possess the same slip direction, thereby allowing easy cross slip and relatively lower hardening.
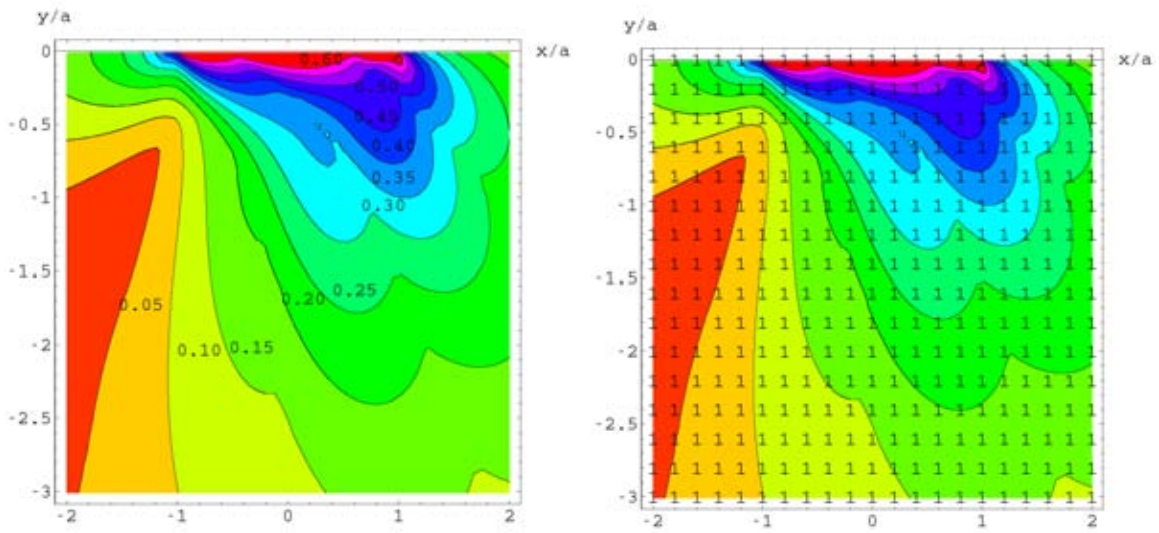
Figure 3.11. Contour plots of the maximum resolved shear stress for the case of [110] surface normal and [1-12] sliding direction. The contours are nominally similar to the previous orientations. However, note that single slip exists throughout the crystal, although the systems are different in different in different locations.
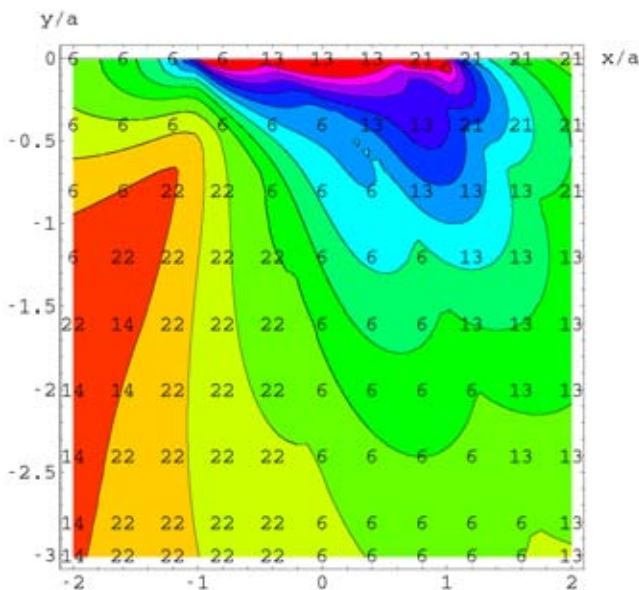
Sliding Direction [1$\overline{1}$2]

Surface Normal [110]
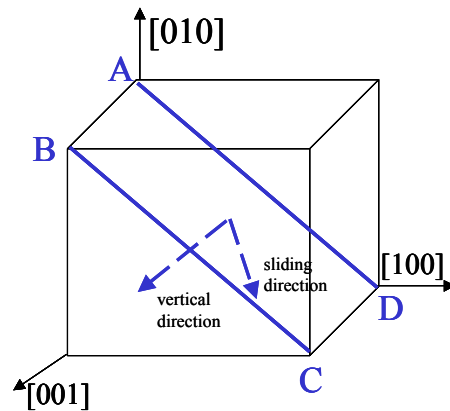
Figure 3.12. Operating slip systems for (110)[1-12] sliding. The most highly stressed regions have slip systems 13 and 21.
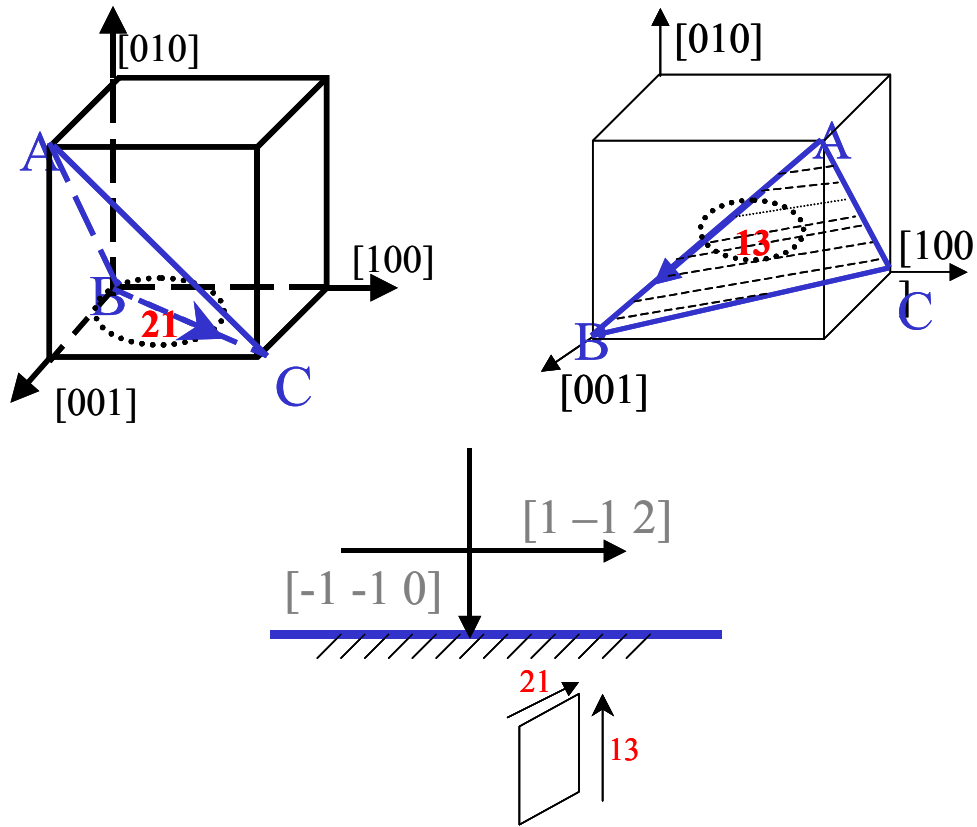
Figure 3.13. The slip orientations for the highly stressed regions for (110)[1-12] sliding system. The bottom figure shows the slip systems viewed edge on. Slip system 13 is below the indenter, while slip system 21 is slightly to the right. It is this system 21 that will control the shear stress at the surface.

4. Friction Measurements and EBSD Analysis

4.1. Introduction

Microstructural evolution underneath wear surfaces has been the subject of numerous prior studies. In all the above studies, large wear scars were generated under heavy loads to facilitate cross-sectional TEM specimen preparation by conventional methods. These specimen preparation techniques, as discussed in Chapter 2, are not capable of making cross-section at specific locations on a wear scar. By utilizing the rotary stage designed and built as a part of this LDRD project (Chapter 2), we have successfully made friction measurements and generated wear scars on single crystal Ni surfaces in several crystallographic directions. The FIB sections of wear scars were analyzed by EBSD, and in a few cases by transmission electron microscopy. The results of this study are given in this chapter.

4.2. Friction Measurements

Measurements were made with Si_3N_4 balls so that the deformation during sliding contact is essentially confined to the softer Ni surface. For the ease in interpreting the EBSD data and for gaining insights into sliding induced recrystallization phenomena, friction tests were conducted in unidirectional sliding mode. For any given normal load, the extent of subsurface deformation
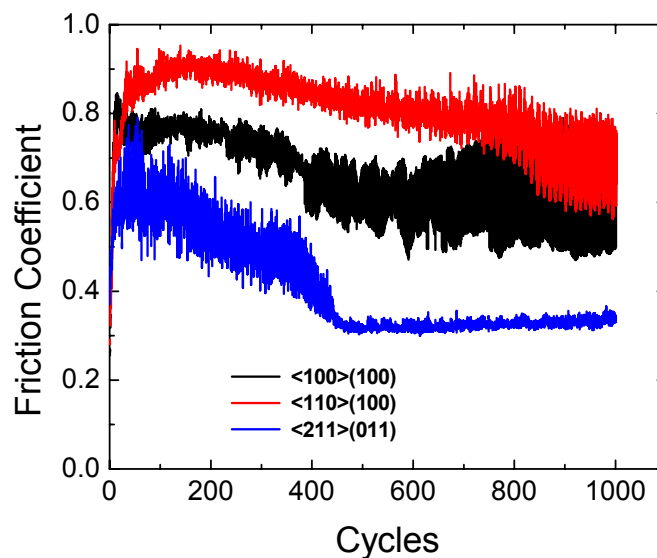
Figure 4.1. Friction coefficients of Ni single crystal surfaces in several crystallographic directions. Note the transition at 400 cycles in the (011)<211> orientation.

was found to be dependent on the crystallographic direction, as evidenced by EBSD analyses from FIB cross sections of wear scars. Another interesting finding is the friction transitions in certain specific crystallographic directions. For example, the friction coefficient on the (011) surface along <211> direction showed a sudden drop from 0.7 to 0.3 after 400 cycles of sliding at a normal load of 100 mN (Fig. 4.1).

Analysis of the resolved shear stresses on the FCC slip systems in this (011)<211> orientation reveals a single slip condition which leads to relatively little dislocation interaction and work hardening, and therefore in large deformations and rapid recrystallization as wear progresses. The friction measurements given in Figure 4.1 were made at a normal load of 100 mN on a 3.125 mm diameter Si_3N_4 Ball

We have also investigated the effect of increased normal load on recrystallized grain structures, and how these new structures in turn would influence friction. The friction trace in Figure 4.2 was generated on the (110)<110> orientation at a much higher normal of 1N for 2000 cycles of sliding. Note that the friction coefficient is high, 0.9 to 0.8. However, as revealed by EBSD and TEM analyses (Fig 4.3), by employing higher contact stresses, we were able to generate unusual structures underneath the wear scars. In the next step, we continued the friction test on the same wear scar for another 1000 cycles of sliding at a much reduced normal load of 50 mN. The reason for decreasing the normal load is to ensure that the deformation in the second stage of the measurement was confined to the recrystallized zone created during the first stage. As can be seen from Fig. 4.2, there is not only a significant decrease in the friction coefficient (0.8 to 0.15) but also in the amplitude of the fluctuations in friction force.
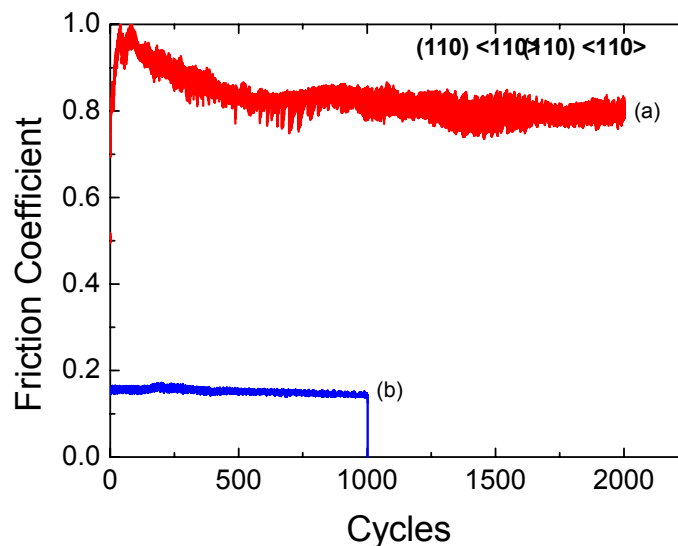
Figure 4.2. (a) Friction coefficient in the (110)<110> orientation at 1N normal load. (b) Friction coefficient at 50 mN load when the test was performed on track (a).

4.2. EBSD Analysis

Electron backscattered diffraction (EBSD) has been used in this study to understand the deformation, orientation changes and recrystallization that is associated with sliding wear of Ni single crystals. Orientation mapping using EBSD is accomplished in the following manner. The electron beam is scanned pixel-by-pixel over an area of interest and an EBSD pattern is collected at each pixel. The EBSD pattern is then automatically indexed to give the three dimensional orientation of the crystal at that point. This process is repeated at each pixel of the scan and an orientation image is produced. Modern EBSD orientation mapping systems can analyze nearly 100 patterns per second. The display of these maps is done by assigning colors to a stereographic triangle and then mapping these colors on the measured orientations.   In addition, the data can also be displayed as orientation differences from one pixel to the next. These maps are very useful when small orientation changes are to be characterized.
As discussed in Chapter 2 this analysis must be conducted on cross sections of the wear scars and not on the wear surface.

EBSD was carried out on many samples for this study.   In this section we will refer to the samples as {hkl} <uvw>. This nomenclature describes the plane of the crystal surface {hkl} and the direction of sliding <uvw>. We have studied Ni single crystals with (100), (110) and (111) orientations. We have tested sliding directions in <100>, <110>, <111> and where possible <112>. Of course not all these directions can be tested on every single crystal orientation as discussed in Chapter 2.
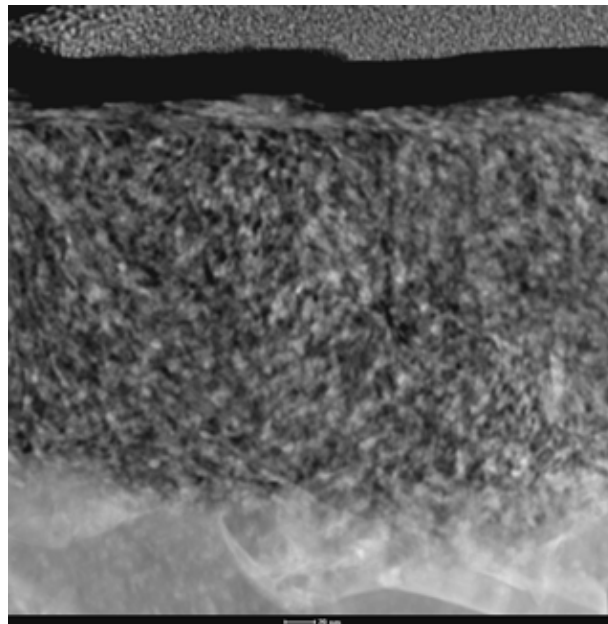
Figure 4.3. STEM annular dark field image of the nanocrystalline structure in the of the wear scar from Fig. 4.2b.

As discussed in Chapter 2, ion imaging can provide information about deformation and grain size. Figure 4.4 shows ion channeling images of cross sections of wear scars prepared on {111} Ni surfaces in the <110> direction. Figure 4.4a shows the ion channeling image for a 10 g normal load and figure 4.4b shows the result for a 100 g normal load. In these images the wear direction is right to left. The top most layer visible in the images is a Pt protective cap that is applied during FIB sample preparation. Below the featureless Pt layer the changes in gray level indicate changes in orientation in a qualitative manner. The interesting observations are that at the lower load of 10 g shown in Figure 4.4a, the depth of deformation is much shallower than that which occurs under the higher 100 g normal load shown in Figure 4.1b. There also appears to be regions of fine grains at the surface of each sample that is thicker on the higher normal load test shown in Figure 4.4b. Although these images are quick and reasonably easy to obtain, they do not provide any quantitative information about the sub-surface deformation induced by wear. One cannot use the changes in gray level in these images to infer anything about the relative orientation changes that have occurred.

EBSD orientation mapping can provide quantitative information about the orientation changes that occur as a result of wear induced sub-surface deformation. Figure 4.5 shows EBSD orientation maps from the same areas from which the ion channel images of Figure 4.5 were obtained. The general microstructural features that are visible in the ion channeling images of Figure 4.4 are visible in the band contrast images in Figure 4.5a and d. The fine grained regions near the surface of the sample are clearly visible . Quantitative orientation changes can be observed in the orientation maps shown in Figure 4.5 b and c. Here the orientations are displayed with respect to the sliding direction and color coded by the stereographic triangle shown. The sliding direction is <110> and this can be determined from the orientation maps by the green color of the image below the deformed region indicating a <110> sliding direction. A comparison of Figures 4.5 b and c shows that the depth of orientation changes is much deeper for the higher normal load as expected. Figures 4.5 c and f are orientation difference maps. Here a pixel that is expected to be representative of the starting single crystal orientation is selected and then orientation differences to each pixel in the image are calculated and displayed in the color scale of blue to red with blue representing small orientation changes and red representing large orientation changes. A comparison of Figure 4.5c and e demonstrates quantitatively the difference in the depth of deformation caused by the 10 fold increase in normal load.

Figure 4.6 shows band contrast, inverse pole figures and orientation difference images for the sample worn on {100} in the <110> direction. Here we show the inverse pole figure maps with respect to the surface normal (figure 4.6b), the sliding direction (figure 4.6c) and the normal to the sliding direction (figure 4.6d). Three inverse pole figures are needed to show the orientation changes that occur during sliding wear. Figures 4.6 and 4.8 show similar EBSD orientation mapping results for {100}<100> and {110}<211>.

There are a number of interesting observations that can be made from a comparison of Figures 4.6, 4.7 and 4.8 concerning the orientation changes associated with wear in single crystals, the amount of recrystallization, or new grain formation, and the depth of deformation. Each of these observations potentially may have an impact on the measured coefficient of friction observed on the single crystals of Ni.

Orientation difference maps are useful in the visualization of plastic deformation. This is especially so n the case of wear of single crystal in that we know the starting orientation of the single crystal. It is thus a simple manner to measure the change in orientation from the starting orientation and plotting that information as a map. Figure 4.9 shows the orientation difference maps together for the wear tracks {100}<100>, {110}<100> and {110}<211>. These maps were for wear scars formed with a 10 g normal force for 1000 cycles. It is quite apparent that the amount of deformation below the wear scar increases in the order {100}<100>, {110}<100> to {110}<211>. The coefficient of friction is often associated with the amount of deformation in the substrate one would expect the friction coefficient to increase with increasing amounts of subsurface deformation. Thus, for the first time, EBSD has provided a real connection between the crystallography of the substrate and the sub-surface deformation associated with wear.

The orientation maps of Figure 4.6, 4.7 and 4.8 demonstrate a couple of points in how the plastic deformation associated with sliding proceeds. For any one of these figures, we can use the orientation maps with respect to the sliding direction and the normal to the sliding direction to understand the nature of the orientation changes associated with the plastic deformation that accompanies sliding wear. Note that in the orientation maps with respect to the sliding normal (Figure 4.6d, 4.7d, 4.8d), the orientation of the sample does not change until just below the surface of the sample while the orientation maps with respect to the sliding direction (Figure 4.6b, 4.7b and 4.8b) show orientation changes that extend much deeper into the sample. This behavior can be explained in the following manner. Sliding results in the plastic straining of the area under the wear scar. Material movement is in the direction that the counterface moves. However, in a direction normal to the sliding direction the plastic strain causes orientation rotations that maintain the original orientation. This can be visualized as the orientation rotating around a direction normal to the sliding direction. From these measurements we now have a more complete view of how material below the wear scar moves in response to the applied shear strains.

Comparison of Figures 4.6b, 4.7b and 4.8b shows that the crystallography of the sample effects the development of a fine recrystallized layer at the surface of the sample. Note that the recrystallized layer appears as a fine layer of random orientation adjacent to the surface of the sample. This layer is very thin for wear scars formed on {100}<100> and {110}<100> but is much thicker for the sample {110}<211>. This result may indicate that more deformation occurs in the later sample leading to larger amounts of recrystallization.
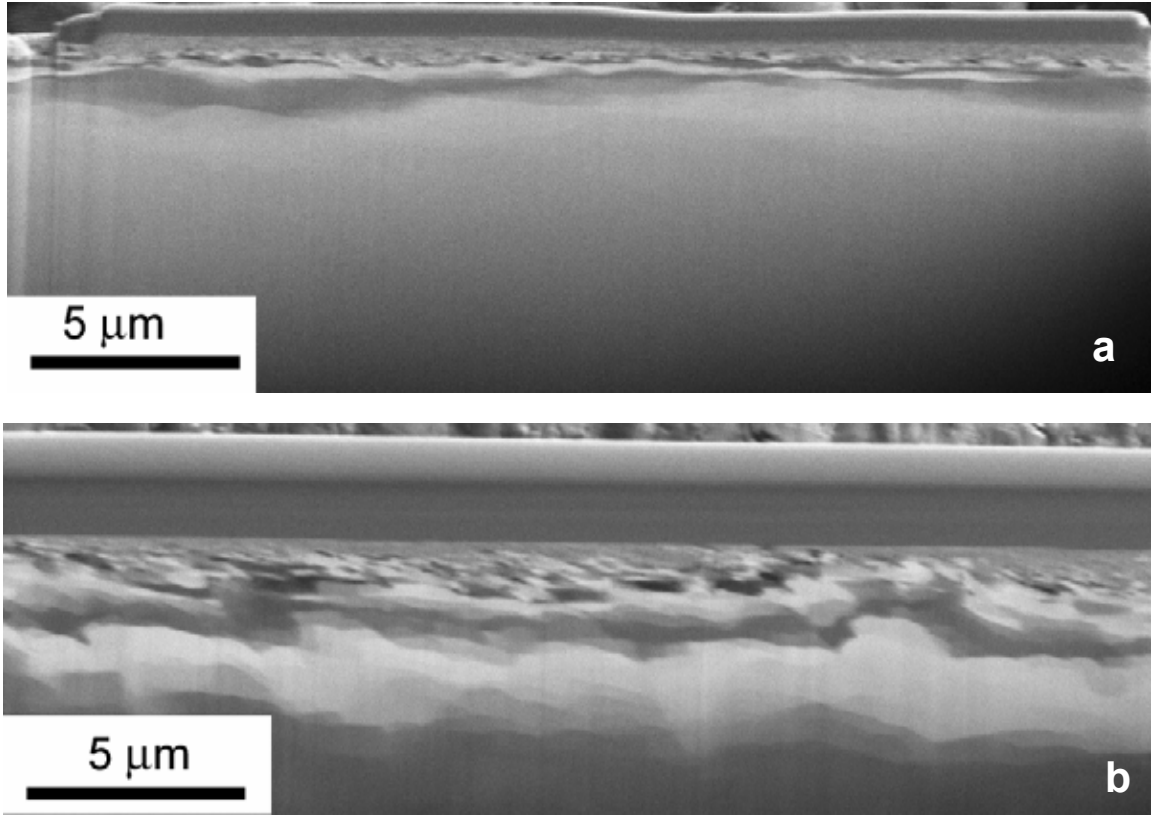
Figure 4.4. Ion channeling images of cross sections of wear scars performed on a {111} surface in the <110> direction. a) 10 g normal load for 1000 cycles b) 100 g normal load for 1000 cycles.
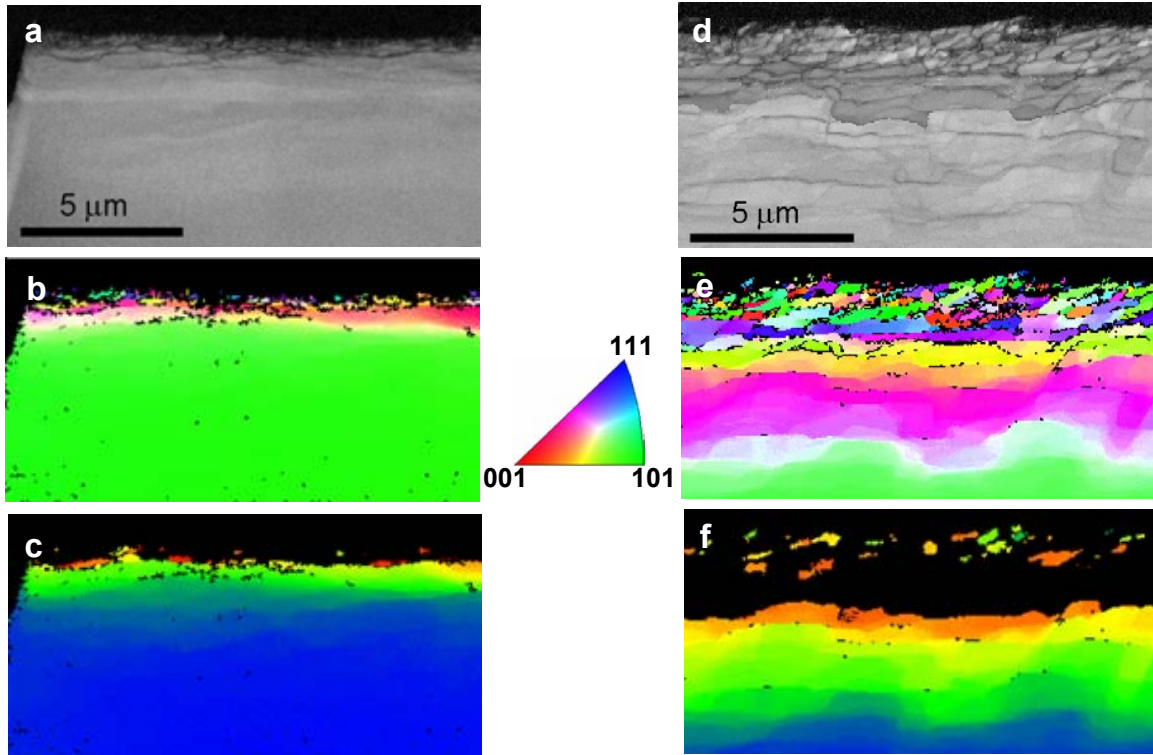
Figure 4.5. EBSD orientation maps and color legend obtained from the wear scar cross sections shown in Figure 4.1 on {111} surfaces in the <110> direction. Images a-c are for the 10 g load for 1000 cycles and images d-f are for the 100g load for 1000 cycles. a and d. Band contrast images, b and e. orientation maps with respect to the sliding direction (horizontal), c and f. Orientation difference maps (blue to red represents 20º orientation changes.
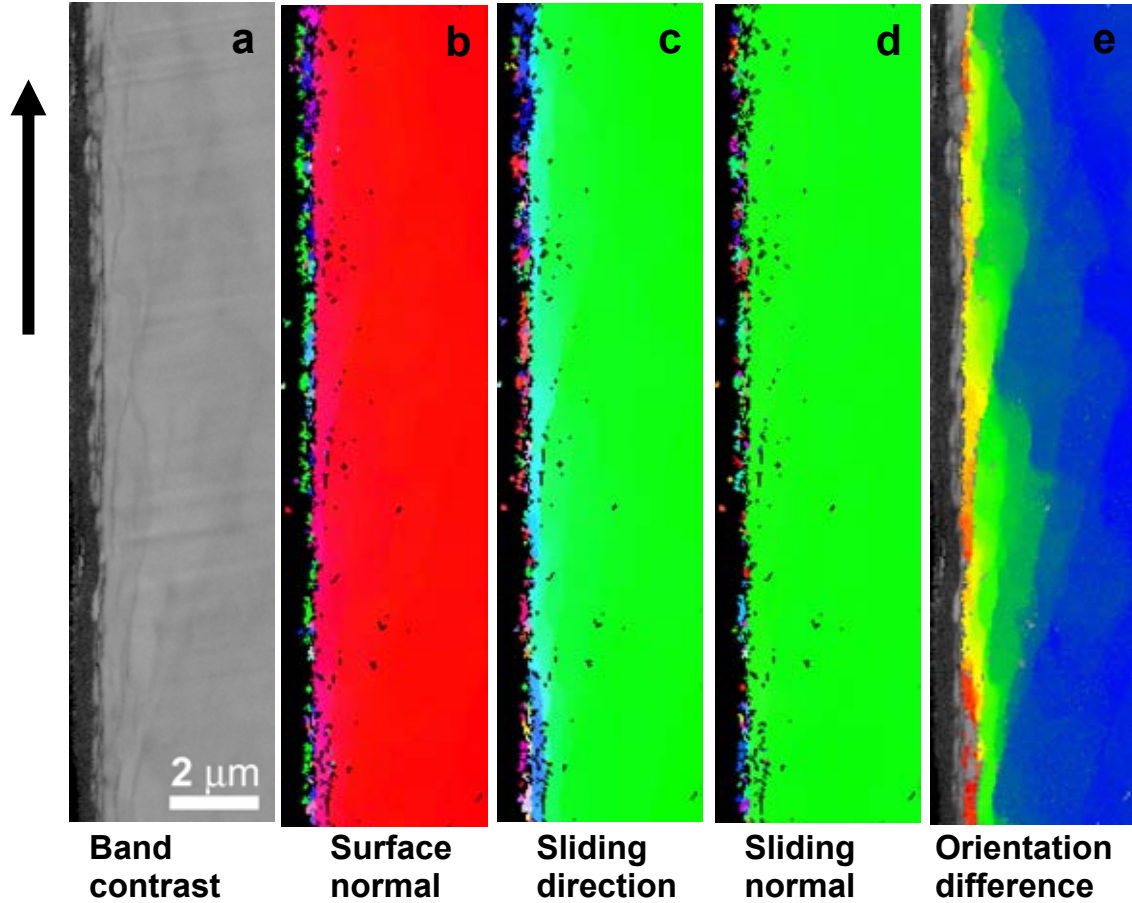
Figure 4.6. EBSD orientation mapping results for a wear scar (10g, 1000 cycles) on {100} in the <110> direction (arrow indicates sliding direction). a) band contrast image. b) Inverse pole figure map with respect to the wear surface normal, c) Inverse pole figure map with respect to the wear sliding direction, d) Inverse pole figure map with respect to the normal to the sliding direction, e) Orientation difference map with respect to the undeformed substrate. Orientation difference maps (blue to red represents 20º orientation changes.

| Band contrast | Surface normal | Sliding direction | Sliding normal | Orientation difference |
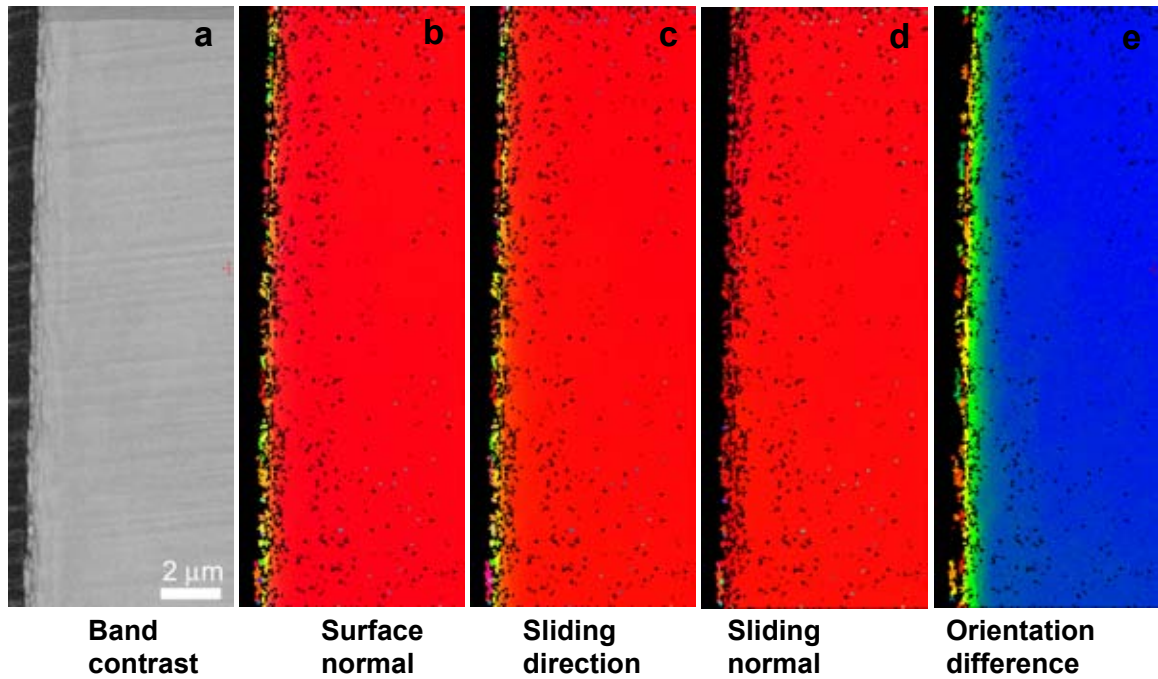
Figure 4.7. EBSD orientation mapping results for a wear scar (10g, 1000 cycles) on {100} in the <100> direction (sliding direction is the same as Figure 4.3). a) band contrast image. b) Inverse pole figure map with respect to the wear surface normal, c) Inverse pole figure map with respect to the wear sliding direction, d) Inverse pole figure map with respect to the normal to the sliding direction, e) Orientation difference map with respect to the undeformed substrate.

| Band contrast | Surface normal | Sliding direction | Sliding normal | Orientation difference |
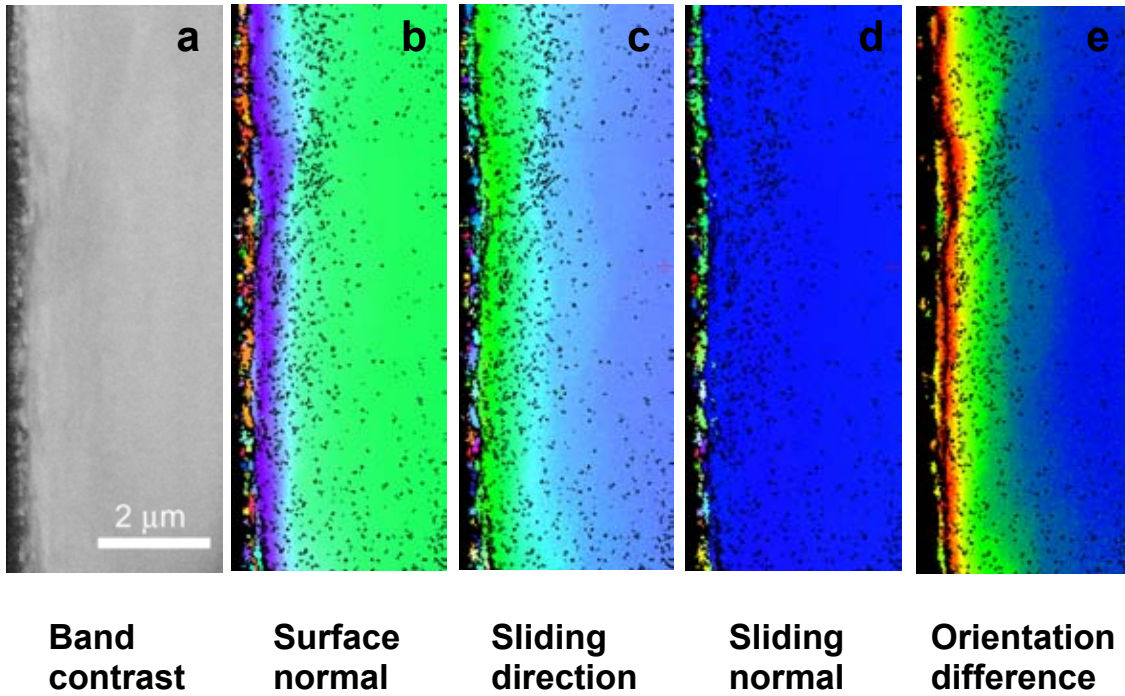
Figure 4.8. EBSD orientation mapping results for a wear scar (10g, 1000 cycles) on {110} in the <211> direction (sliding direction is the same as Figure 4.3). a) band contrast image. b) Inverse pole figure map with respect to the wear surface normal, c) Inverse pole figure map with respect to the wear sliding direction, d) Inverse pole figure map with respect to the normal to the sliding direction, e) Orientation difference map with respect to the undeformed substrate.
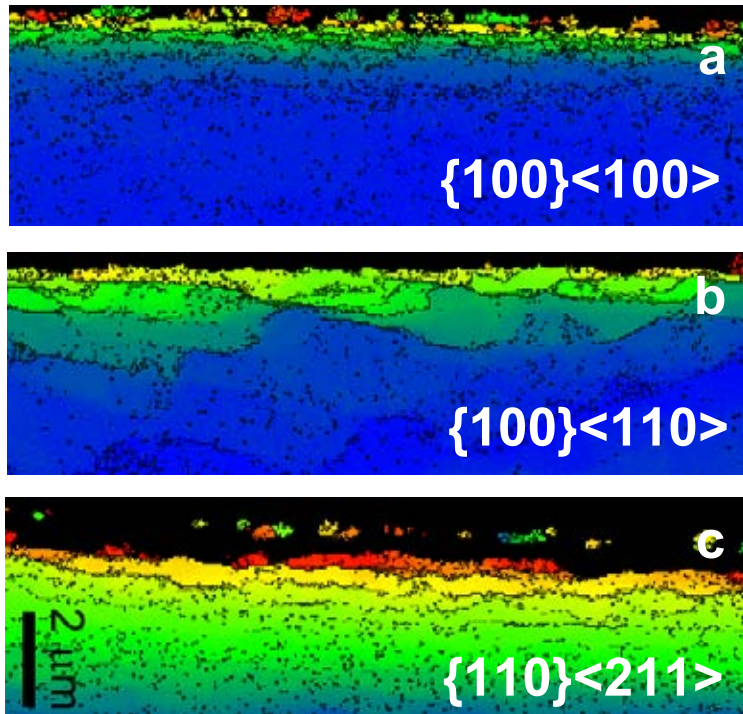
Figure 4.9. Comparison of orientation difference maps from samples worn at 10g normal load for 1000 cycles. a) {100}<100>, b) {100}<110> and c) {011}<211>.

5. Modeling the Evolution of Deformation, Microstructure, and Friction

5.1. Modeling Plastic Deformation During Wear

The response of a material to friction is a complex process, but perhaps the most important phenomenon involved in the wear response of a metal is its deformation via dislocation plasticity. The experimental evidence from the present study strongly suggests that dislocation activity leads to the formation of subgrains in the (initially) single crystal material.

In order to describe the plastic deformation of the worn metal, and on a scale relevant to the experiments, we use a continuum constitutive model of crystal plasticity [5.1]. This model is adapted from a Sandia-developed constitutive formulation developed at Sandia for finite element analysis (FEA). In order to enable the treatment of kilocycle wear, we have condensed the original constitutive formulation into an approximate and more efficient form, as described below.

Unlike in an FEA approach, where nodal displacements are computed to equilibrate the internal stresses, we assume that the stress state is static and that the material does not deform. Because the experimental friction tests are load-controlled, this approximation is not drastic, and the gains in computational efficiency are immense. In our model, the static state of stress is taken from analytical solutions for the contact stresses underneath a cylindrical frictional indenter [5.2], such that

$$\sigma_{xx} = p_{\mathrm{o}}C_4 - 2p_o\mu x\left(1 - \frac{C_1}{C_2}\right) + \mu p_o C_5,$$

$$\sigma_{yy} = -p_{\mathrm{o}}y^3\frac{C_1}{C_3} - p_o\mu C_5,$$

$$\sigma_{zz} = -2\nu_s p_{\mathrm{o}}y\left(\frac{C_2}{C_1} - 1\right),$$

$$\sigma_{xy} = -p_{\mathrm{o}}C_5 + p_o\mu C_4,$$

$$\sigma_{xz} = \sigma_{yz} = 0,$$

$$p_{\mathrm{o}} = \frac{2P}{\pi}\left(\sqrt{\frac{4RP}{\pi}\left(\frac{1-\nu_i^2}{E_i} + \frac{1-\nu_s^2}{E_s}\right)}\right)^{-1}, \tag{5.1}$$

$$C_1 = \sqrt{\frac{x^2 + y^2 - 1 + \sqrt{\left(1 - x^2 - y^2\right)^2 + 4y^2}}{2}},$$

$$C_2 = \sqrt{1 + C_1^2},$$

$$C_3 = C_1{}^4 + y^2,$$

$$C_4 = y\left(2 - \frac{C_1}{C_2} - \frac{C_2}{C_1} - \frac{C_1{}^3 x^2}{C_2{}^3\left(C_1{}^4 + y^2\right)}\right), \text{ and}$$

$$C_5 = xy^2 \frac{C_1}{C_2 C_3},$$

where σ_{xx} is the xx component of the stress; p_o is the maximum contact pressure; μ is the friction coefficient; ν is Poisson's ratio; P is the applied load; R is the radius of the cylindrical indenter; E is Young's modulus; $C_{1\text{-}5}$ are constant functions of the spatial coordinates, introduced for convenience; the subscripts i and s denote indenter and substrate, respectively; the spatial coordinates are in units of the contact length of $2P/\pi p_o$; and the coordinate $(x,y) = (0,0)$ corresponds to the perpendicular intersection between the radius of the cylindrical indenter and the substrate surface. A graphical example of the stress field in Equ 1 is shown in Fig 1.

The model tracks a vertical line (extending into the positive y-direction – see Fig 5.1), called hereafter the Region of Interest (ROI), as it passes through the stress field of Eq 5.1. The bounds of the ROIs travel, and the length of the line representing the ROI, are determined from the edges of the rectangle within which the stresses in Eq 5.1 are sufficient to initiate dislocation plasticity (see below). During each wear cycle, the ROI moves in small increments in the $-x$ direction, and at each increment the stresses in Equ 5.1 are applied to the crystal plastic constitutive model (see below) to evolve the hardness and dislocation content of the ROI.

At each increment within a wear cycle, the stresses in Equ 5.1 are decomposed onto the FCC slip systems according to the predefined crystallographic orientation of the substrate material:

$$\tau_\alpha = \mathbf{\sigma} : \mathbf{P}_\alpha, \tag{5.2}$$

where τ_α is the resolved shear stress on slip system α, and bold variables denote tensors. $\mathbf{P}_\alpha$ is the skew-symmetric component of the dyad of the lattice vectors for slip system α:

$$\mathbf{P}_\alpha = \frac{\vec{d}_\alpha \otimes \vec{n}_\alpha + \vec{n}_\alpha \otimes \vec{d}_\alpha}{2}, \tag{5.3}$$

where $\vec{d}_\alpha$ and $\vec{n}_\alpha$ are the slip direction and slip plane normal, respectively, for slip system α; and $\otimes$ is the tensor product [5.3]. The slip directions and slip plane normals are defined relative to the global coordinate system, and thereby depend on the crystallographic orientation of the substrate material. The resolved shear stress is used to compute the slip rate,

$$\dot{\gamma}_\alpha = \left(\frac{\tau_\alpha}{\Gamma_\alpha}\right)^{30}, \tag{5.4}$$

where $\dot{\gamma}_\alpha$ is the slip rate on slip system α and Γ_α is the critical resolved shear stress on slip system α. Slip rates below 1×10^{-5} per sec were neglected. The plastic deformation rate on slip system α is computed from the slip rate via

$$\dot{\mathbf{D}}_\alpha = \frac{\dot{\gamma}_\alpha}{2}\mathbf{P}_\alpha,$$ (5.5)

which then determines the plastic strain increment via

$$\Delta\varepsilon_\alpha = \Delta t \sqrt{\frac{2}{3}\left(\dot{\mathbf{D}}_\alpha : \dot{\mathbf{D}}_\alpha\right)},$$ (5.6)

where $\Delta\varepsilon_\alpha$ is the plastic strain increment in slip system α and Δt is the time increment determined from the distance that the ROI moves and the sliding speed (3.75 mm/sec in this work). Finally, the critical resolved shear stress is updated via

$$\Gamma_\alpha = 67 + 495\left[1 - \exp\left(-\frac{3139}{495}\varepsilon_\alpha\right)\right],$$ (5.7)

where Γ_α is in units of MPa, the constants were fit to experimental tension test data; and ε_α is the accumulated plastic strain in slip system α over all prior deformation. The deformation increments, i.e. Δt, were chosen such that the maximum sliprate along the ROI line never exceeded 10 per sec.

In order to model the formation of microstructure as the worn material deforms, we assume that the dislocations generated during wear will organize into subgrains. (This is supported by the TEM evidence. Further, we assume that the average size of these subgrains is related to the total equivalent plastic strain [5.4] according to

$$d = \frac{0.724}{\varepsilon_p^{\,2}}$$ (5.8)

where d is the average subgrain size in μm, and the constants were derived from rolling experiments on Al [5.4]. The total equivalent plastic strain, ε_p, is the accumulation of plastic strain increments defined as

$$\Delta\varepsilon_p = \Delta t \sqrt{\frac{2}{3}\left[\left(\sum_{\alpha=1}^{12}\dot{\mathbf{D}}_\alpha\right) : \left(\sum_{\alpha=1}^{12}\dot{\mathbf{D}}_\alpha\right)\right]}.$$ (5.9)

5.2. Deformation Under Ideal Contact

If we assume a perfectly smooth Si_3N_4 ball and Ni surface, and that no material transfer or debris is generated during the wear process, then the radius of the indenter, R in Equ 5.1, is $R = 1/16"$ in the present context. (This is a bad assumption, as we will soon see.) Using a normal load of $P = 1$ N, a friction coefficient of $\mu = 0.8$, and the material properties in Table 5.1 for Si_3N_4 and Ni, the equivalent plastic strain (at a location 400 nm below the Ni surface) evolves over 2000 cycles as shown in Fig 5.2a. Using Equ 5.8 to estimate the subgrain size produced by the plastic strain in Fig 5.2a yields Fig 5.2b. A cursory qualitative comparison between Fig 2b and the micrographs in Chapter 3 reveals that the ideal contact assumption is drastically insufficient to produce the levels of deformation, and subsequent subgrain sizes, that are clearly evident in the experimental results.

5.3. Modeling Asperity Contact

In virtually any realistic wear scenario, the contacting surfaces are non-ideal. They are generally never atomically smooth, and often contain large asperities and other imperfections. Furthermore, as wear progresses, debris can be produced when material from either or both contacting surfaces is ejected, and material from one surface can be transferred and adhere to the other. These unavoidable phenomena can be critical to a meaningful description of deformation during wear, primarily because the stresses generated by contacting bodies increases as the effective contact area (and therefore the contact pressure at constant load) decreases.

Incorporating a description of asperity contact into the wear model is a simple matter of adjusting the value of the "indenter" radius, R, in Equ 5.1. When contact is mediated by asperities, R represents the characteristic length of the effective contact area. Furthermore, if we assume that the contact is dynamic, perhaps because it is dependent on wear debris and transfer material that changes during the wear process, then the contact radius, R, can be variable in time to represent the changing nature of the contact geometry. A reduction in R serves to increases the maximum contact pressure, p_o, and therefore to increase the stresses near the contact interface, but it also localizes the stresses to a smaller region as illustrated in Fig 5.3.

5.4. Deformation Under Asperity Contact

Figure 5.4 contains plots of equivalent plastic strain and corresponding subgrain size, also extracted from 400 nm below the Ni surface, as functions of wear cycles for a load of $P = 1$ N and a friction coefficient of $\mu = 0.8$. A stochastic description of asperity contact was included, and is meant to model wear debris or other asperities on the Ni surface. Specifically, during each wear cycle, the contact size was taken to be R_1 over a sliding distance of R_1 itself, and $R_2 = 1/16"$ otherwise. The location, relative to the locations of the indenter and ROI, were chosen at random for each cycle. The value of R_1, in nm, was also randomized per cycle according to

$$R_1 = 150\left[1 + \tan\left(\frac{3}{2}\xi\right)\cot\left(\frac{3}{2}\right)\right],$$

(5.10)

where ξ is a random number such that $\xi \in [-1,1)$. The randomization of the asperity size, and especially the asperity location, are evident in the "stair-stepped" shape of the curves in Fig 5.4. Furthermore, the subgrains of only a few nanometers in size for the most heavily-deformed crystallographic orientations, e.g. {110}<211>, are much more in line with experimental observations.

5.5. Modeling the Effect of Deformation on Friction

The model of asperity contact, presented above, succeeds (at least qualitatively) in modeling the evolution of deformation and subgrains during wear. However, the experimental friction measurements clearly show that the friction coefficient depends on both wear (i.e. load and number of cycles) and crystallography. To incorporate these effects into the wear model, we first assume that very small subgrains are able to diffusively rotate in response to a shear stress [5.5]. (We expect this subgrain rotation to occur on a time scale associated with short-range diffusion, and therefore to be slightly slower than dislocation motion, but much faster than the rate of sliding of the indenter itself.) The shear rate, $\dot{\gamma}_{gb}$, of this rotation is

$$\dot{\gamma}_{gb} = \tau \frac{160\Omega}{kT} \frac{D_{bk}}{d^2}\left(1 + \frac{\pi\delta}{d}\frac{D_{gb}}{D_{bk}}\right),$$

(5.11)

where τ is the shear stress at the boundary of the subgrain, Ω is the atomic volume, k is Boltzmann's constant, T is the temperature (taken to be room temperature, $T = 273$ K), d is the subgrain diameter, δ is the width of the grain boundary diffusion path, and D_{gb} and D_{bk} are the grain boundary and bulk diffusivities, respectively, defined as

$$D = D_o \exp\left(-\frac{Q}{RT}\right),$$

(5.12)

where D_o is the diffusion prefactor, Q is the diffusion activation barrier, and R is the universal gas constant. The shear rate due to grain rotation, $\dot{\gamma}_{gb}$, can be converted into an equivalent grain boundary strain, ε_{gb}, i.e. the amount of deformation accommodated by grain boundary sliding, using the same procedure for obtaining equivalent plastic strain, ε_p, in Equ 5.4-5.6.

The experimental evidence strongly suggests that ultra-fine-grained Ni material at the wear surface is responsible for the lubrication seen on some of the crystallographic orientations. Since the present model is not capable of predicting friction or friction coefficient *a priori*, we instead model the influence of microstructure on friction in a phenomenological way. We assume that the ultra-fine-grained material can accommodate deformation through grain boundary sliding, as in Equ 5.11, and that this process is responsible for lubrication. (Consider the analogy between

easily-sliding grain boundaries and graphite layers.) If so, one might expect the efficiency of that lubrication to depend on how much deformation is accommodated by grain boundaries relative to plasticity. To model this, we introduce a phenomenological expression relating the friction coefficient to the distribution of deformation modes, via

$$\mu = 0.2 + 0.6 \exp\left[-2\left(\frac{\varepsilon_{gb}}{\varepsilon_p}\right)\right].$$
(5.13)

Equation 5.13 is merely designed to provide a rapid yet smooth transition between 0.8 and 0.2 as the strain ratio approaches and exceeds unity.

5.6. Friction Evolution During Asperity Contact

Figure 5.5 shows the evolution of the friction coefficient, according to Equ 5.13, for a load of $P = 1$ N, a constant and uniform asperity contact of 200nm (for simplicity), and strain values extracted from 325 nm below the Ni surface. The evolution of the friction coefficient for the {110}<211> wear orientation is qualitatively similar to that observed experimentally, as is the prediction that significant lubrication (at a load of 1 N) only occurs in that orientation and no others.

Table 5.1. Material properties for friction model. (See text for symbol definitions)

Property	Value	Equation
E_{SiN}	250.0 GPa	5.1
ν_{SiN}	0.300	5.1
E_{Ni}	199.5 GPa	5.1
ν_{Ni}	0.312	5.1
D_o	1.9×10^{-4} m²/sec	5.12
Q_{bk}	68,000 cal	5.12
Q_{gb}	34,000 cal	5.12
Ω	0.01128 nm³	5.11
δ	1 nm	5.11
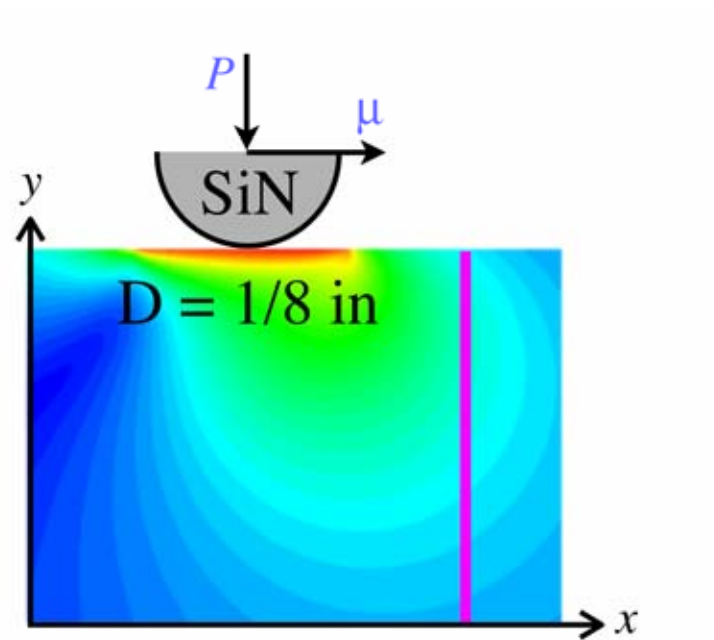
Figure 5.1. Color map of the von Mises stress in Ni in contact with a frictional SiN indenter. Blue represents low stress, and Red is high. The magenta line represents the modeled region.

(a)

(b)
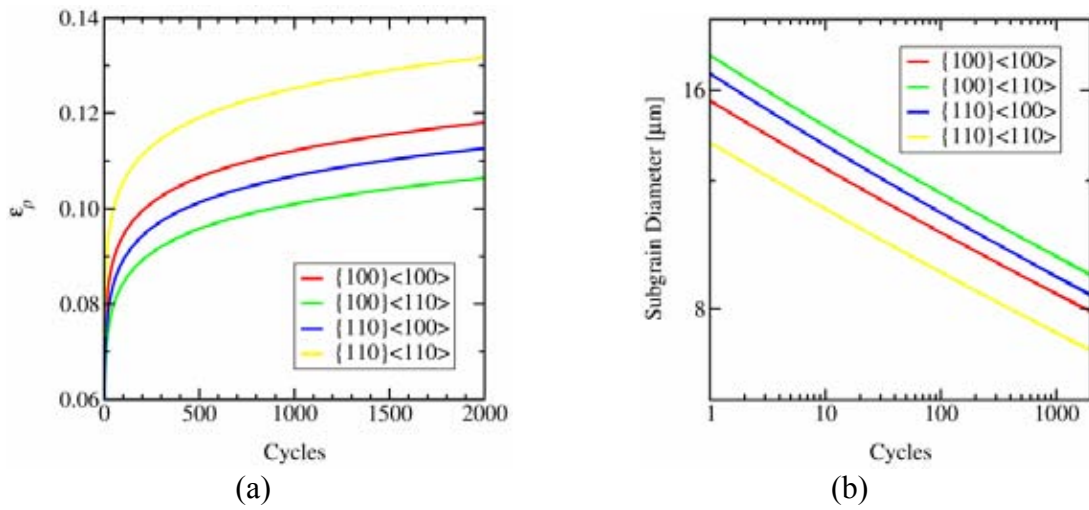
Figure 5.2. Evolution of a) plastic strain and b) subgrain size during wear by a sliding 1/8"-diameter SiN ball on single crystal Ni in four crystallographic orientations. The normal load was $P = 1$ N and the friction coefficient $\mu = 0.8$.
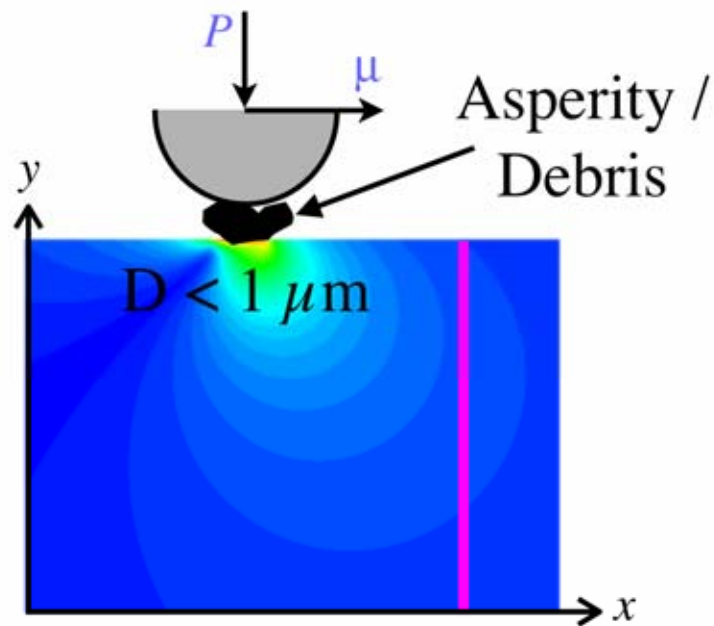
Figure 5.3. Color map of the von Mises stress in Ni in contact with a frictional asperity. Blue represents low stress, and Red is high. The magenta line represents the modeled region.

(a)   (b)
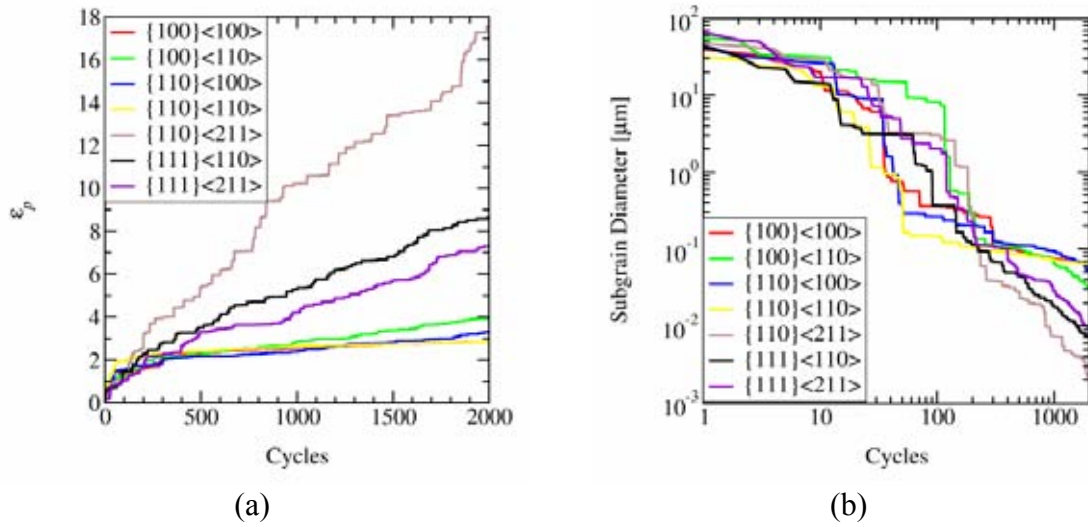
Figure 5.4. Evolution of a) plastic strain and b) subgrain size during wear by a sliding 1/8"-diameter SiN ball with occasional random asperity contact (see text), on single crystal Ni in seven crystallographic orientations. The normal load was $P = 1$ N and the friction coefficient $\mu = 0.8$.
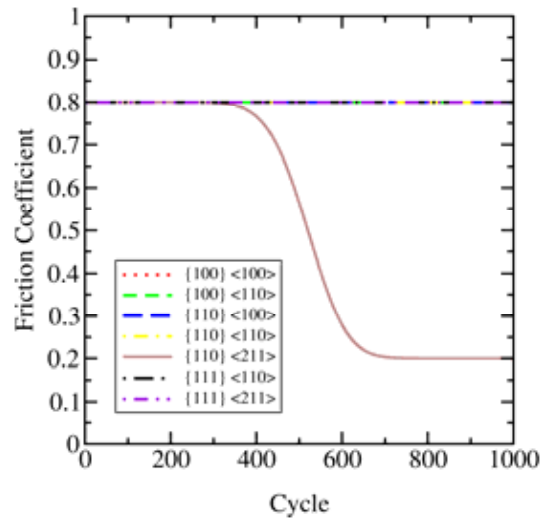
Figure 5.5. Evolution of the friction coefficient during wear by a 200 nm contacting asperity, with deformation accommodation by plasticity and grain boundary sliding, on single crystal Ni in seven crystallographic orientations. The normal load was $P = 1$ N.

6. Mechanical Properties of Wear Surfaces on Single Crystal Nickel

6.1. Introduction

The EBSD analysis presented in Chapter 4 revealed the formation of subsurface recrystallization in single crystals as a result of frictional contact. The objective of this chapter is to evaluate the mechanical properties of wear surfaces on single crystal Ni using nanomechnical techniques. As illustrated in previous sections, the process of wear is multifaceted and depends on environment, composition, surface properties and the contact forces involved [6.1]. What takes place on the surface as well as beneath are important aspects to examine to fully understand the phenomena of wear. Many researchers have observed a reduction in grain size at the near surface under wear scars [6.2-6.7]. The reduction is believed to be due to work hardening of the material and has been the subject of many studies [6.8, 6.9], and the amount of work hardening can easily be accounted for by measuring the hardness of the material. Hardness is a material characteristic which continues to be relevant as new techniques allow us to extend tribological studies into the nanoscale [6.10]. Usually, wear scars would be carefully cross-sectioned and polished for optical examination. This technique is excellent for examining the dislocation cell structure that is formed by the sliding contact, however, mechanical properties of the different cell structures and work hardening regions cannot easily be probed this way. Previous indentation work by [6.10-6.12] on polished cross-sections of wear scars or inside wear scars has shown that hardness does increase with increasing wear cycles and dislocation density. These studies [6.10-6.12] utilize a Knoop indenter, which is very large compared to the grain size and dislocation cell arrangement observed beneath wear scars. Nanoindentation can be utilized to probe the small volumes of the work hardening regions.

Because nanoindentation is a versatile technique it can provide the elastic modulus, hardness, and yield strength of metals through the Tabor [6.13] relationship. It is one of the few techniques available that can acquire properties of materials in their natural microstructural state without the need of extra sample preparation. Additionally, properties can be determined as a function of contact depth of the indenter through the use of the continuous stiffness method (CSM) [6.14]. A sinusoidal driving force is superimposed on the load while the displacement response is monitored. Small oscillations to the force signal are applied at high frequencies. The displacement of the oscillation is monitored at the excitation frequency with the use of a two-channel, phase-sensitive detector. This can accurately measure displacements as small as 0.001 nm using frequency specific amplification. The difference between the driving force and response gives the phase angle of loading from which stiffness and elastic modulus can be determined [6.14]. This technique is useful when measuring the properties of thin film systems or material systems where it is know that the microstructure changes with depth, as in the case of wear scars in ductile materials.

The nanoindenter can also be used to generate wear using its scanning capabilities. Wear boxes can be formed with the indenter by varying the load and number of passes. Nickel (001) single crystal is examined for its wear properties at the nanoscale. Mechanical properties of hardness, elastic modulus and strain can be studied within wear boxes and conclusions to how wear effects these properties will be discussed.

6.2. Experimental Procedure

A (100) bulk single crystal nickel was polished using standard mechanical and electro polishing methods. Wear boxes were made on the surface using a Hysitron TriboIndenter® and a 1 μm radius conical diamond tip. The loads of the indenter (100 μN, 200 μN, 500 μN, and 800 μN) and passes (1, 2, 5, and 10) were monitored to create sixteen 45 μm square boxes, each with a different wear condition. A 4 x 4 grid of boxes was used to organize the experiment. Each wear box center is 150 μm away from the center of next wear box in both the X and Y directions. The crystal directions, either [100] or [011], were placed so they were parallel to the scanning direction of the indenter tip which moved at a rate of 45 μm/s. Figure 6.1a is a schematic drawing of the experimental set up and Figure 6.1b is a optical image of the wear boxes in on the (100) Ni in the [100] direction.

Atomic Force Microscopy (AFM) was utilized to examine the surfaces of the wear boxes. Both tapping mode (TM) and contact mode (CM) were initially used to determine which method would be better to image through the wear debris. It was found that both methods work well and that the debris will move with either TM or CM. For that reason, CM was used because height values are more accurate compared to TM. RMS roughness values of the box interiors were also measured with the AFM.

Nanoindentation experiments were performed inside each wear box to examine the effects of load and pass number on the mechanical properties of the nickel. An MTS Nanoindenter XP with a dynamic contact module (DCM) head and Berkovich diamond indenter tip (50 nm tip radius) was used to measure properties to a depth of 500 nm in the unworn nickel and in each wear box using the continuous stiffness option at 45 Hz with 2 nm displacement amplitude. Nine indents were performed inside each box.

6.3. Results

Through AFM studies, it was observed that the surface deformation and surface roughness varied with applied load and number of passes. The strongest effect was shown under the highest load (800 μN) tested. Examples of the surfaces can be found in Figures 6.2 and 6.3 for both directions. RMS roughness of the wear box interiors are given in Tables 6.1 and 6.2. As expected, roughness increases with increased load and pass number with the maximum roughness measured for the 800 μN-10 pass box.

Initial nanoindentation results show a transition from single crystal nickel values to polycrystalline values for both elastic modulus and hardness. For example, near surface elastic modulus values reflect single crystal orientation but quickly transitioned to polycrystalline values (Figure 6.4). Load and pass number had little effect on the elastic modulus. On the other hand, load and pass number strongly effected hardness inside the wear boxes. Hardness increased with applied load and number of passes with a strong surface roughness effect, as shown in Figure 6.5.

The large variation in the hardness values are most likely a product of geometry and property gradients. Near surface variations in hardness can be attributed to surface chemical effects, indentation size effects, property variations with depth, and surface roughness. Surface roughness results from the large strains and local strain rate responses during wear pattern generation. The asperities created during wear are high stress and strain energy structures, thus requiring that the probing of properties to use additional factors [6.15]. With the use of a contact area to the first order correction, the geometry (asperities) and material can be experimentally separated. The terms are separated using the P/S^2 approach assuming a constant elastic modulus [6.16, 6.17]. In this case, since the elastic modulus values are relatively constant for all displacements, the correction can be applied. From general indentation mechanics the P/S^2 can be derived

$$\frac{P^2}{S} = \frac{\pi P}{4AE^*} = \frac{\pi H}{4E^*} \qquad (6.1)$$

Where P is the load, S is the stiffness, H is the hardness and E^* is the reduced elastic modulus. Corrected hardness values exhibit a well-defined increase with applied load and number of passes (Figure 6.6).

By applying the P/S^2 correction to all of the indentation results, the effect of load and number of passes can be examined individually. An increase in the number of passes has little effect on hardness and the extent of deformation. For example, the 100 μN load in the [011] direction has an average hardness of about 1.75 GPa for all wear boxes (Figure 6.7a) while the surface roughness slightly decreases. At the same time the 800 μN loaded wear box roughness dramatically increases with pass number but again the average measured hardness values for each box is 2 GPa (Figure 6.7b). Conversely, increasing the applied load leads to a significant increase in hardness as well as the extent of surface deformation. Figure 6.8 illustrates the effect of the load for the wear boxes in the [011] direction; the higher the load the higher the average.

6.4. Discussion

Cross plots (Figure 6.9) show that increase in the applied load leads to a significant increase in hardness within the wear patterns (in the [011] direction). The lack of cyclic pass effect contrasts with the change in the wear surface appearance. The same behavior was observed in the wear boxes along the [001] direction. This phenomenon could be due to the fact that the wear mode is changing with load and not with the number of passes. Hokkirigawa and Kato [6.18] have described three modes of wear that dominate when an indenter is used to generate wear.

The modes are plowing, wedge formation and cutting and depend on hardness and geometrical factors with the displacement of the indenter being the most important [6.10]. With this information in mind, it is easy to understand why the hardness of single crystal nickel has a load dependence and not on the number of passes: the larger the load on the tip the larger the initial displacement and thus different mode of wear. AFM images (Figures 6.2 and 6.3) also agree with this hypothesis. The surface morphology changes more with load than with the number of passes.

Continued examination of the gathered data indicates that the stress-strain relationship for each wear box can be measured. Using a simple algorithm, the evolution of the deformation under a rigid indenter can be described [6.19]. By assuming the stress and strain states maintain radial symmetry, the change in contact area to plastic zone radius (da/dc) is

$$\frac{da}{dc} = \frac{\sigma_o}{E}\left[3(1-v)\frac{c^2}{a^2} - 2(1-2v)\frac{a}{c} \right] \tag{6.2}$$

where σ_0 is the yield stress (derived from the Tabor approximation for indentation hardness), E is the elastic modulus, v is Poisson's ratio, and the plastic zone radius, c, is

$$c = \sqrt{\frac{3P}{2\pi\sigma_o}} \tag{6.3}$$

with P representing the load. Equations 2 and 3 are combined to characterize the plastic radial strains as

$$\varepsilon_r^p \approx -2(1-v)\frac{\sigma_o}{E}\left[\frac{c^3}{r^3} - 1\right]. \tag{6.4}$$

Equation 6.4 also applies to deformation under cyclic contacts and from single and multiple cycles of lateral scratches. Stress and strain were measured at a depth of 150 nm within the plastic zone and assuming the indentation size effect was constant for all tests. Figure 6.10 illustrates that there is a strong hardening effect with essentially the same behavior along both the <001> and <011>. The hardening exponent, n for the single crystal nickel is 0.13. These indentation results complement microtensile tests by Allameh et al. [6.20]. They have showed that LIGA nickel properties are higher than bulk nickel and vary strongly with grain size as shown in Figure 6.11. The single crystal work hardening response under nanoindentation follows the evolution of tensile test results with strength.

6.5. Conclusions

In single crystal Ni the extent of deformation increases with applied load and the number of lateral passes. Mechanical properties are affected more by the increase in applied load rather than the increase in the number of passes. Estimates for stress and strain show a strong

hardening response to sliding contact. The corresponding work hardening response under nanoindentation follows the evolution of microtensile test results. The origin of behavior correlates to dislocation emission and slip band formation. Multiple system slip creates a nanocrystalline-like structure and near surface deformation that evolves with load and number of passes.

Table 6.1. Wear pattern RMS roughness (nm) for (001)<001> single crystal nickel using contact AFM.

	100 µN	200 µN	500 µN	800 µN
1 Pass	2.2	1.6	9.6	15.6
2 Pass	2.8	3.5	18.1	21.8
5 Pass	1.2	4.2	16.7	28.5
10 Pass	1.1	4.9	15.0	28.9

Table 6.2. Wear pattern RMS roughness (nm) for (001)<011> single crystal nickel using contact AFM.

	100 µN	200 µN	500 µN	800 µN
1 Pass	2.1	5.2	16.5	16.2
2 Pass	1.7	2.4	12.9	18.6
5 Pass	1.2	2.6	25.0	40.0
10 Pass	1.1	5.0	30.3	40.1
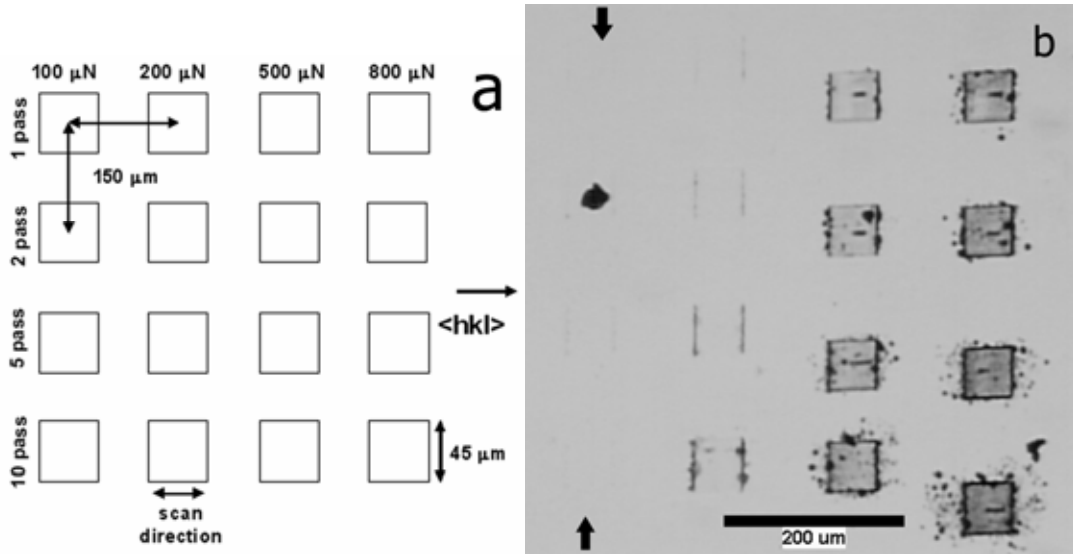
Figure 6.1. (a) Schematic diagram of the wear experiment. (b) Optical micrograph of wear boxes in the [001] on the (001) plane. The arrows indicate where the 100 μN wear boxes are situated.
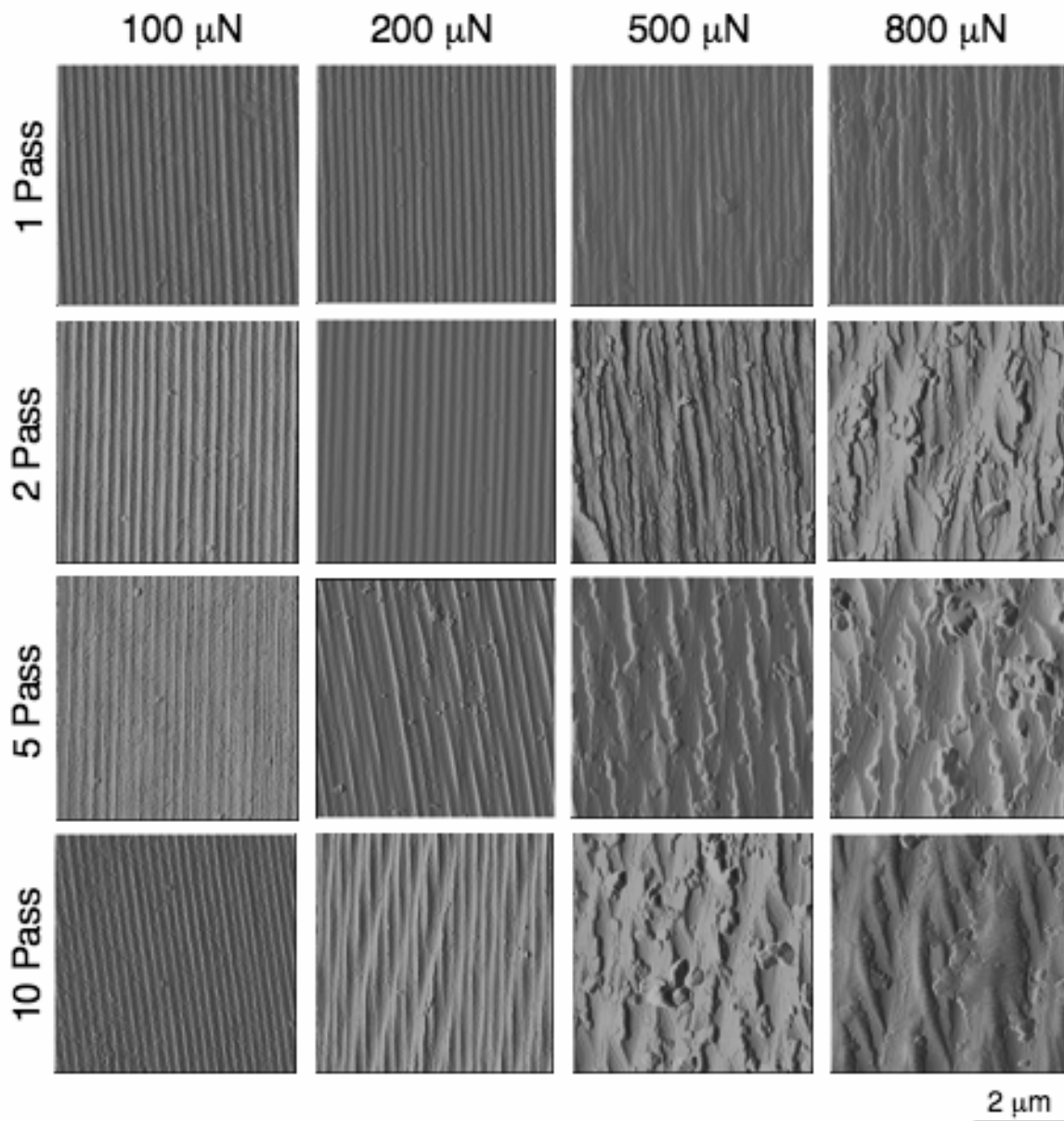
Figure 6.2. 5x5 μm AFM deflection images of all wear box interiors for the [001] direction on a (001) single crystal nickel sample.
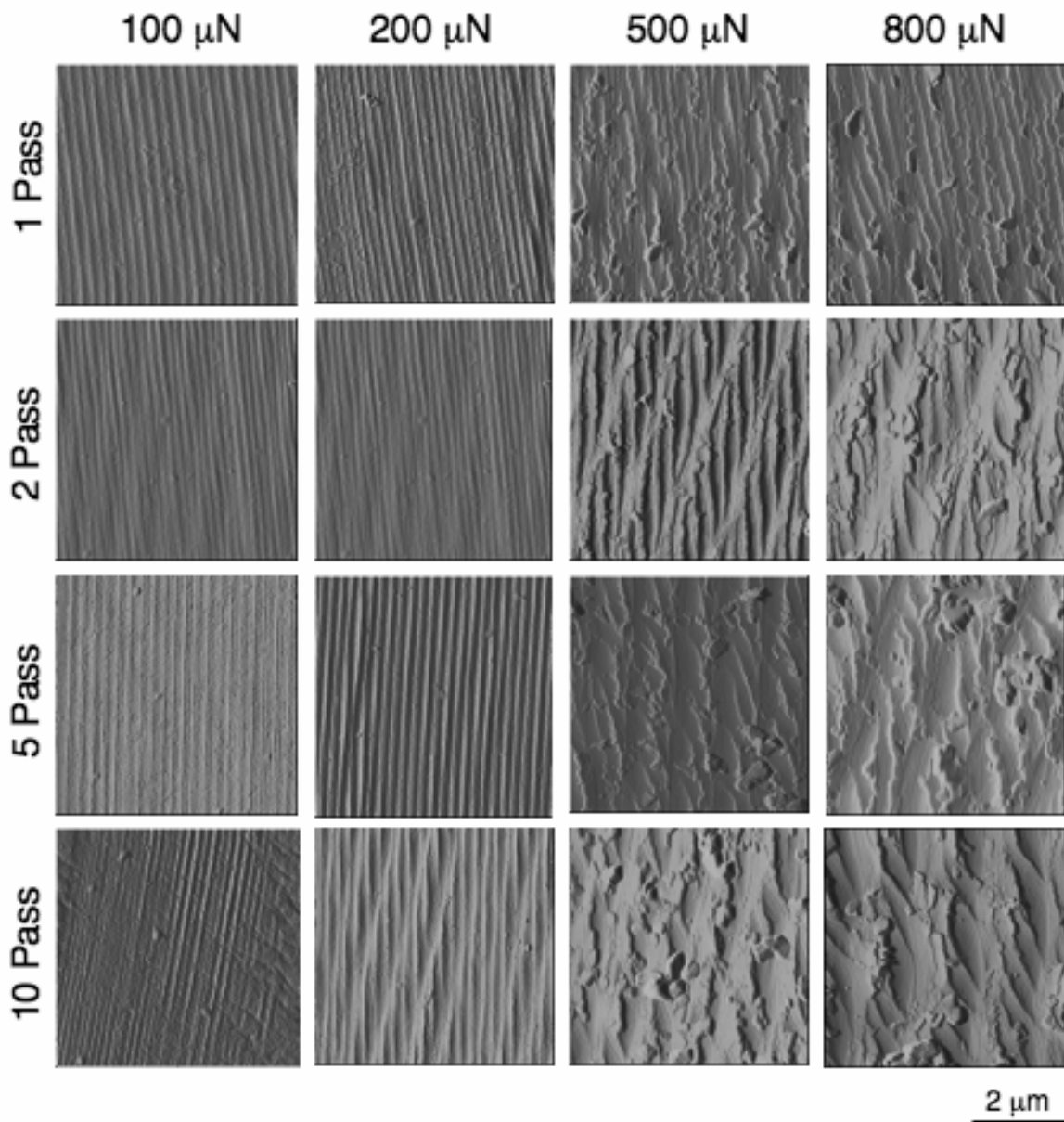
Figure 6.3. 5x5 μm AFM deflection images of wear box interiors for the [011] direction on a (001) single crystal nickel sample.
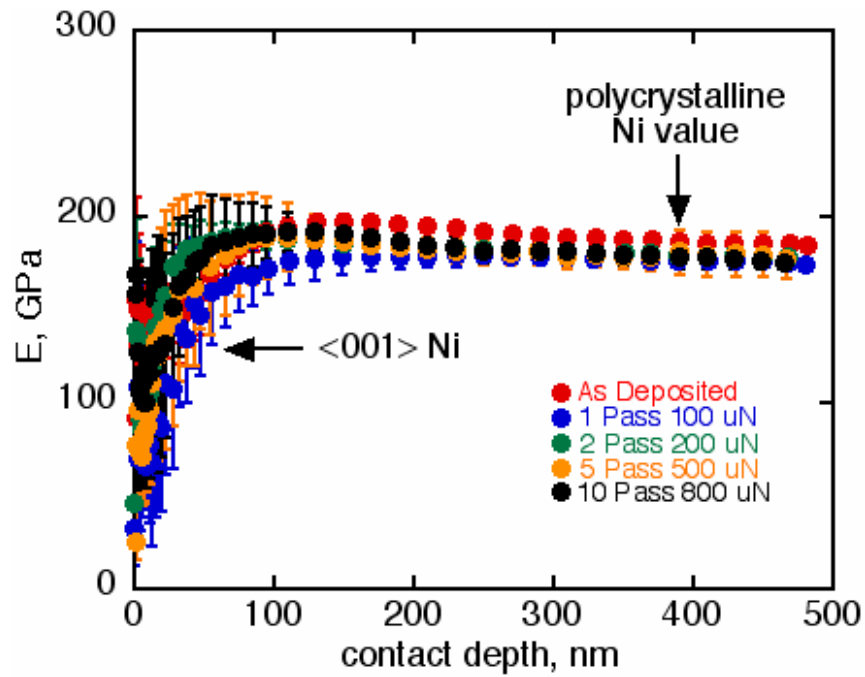
Figure 6.4. Average Elastic modulus for wear boxes in the <011> on the (001) for six indents. The error bars represent the standard deviation. All of the wear boxes have similar values with that of the unworn surface.
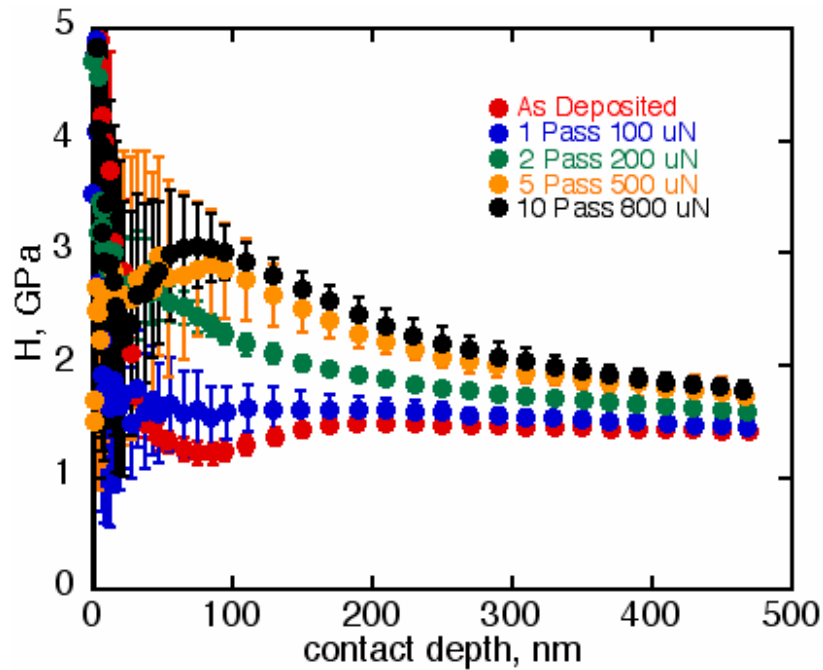
Figure 6.5. Average hardness of six indents inside the wear boxes in the <011> direction on the (001) plane without a roughness correction. The error bars represent the standard deviation of the indents.
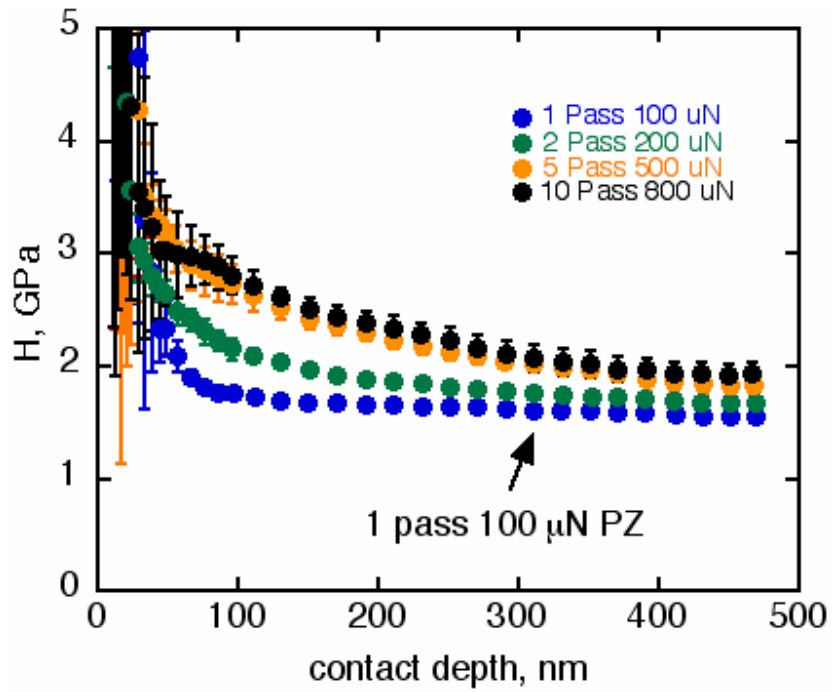
Figure 6.6. Roughness corrected hardness values for the <011> direction on the (001) plane. The error bars represent the standard deviation of the nine indents preformed inside the wear boxes.
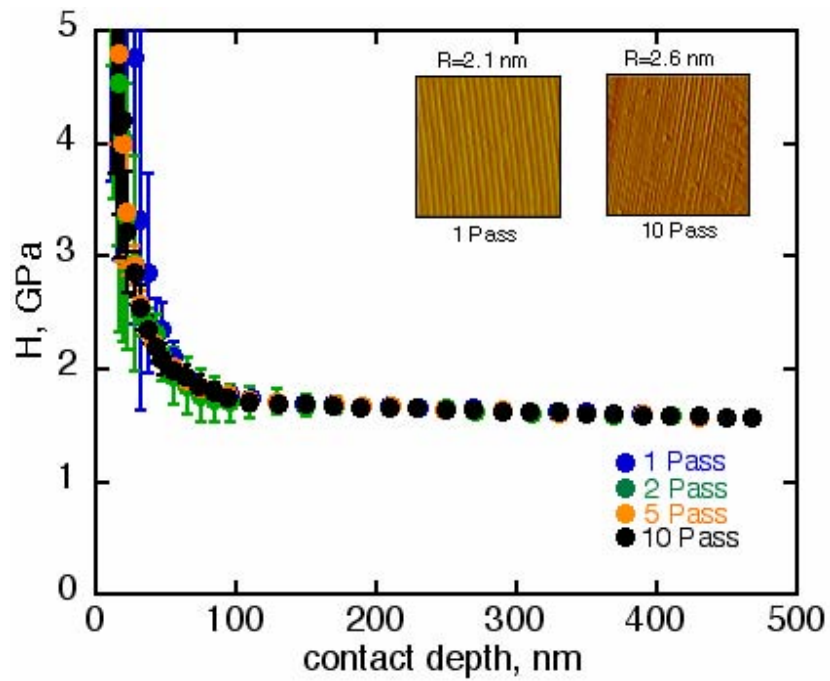
(a)
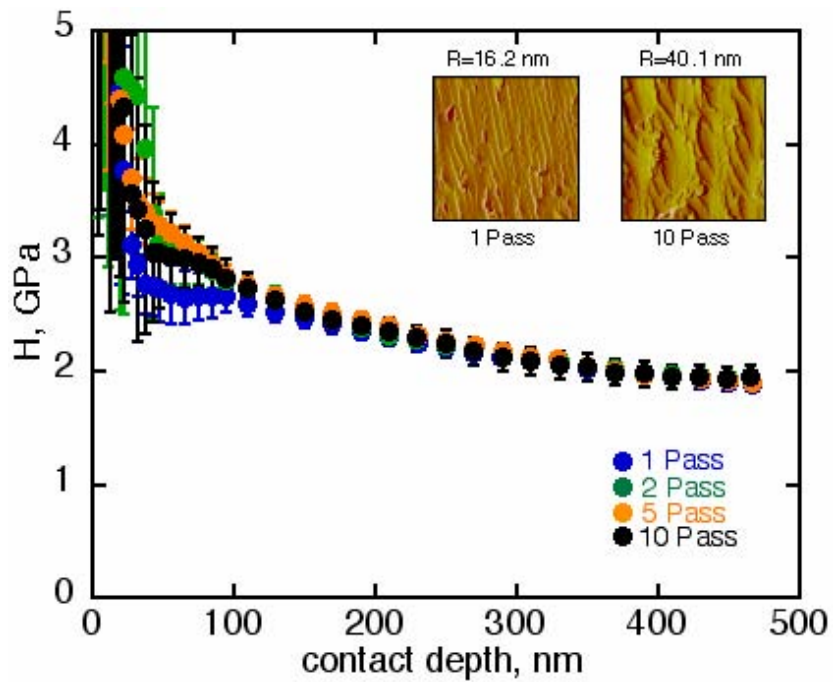
(b)

Figure 6.7. Effect of the number of passes on hardness in the [011] direction on the (001) plane is small. (a) 100 μN loads and (b) 800 μN loads. The error bars represent the standard deviation of the indents.
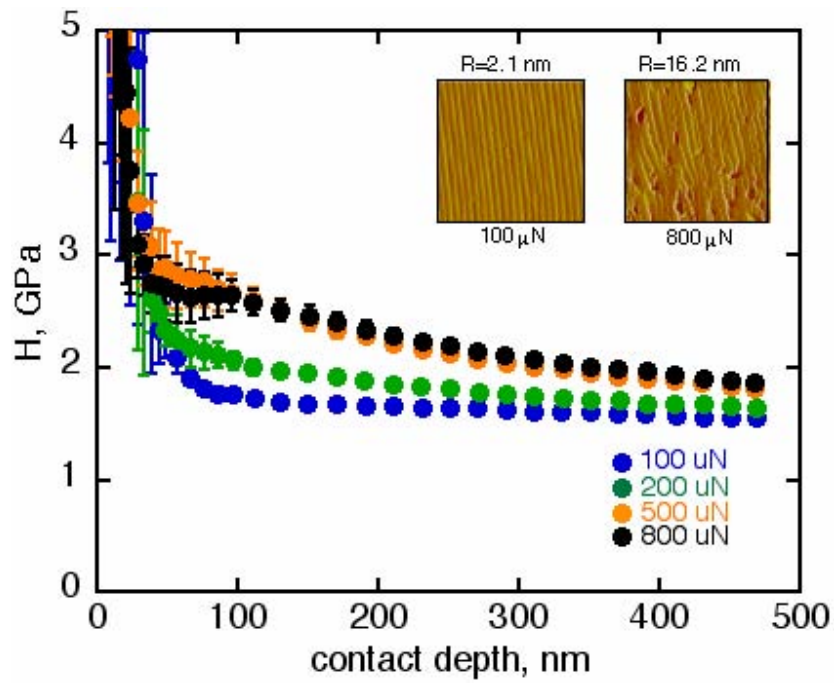
(a)
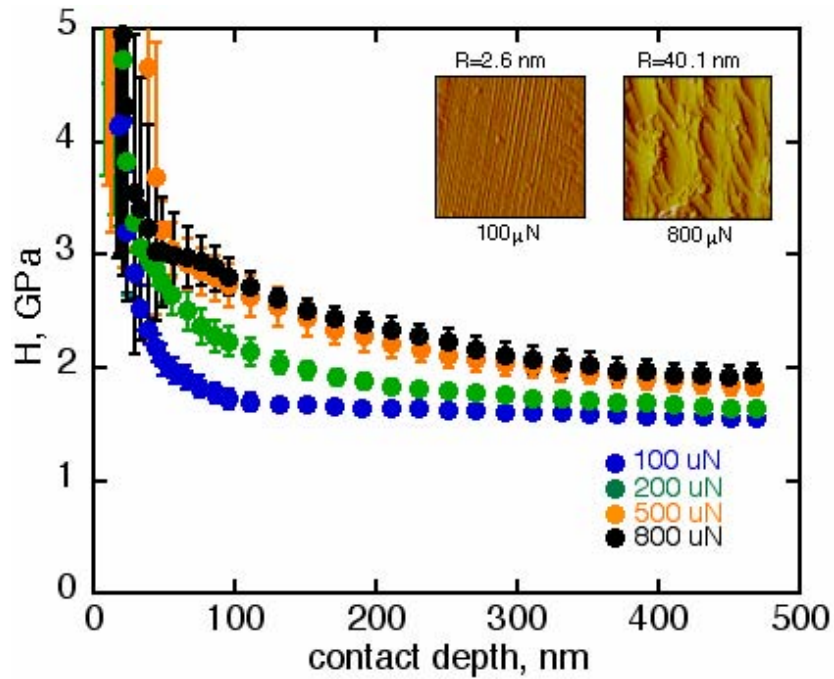
(b)

Figure 6.8. The effect of the applied load on hardness in the [011] direction on (001) crystal surface. (a) 1 pass wear boxes and (b) the 10 pass wear boxes. The error bars represent the standard deviation of the indents.
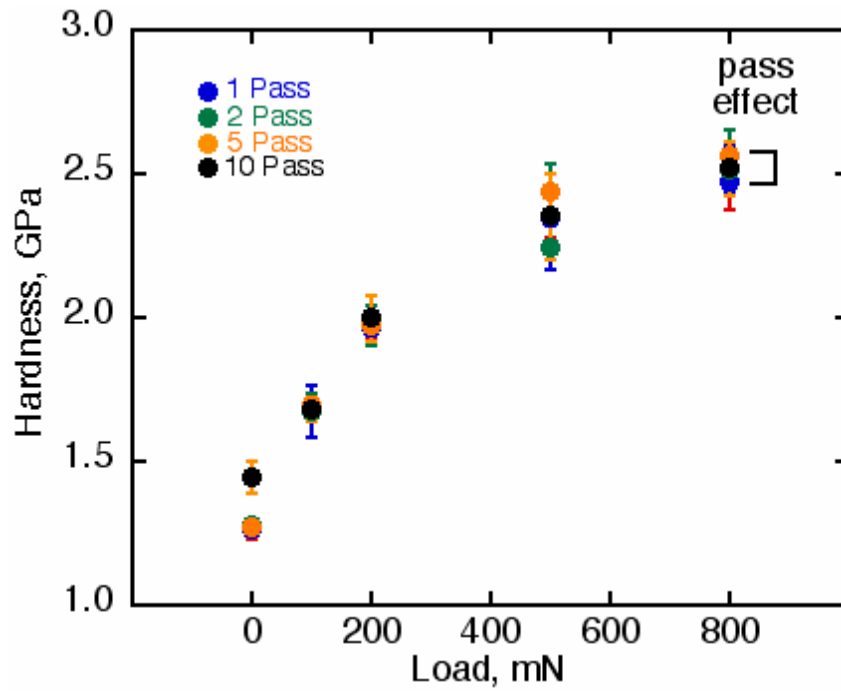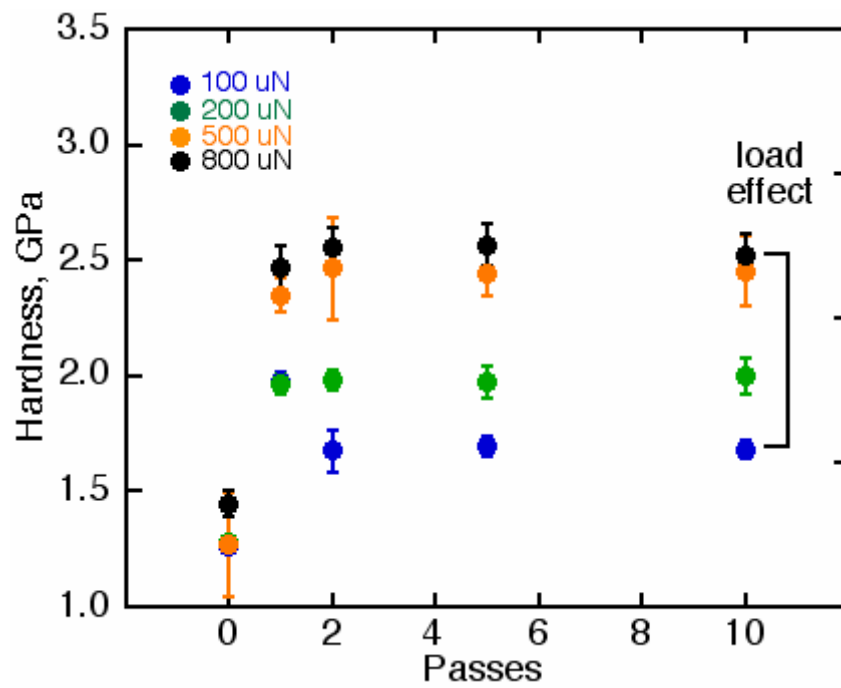
Figure 6.9. (a) The number of passes has a small effect on the hardness of the wear boxes overall in the [011] on (001). However, the applied load (b) has a much larger effect on the measured hardness. The error bars represent the standard deviation.
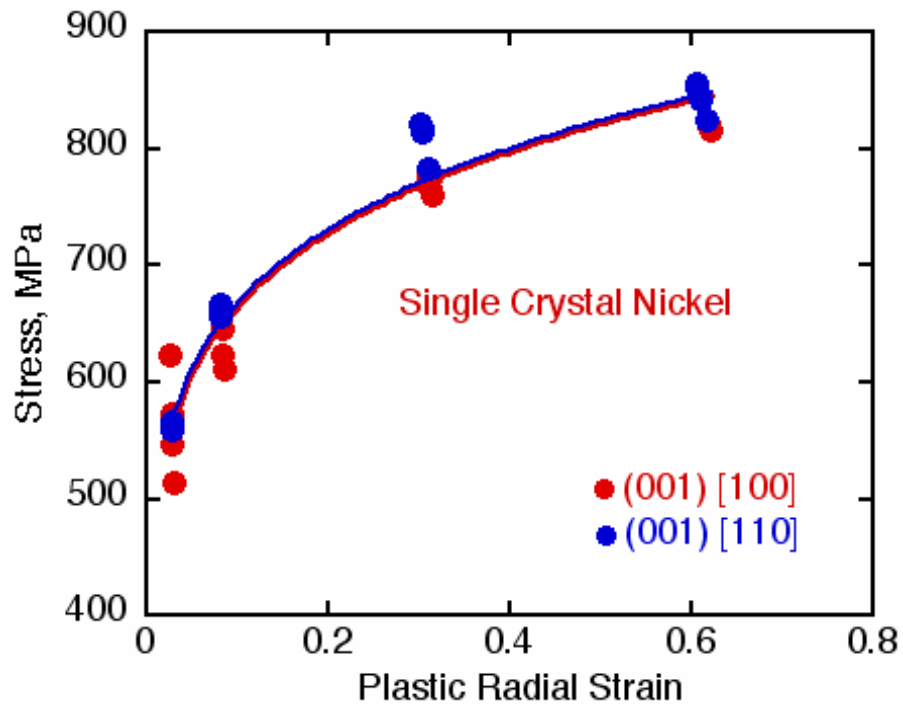
Figure 6.10. Stress –strain relationship of the (001) Ni crystal in the [001] and [011] directions.
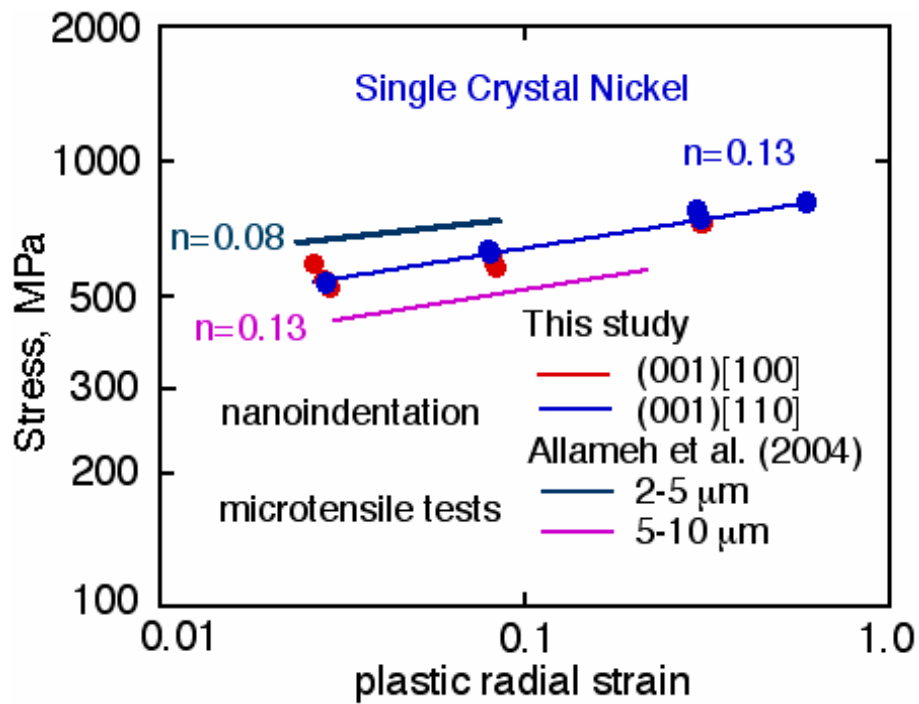
Figure 6.11. Comparison of the nickel data to that of microtensile data. The results of the indentation of single crystal nickel fit within the small grained data of Allameh et al.[6.20].

7. Nanomechanics-Based Approach for Characterizing the Mechanical Response of Wear Surfaces

7.1. Introduction

As seen in the previous chapters, frictional contact induces surface near surface microstructrural changes in metallic materials. These observations imply that the mechanical behavior of wear surfaces can be significantly different from that of the bulk. Since the surface interactions dominate as machine scale is reduced, the mechanical behavior of friction-induced subsurfaces will play a crucial role in determining the reliability of the Microsystems. The focus of this chapter is to develop a nanomechanics-based approach to characterize the mechanical response of wear surfaces with particular relevance to LIGA-fabricated Microsystems. In recent years, LIGA (a German acronym for "Lithographie, Galvanoformung, Abformung") has emerged as an important technology for fabricating small-scale high precision MEMS structures with applications that range from accelerometers for airbags and heat exchangers to gear-trains and comb drives. [7.1-7.3] In this process, metals or alloys are typically electrodeposited into lihthographic micromolds to create high aspect ratio parts which can be assembled into micromachines. [7.4] Nickel is often the metal of choice as its electrodeposition chemistry is well understood, and Ni electrodeposits have good mechanical properties and corrosion resistance. [7.4-7.6] Moreover, the development of nickel-based binary alloys provides materials with a range of properties. [7.4, 7.7-7.9] The strengths of these alloys are higher than those of bulk nickel and in some cases much higher. As shown by Hemker and coworkers [7.10, 7.11] and later by Buchheit et al. [7.4, 7.7, 7.12], strengths in these alloys can approach 1000 MPa in the as-deposited condition by varying plating bath chemistry and current density. However, they also exhibit significant anisotropy in mechanical response and variability in properties, even between electrodeposits of the same material. [7.4] As a consequence, recent studies [7.4, 7.12] have focused on defining structure-property relationships in LIGA-fabricated nickel and nickel alloy structures.

In many Microsystems applications, sliding contacts often determine performance and reliability. [7.1] The regions below the sliding contacts are severely stressed and give rise to acute gradients of plastic shear strain [7.12-7.16] which accumulates with continued sliding. [7.17] These strains can easily exceed 10 near the wear surface [7.17-7.20] and have been estimated to approach 100. [7.20-7.22,] Strains of these magnitudes can markedly change surface roughness, hardness, grain size, and texture. [7.1, 7.21] But they also decrease rapidly with distance from the surface creating a gradient of microstructures and deformation substructures. [7.13, 7.17, 7.19] The gradients in microstructures and deformation substructures can lead to strong gradients in mechanical response. As a consequence, characterizing the mechanical behavior of material under wear surfaces is crucial to predicting the performance and reliability of micromachines.

Numerous studies have addressed the evolution of microstructure under wear surfaces. [7.1, 7.2, 7.13, 7.19, 7.21, 7.23] See also the many references cited therein. In work-hardening alloys, high surface strains under sliding contacts lead to formation of a hard surface layer of small subgrains. [7.13,7.18,7.22,7.24] Farther from the surface, structure is characterized by the formation of dislocation cells that increase in size with an increase in distance from the surface. [7.13, 7.19, 7.22] The same evolution is observed in cold-rolled nickel where there is a change from a nanoscale structure in the surface region to deformation substructures, and a mixture of small and large angle dislocation boundaries in the deeper regions. [7.23] These structures become increasingly finer with increasing strain. Under extreme strains, the local dislocation density can be two orders of magnitude greater than conventionally cold-worked metals. [7.23] The evolution in microstructure and deformation substructures creates a positive hardness gradient as one moves from the bulk material to the sliding interface. [7.17, 7.24]

Studies on friction, wear, and mechanical behavior of LIGA-fabricated nickel have focused on behavior at the macro and micro scales. [7.4, 7.12] In this study, we focused on behavior of electrodeposited nickel at the nanoscale. Nanoscratch techniques were used to generate wear patterns, Atomic Force Microscopy was used to characterize surface topology, and nanoindentation was used to measure properties in each wear pattern. The results showed that increases in applied load and the number of nanoscratch passes systematically increased hardness. The results also follow behavior established from tensile tests at larger scales, supporting use of a nanomechanics-based approach for studying mechanical properties of wear surfaces.

7.2. Materials and Procedure

7.2.1. Materials

The electrodeposited nickel test coupons were prepared by mimicking the LIGA process. A UV mask with a two-dimensional array of 10 mm x 10 mm squares was used to create an array of micromolds in a 500 μm thick photoresist layer on a metallized silicon substrate. [7.1] Nickel was electroplated into these micromolds from a sulfamate bath followed by a surface lapping procedure following standard metallographic procedure. The photoresist mold material was dissolved leaving Ni coupons on the substrate. The substrate was then diced to obtain individual test coupons. For this study, the test coupons were not released from the substrate. Chemistry of the sulfamate bath and details of the deposition process are given elsewhere. [7.25]

The microstructure consisted of 1 to 2 μm wide columnar laths that extended through the sample thickness, which is typical of most electroplated materials. [7.1, 7.4] The laths also contained a high density of twins. [7.1] Automated orientation analysis of focused ion-beam (FIB) cross-sections revealed that the coupons had a strong <001> texture consistent with previously reported electron backscatter diffraction (EBSD) data. [7.1, 7.4] Lapping also led to near surface damage and formation of a thin (~30 nm) fine-grained surface layer. [7.1]

7.2.2. Procedure

Nanoindentation and nanoscratch tests were then performed to study the effects of friction and wear on mechanical properties of electrodeposited nickel surfaces. The experiments consisted of generating 4x4 matrices of 40x40 μm square wear patterns spaced 100 μm apart at loads of 100, 200, 500, and 800 μN using a Hysitron Triboindenter with a 1 μm radius conical diamond tip. (Figure 7.1) Each load was applied for 1, 2, 5, and 10 passes. The patterns were generated at 0.5 Hz giving an effective sliding rate/velocity of 20 μm/s. A final scratch test was run on each wear pattern at the load and rate used to generate the pattern while monitoring normal and lateral forces to determine the coefficient of friction for each wear test condition. Atomic Force Microscopy (AFM) under tapping and contact mode was then used to characterize the effect of applied load and number of wear passes on surface topology.

A Nano Instruments XP with a Dynamic Contact Module and a nominal 50 nm radius Berkovich diamond indenter was then used to measure properties to a depth of 500 nm in each wear pattern. The tests were conducted in the continuous stiffness mode which superimposed a sinusoidal signal at 75 Hz and amplitude of 2 nm. Indentation tests were also run on the unworn surface for reference. All indentation tests were run at a constant nominal strain rate of 0.05 s^{-1}.

Modulus was determined from measured stiffness values and projected contact areas using the analysis of Oliver and Pharr [7.26] as follows,

$$S = \beta \frac{2}{\sqrt{\pi}} E * \sqrt{A} \qquad (7.1)$$

where

$$\frac{1}{E*} = \left| \frac{\left(1 - v_i^2\right)}{E_i} + \frac{\left(1 - v_s^2\right)}{E_s} \right| \qquad (7.2)$$

In these expressions, S is the stiffness, P is the load, A is the projected contact area, β is a tip shape correction factor equal to 1.034 for a Berkovich indenter, and E* is the reduced modulus composed of the moduli, E_i and E_s, and Poissons ratios, v_i and v_s, for the indenter and the sample respectively. Contact areas were determined using a nine-order polynomial tip shape function derived from tests on a fused silica standard. Hardness was determined from the classical definition of H=P/A. Six indentations were conducted in each pattern to measure modulus and effective hardness maintaining a 15 μm minimum spacing between indentations to avoid indentation interactions. Indentations were also run on multiple patterns for each condition to generate statistically accurate property measurements.

7.3. Results and Discussion

7.3.1. Topography and Structure

AFM revealed a significant change in topography with an increase in applied load, and to a lesser degree with an increase in the number of wear passes as shown in Figure 7.2. Wear surface appearance paralleled previous studies that characterized wear as a transition from mild to severe that occurs over a range of sliding conditions (load and velocity). [7.27,7.28] After one pass, deformation created a smooth sliding surface characterized by parallel shallow grooves and smooth ridges. At 500 μN, deformation began taking on a 'woven' appearance with the groves and ridges making numerous small changes in direction with each pass. These effects became pronounced at 800 μN with the ridges exhibiting extensive lateral extrusion of material.

A change in RMS roughness was also observed as noted for each condition in Figure 7.2 and for all conditions in Table 7.1. When compared with the as-lapped surface roughness of 10 nm, roughness as the wear load and the number of wear passes increased. The roughest surface was generated under the most severe wear pattern conditions (800 μN/10 pass). The measured coefficients of friction mirror these effects with the coefficients increasing with increasing load and number of scratch passes. (Table 7.2)

Pin-on-disk tests by Prasad and coworkers [7.1] on electrodeposited nickel samples from the same production lot as used in this study showed structure evolved with depth beneath the wear track. For several microns under the wear surface, frictional forces deformed the nickel, bending the columnar grains in the direction of sliding. Immediately beneath the wear surface, these forces created a submicron size, equiaxed grain structure. [7.1] These structures are typical of those found in metals subjected to severe working [7.13,7.15,7.18,7.21-7.23,7.27] and indicate that frictional forces have generated very large plastic strains in the severely deformed near surface material. [7.19,7.22]

7.3.2. Properties

Nanoindentation results for the undeformed nickel and the wear patterns along the matrix diagonal are given in Figure 7.3. The results are typical of all tests in this study and were selected to show the effect of increasing wear load and number of wear passes on material response without masking individual test results. Nanoindentation gave an undeformed electrodeposited nickel a modulus of 190 GPa, which is in good agreement with bulk nickel values and with previous work on electrodeposited nickel. [7.12] However, elastic moduli exhibited a systematic decrease in near surface values with increasing load and number of wear passes. There was also a pronounced increase in scatter. The near surface decrease in modulus with increasing load and number of wear passes is directly attributable to the effect of decreasing contact area with increasing surface roughness [7.14] which became pronounced when the test depth was comparable to the scale of roughness. As test depth increased, the measured modulus for each condition approached the undeformed, flat surface modulus of 190 GPa.

The measured hardness of 1.6 GPa for the as-lapped undeformed nickel was higher than the value of 1.3 GPa typically associated with bulk nickel but consistent with tensile test results in electrodeposited nickel. [7.12] Within the wear patterns, near surface measured hardness values exhibited a stronger effect of scatter than the modulus values. There was also a strong variation with indentation depth. Nevertheless, there was a trend of increasing hardness with increasing load and number of lateral scratches. For additional clarification, it should be noted that the LIGA nickel is undeformed and the single crystal nickel is deformed. Nevertheless, the LIGA nickel is harder than the single crystal nickel at all deformations due to the differences in microstructure; however, both systems exhibit the same trends with increasing load.

7.3.3. Roughness Corrections

The variation of hardness with indentation depth is a compound effect of surface roughness and property gradients. [7.14, 7.29] Separating the roughness effect from the measured values gives the variation in hardness with applied load, number of lateral scratches, and contact depth. [7.14]

A first order estimate of actual hardness values can be determined experimentally following the approach of Joslin and Oliver [7.30] and Page and co-workers [7.31] to correct for roughness effects on contact area of bulk materials and more recently by Saha and co-workers to correct for hardness effects on thin film measurements.

Setting the elastic modulus for electrodeposited nickel equal to measured value of 190 GPa, hardness was determined directly from measured load and stiffness values as follows,

$$H = \frac{4E^{*2}P}{\pi S^2} \qquad (7.4)$$

where

$$\frac{1}{E^*} = \left| \frac{\left(1 - v_i^2\right)}{E_i} + \frac{\left(1 - v_s^2\right)}{E_s} \right| \qquad (7.5)$$

In these equations, P is the applied load, S is the stiffness, and E_i and v_i and E_s and v_s are the elastic moduli and Poissons' ratios for the diamond indenter and the sample respectively. The approach corrects for roughness effects on contact area giving a first order estimate of actual hardness values as a function of test depth. It also corrects for pile-up and sink-in effects on contact area, which can be pronounced at shallow depths. It does not correct for second order effects such as asperity size effects on near surface yield strength. We also ignore any variation influenced by the method of measurement and instrument errors in depth-sensing measurement and any disruptive effect of the indenter on the hardness measurement. [7.14]

This correction was applied to all test data. As shown in Figure 7.4 for the diagonal wear patterns, correction for roughness effects reveals that hardness exhibits a strong increase with increasing applied load and the number of lateral scratch passes. The extent of the plastic zones (eq. 7.6) in patterns generated at applied loads of 100 μN and 800 μN are indicated by the arrows in the figure. [7.32] Selecting data at applied loads of 100 and 800 μN in Figure 7.5 and at 1 and 10 passes in Figure 7.6 which have been corrected for roughness using this approach show hardness increases systematically with increasing applied load and to a slightly lesser extent with an increase in the number of wear passes. The effect of increasing applied load and number of wear passes is clearly shown in Figure 7.7 for cross plots of hardness at a contact depth of 150 nm. This depth is within the plastic zone size for all test conditions. It also put the point of analysis beyond the effect of strong indentation size effect gradients and beyond the effect of asperity interactions. [7.14] These results parallel observed changes in topography and roughness, and with the coefficients of friction. They also parallel previous work showing that the amount of strain in the near surface region increases with the number of sliding contact passes. [7.15,7.33]

7.3.4. Stress Strain Response

Gerberich and co-workers [7.33] demonstrated a direct link exists between measured hardness and the extent of plasticity for micro and nanoscale compressive contacts using a simple algorithm derived following the same approach Johnson used to derive his cavity model. [7.32] The core assumption is that the stress and strain states maintain radial symmetry when a rigid indenter tip is driven normally into the surface. With this assumption, the plastic radial strain within the plastic zone is given by, [7.32]

$$\varepsilon_r^p \approx -2(1-\nu)\frac{\sigma_{ys}}{E}\left|\frac{c^3}{r^3}-1\right| \tag{7.5}$$

where the plastic zone size, c, is given by [7.32],

$$c = \sqrt{\frac{3P}{2\pi\sigma_{ys}}} \tag{7.6}$$

and the yield strength is approximated by,

$$\sigma_{ys} = \frac{H}{3} \tag{7.7}$$

In these equations, ε_r^p is the plastic radial strain, σ_{ys} is the yield stress, r is the distance from the point of contact, and c is the extent of the elastic-plastic boundary. This is identical to the solution readily obtainable from small deformation theory. [7.32]

We applied this approach to our results at a contact depth of 150 nm. As noted in the discussion of roughness effects, this depth put the point of analysis beyond surface roughness effects and within the plastic zones for all test conditions. The formulation used here is derived from the plastic radial strain based on Hill's slip line solution used in the widely accepted expanding cavity model for plastic zone formation beneath an indenter. More importantly, it has been shown to accurately describe pileup due to dislocation processes in ductile metals. We also assume that the indentation size effects are the same for all tests. This assumption is supported by data on gold films showing that indentation size effects vary with indenter tip radii but not with variations in film properties. [7.34] The wear pattern data superimpose on a single curve (Figure 7.8) revealing a direct link between the evolution of flow stress and extent of plasticity under single and multiple scratch passes. This is the same behavior observed for the evolution of plasticity under cyclic contacts. [7.33] The behavior did not change as long as the depth chosen for analysis was within the plastic zones for all test conditions.

7.3.5. Work Hardening

These results can be compared to recent micro-tensile test results of Allameh and co-workers [7.12] for electrodeposited nickel structures 70 μm and 270 μm thick deposited by the same sulfamate bath process used to fabricate samples in this study. These structures had columnar widths of 2 to 5 μm for the 70 μm thick structure and 5 to 10 μm for the 270 μm thick structure, which are significantly greater than the 1 μm columnar width of electrodeposited nickel used in this study. As Figure 7.9 shows, there is a systematic increase in strength and decrease in work hardening coefficients with decreasing columnar width. The evolution of work hardening response with increasing yield strength regardless of test technique provides confidence in the use of nanoindentation and nanoscratch tests to study mechanical properties in microdevice materials under service loads.

7.4. Conclusions

In this study, nanoindentation and nanoscratch techniques were used to evaluate the mechanical properties governing performance and durability of wear tested electrodeposited nickel samples. Nanoscratch techniques were used to generate wear patterns using loads of 100, 200, 500, and 800 μN with each load applied for 1, 2, 5, and 10 passes. Nanoindentation was then used to measure mechanical properties in each wear pattern. Correcting for surface roughness gave a first order estimate of actual hardness values as a function of test depth. Roughness corrected values showed that hardness increased with increasing applied load and the number of lateral scratch passes. The results also showed that the work hardening coefficient determined from indentation tests within the wear patterns followed the results established from tensile tests, supporting use of a nanomechanics-based approach for studying mechanical properties of wear tested material.

Table 7.1. Wear pattern RMS roughness (nm) using contact AFM.

	100 μN	200 μN	500 μN	800 μN
1 Pass	2.8	2.4	5.5	23.9
2 Pass	3.5	2.4	7.8	13.1
5 Pass	5.9	3.4	11.9	24.4
10 Pass	3.0	9.1	22.8	26.4

Table 7.2. Coefficients of friction for wear pattern data.

	100 μN	200 μN	500 μN	800 μN
1 Pass	0.35	0.37	0.48	0.52
2 Pass	0.42	0.37	0.58	0.65
5 Pass	0.49	0.40	0.53	0.68
10 Pass	0.39	0.44	0.54	0.54
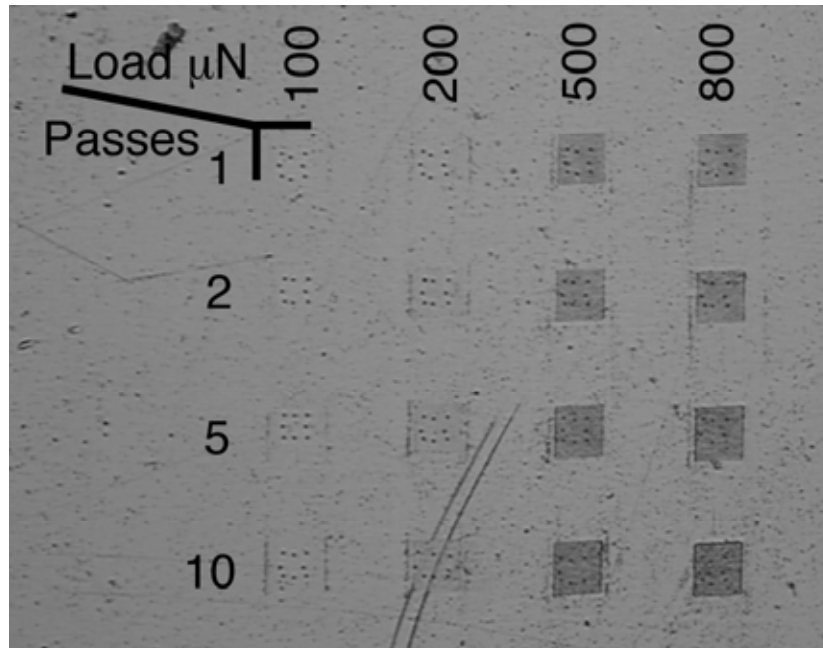
Figure 7.1. A 4x4 matrix of wear patterns were generated on electrodeposited Ni using loads of 100, 200, 500, and 800 µN with each load applied for 1, 2, 5, and 10 passes. Each pattern is 40 µm x 40 µm.
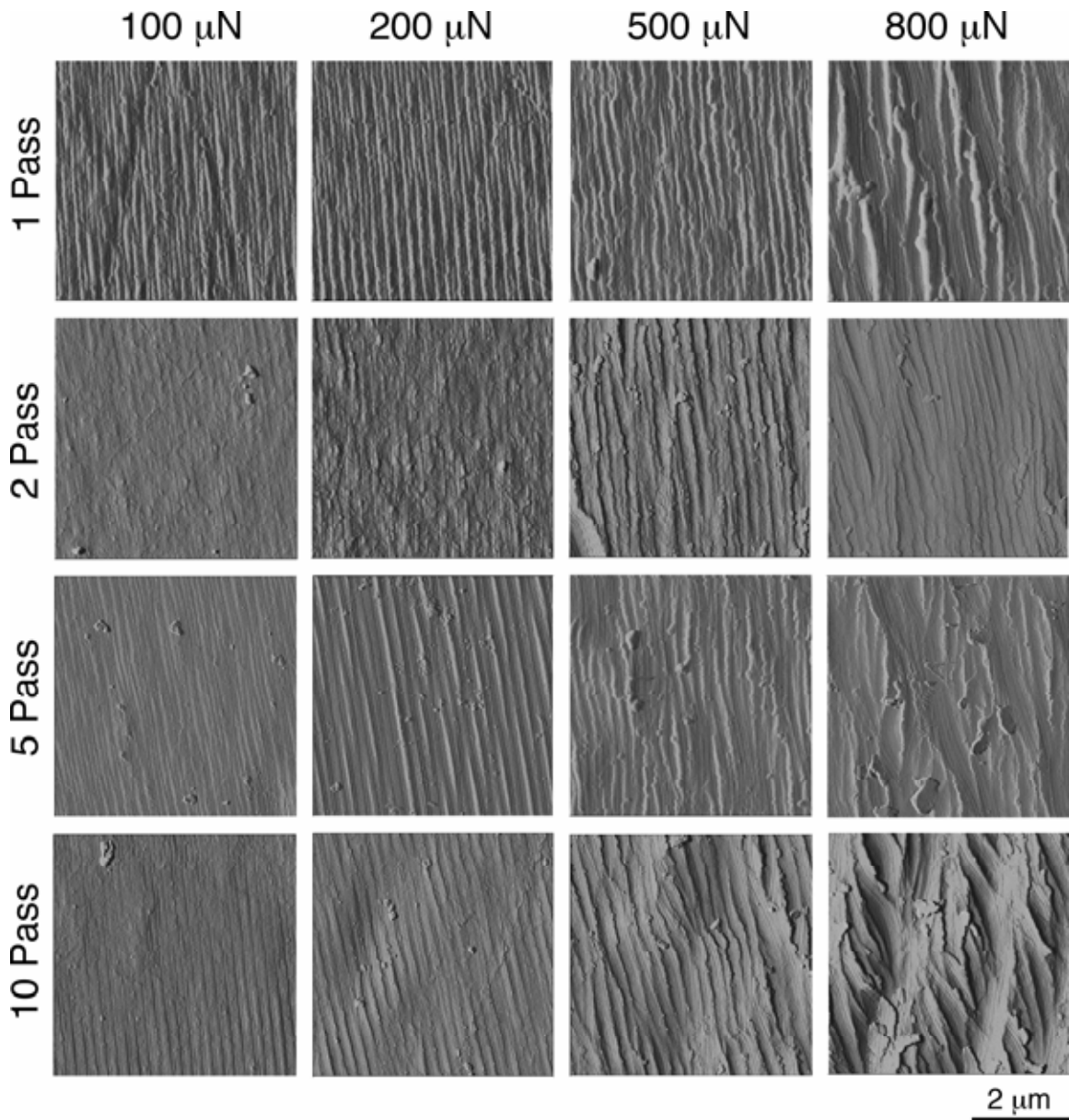
Figure 7.2. Contact AFM showed topography changed from parallel shallow grooves to a woven appearance of grooves and ridges with increasing applied load and number of wear passes. These effects became pronounced at 800 μN with the ridges exhibiting extensive lateral extrusion of material. The surfaces exhibited a parallel change in rms roughness.
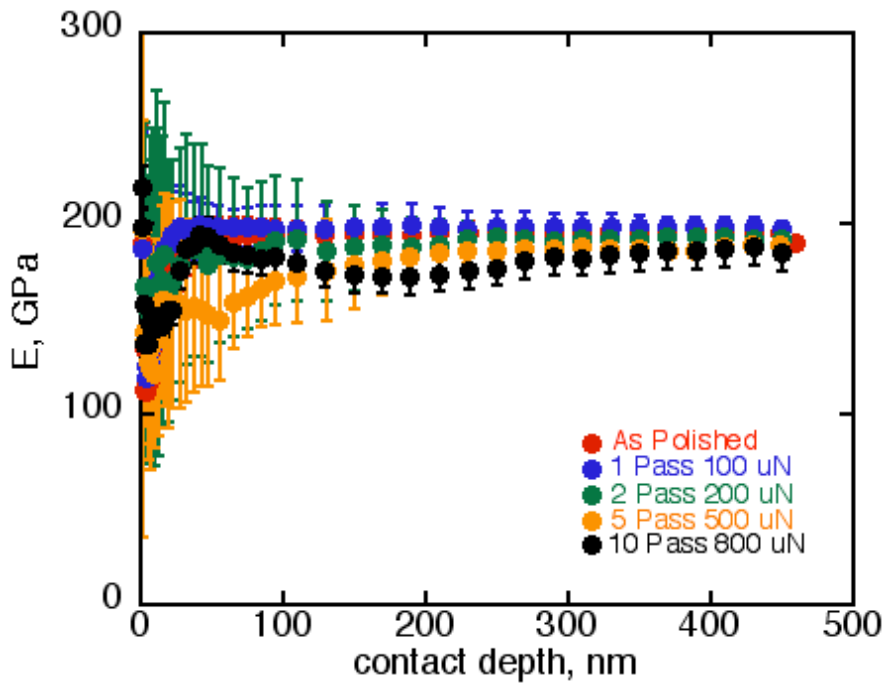
(a)
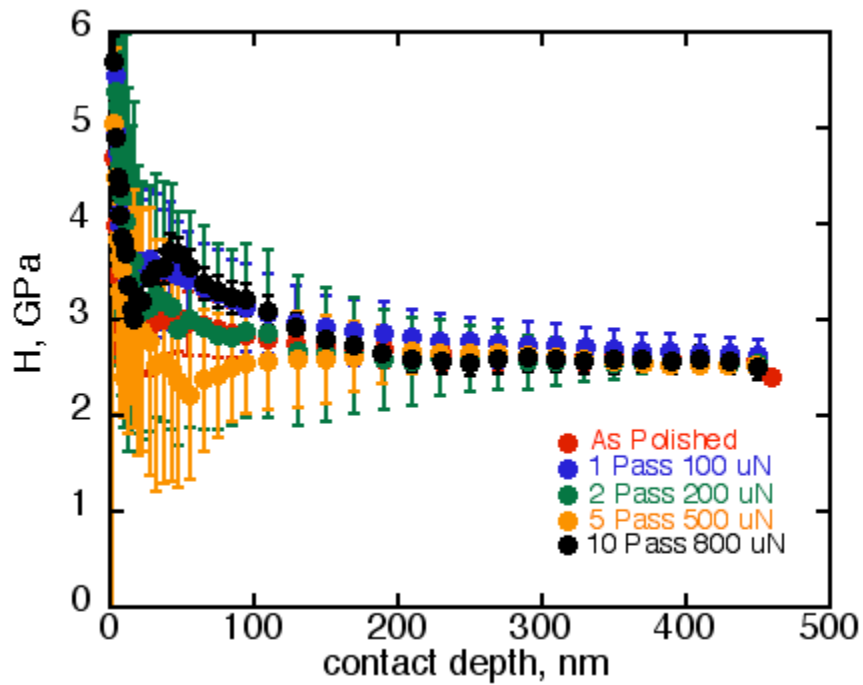
(b)

Figure 7.3. Data from Nano DCM using continuous stiffness at 75Hz with a 2nm amplitude showing effects of wear on (a) as-measured elastic modulus, (b) as-measured hardness.
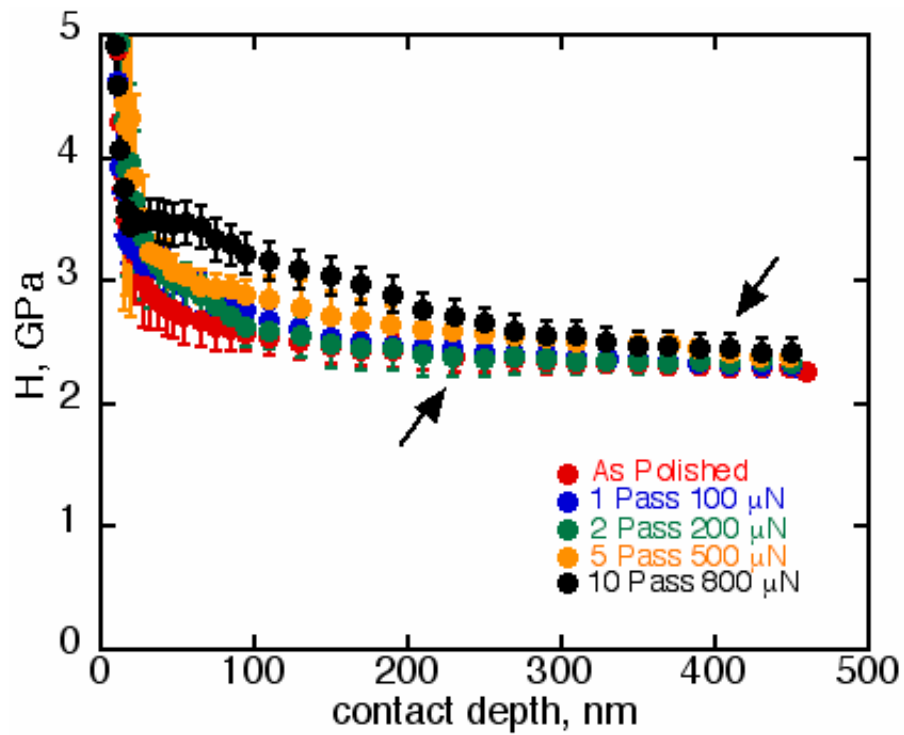
Figure 7.4. Hardness values for the diagonal wear pattern data corrected for roughness exhibit a systematic increase with increasing applied load and number of wear passes. The arrows show the extent of the plastic zones in patterns generated at applied loads of 100 μN and 800 μN.
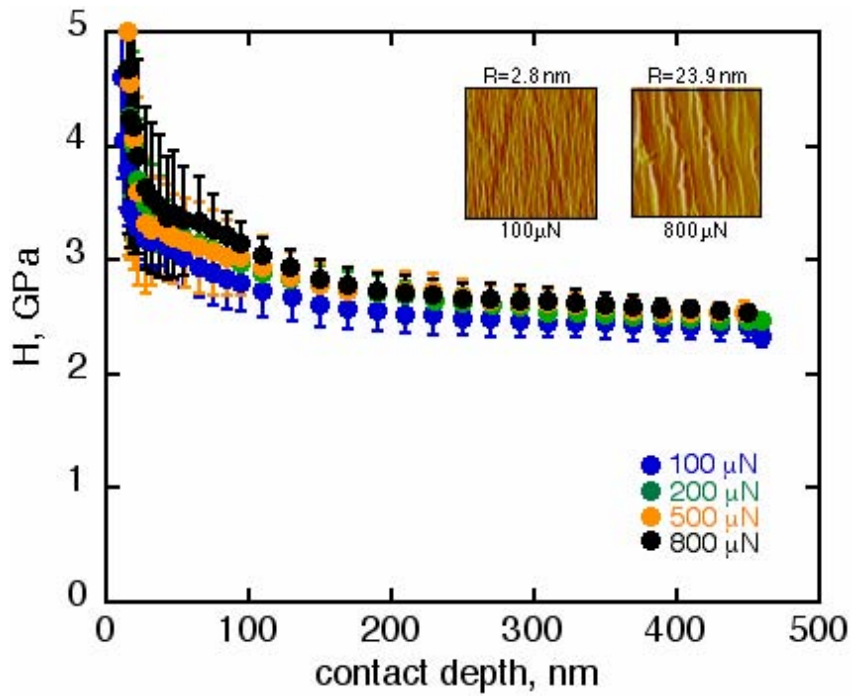
(a)
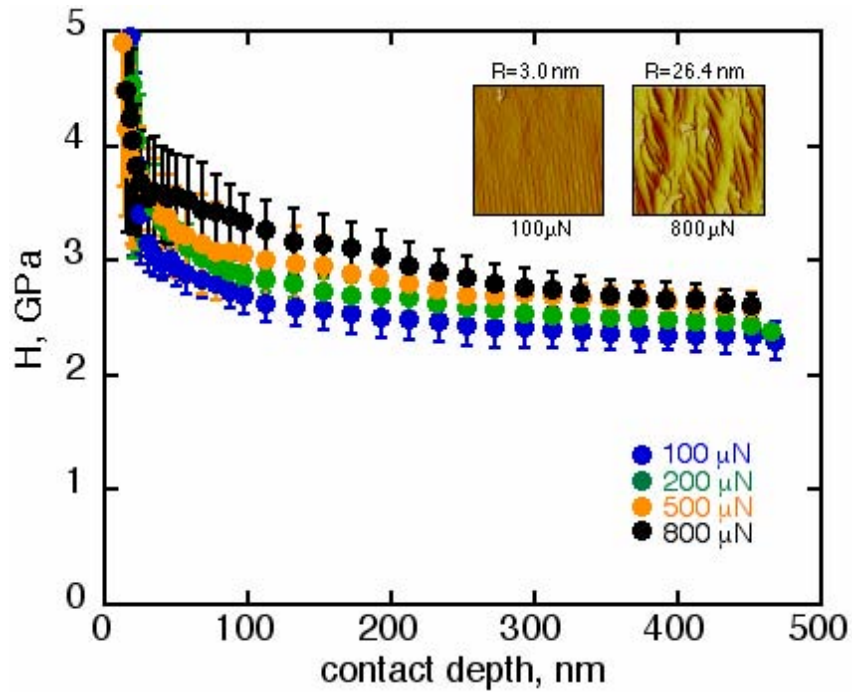
(b)

Figure 7.5. Increasing applied load led to an increase in extent of surface deformation and hardness after (a) 1 wear pass and after (b) 10 wear passes.
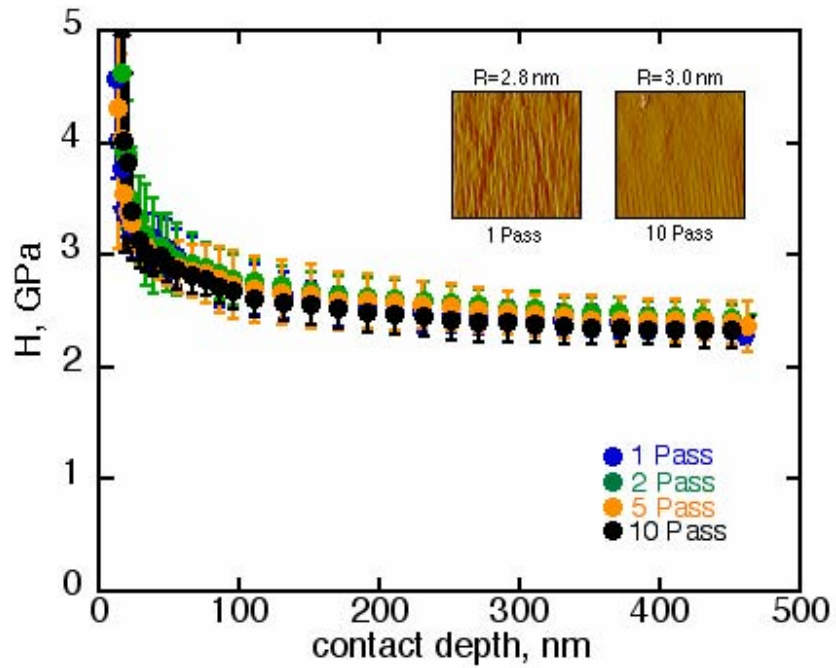
(a)
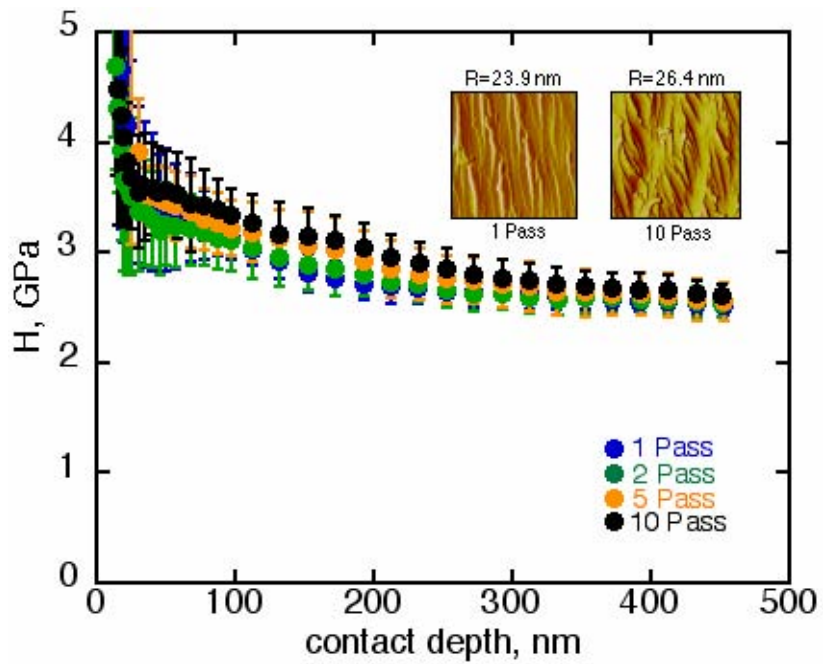
(b)

Figure 7.6. An increase in the number of wear passes also led to an increase in extent of surface deformation and hardness at (a) 100 μN and at (b) 10 μN.
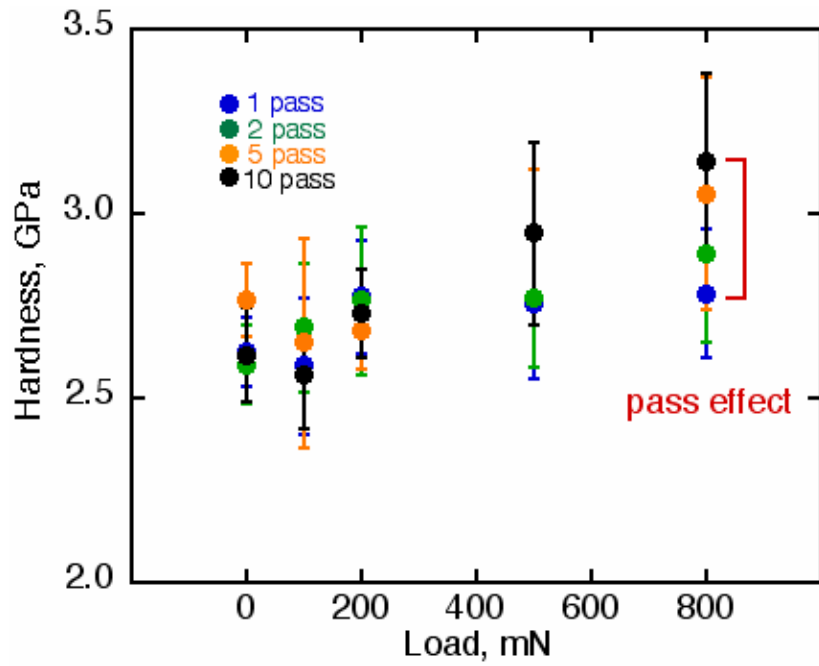
(a)
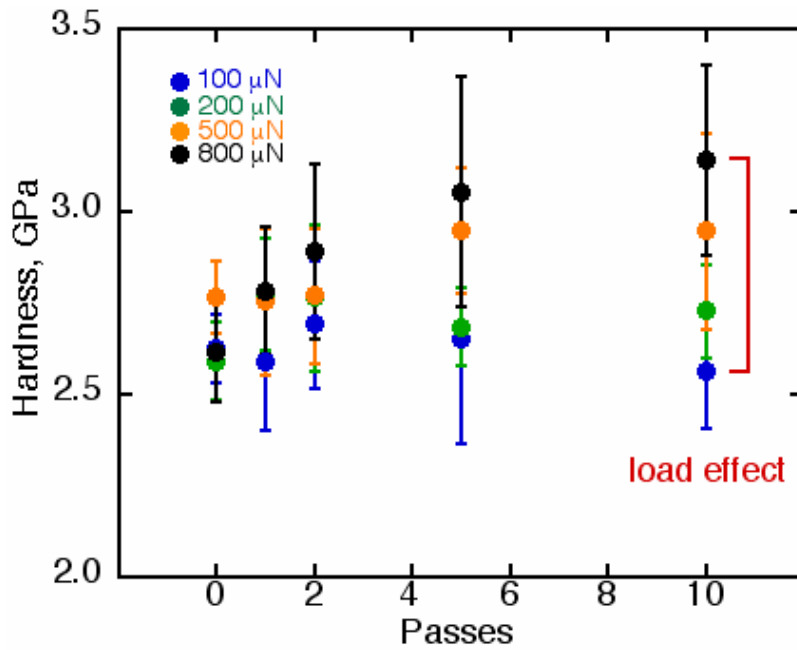
(b)

Figure 7.7. Cross plots of hardness at a depth of 150 nm under (a) an increasing applied load and (b) an increasing number of wear passes shows that applied load has a stronger effect on hardness than an increase in the number of wear passes.
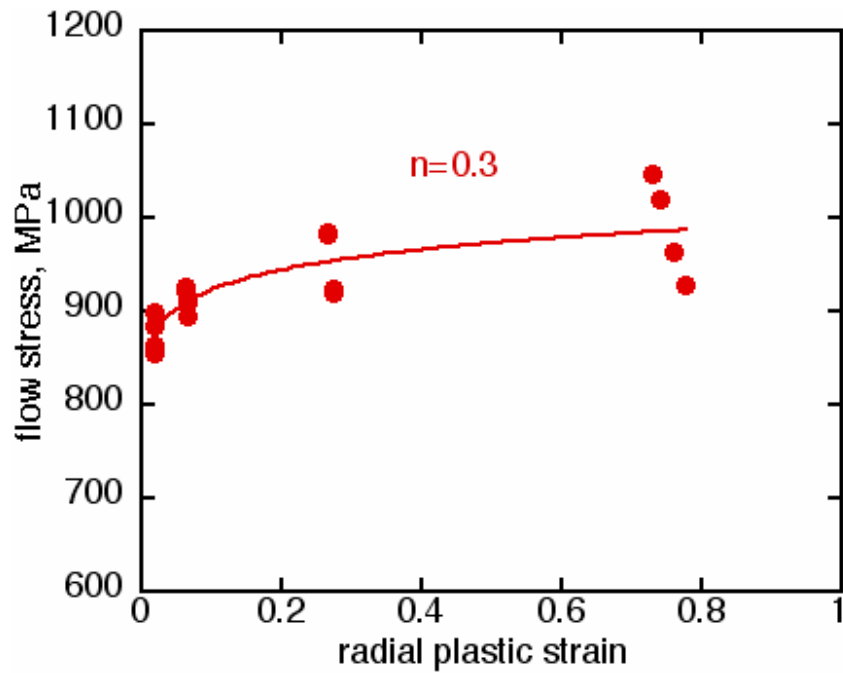
Figure 7.8. The wear pattern data for all test conditions reveal a relatively rate of work hardening for the electrodeposited nickel used in this study.
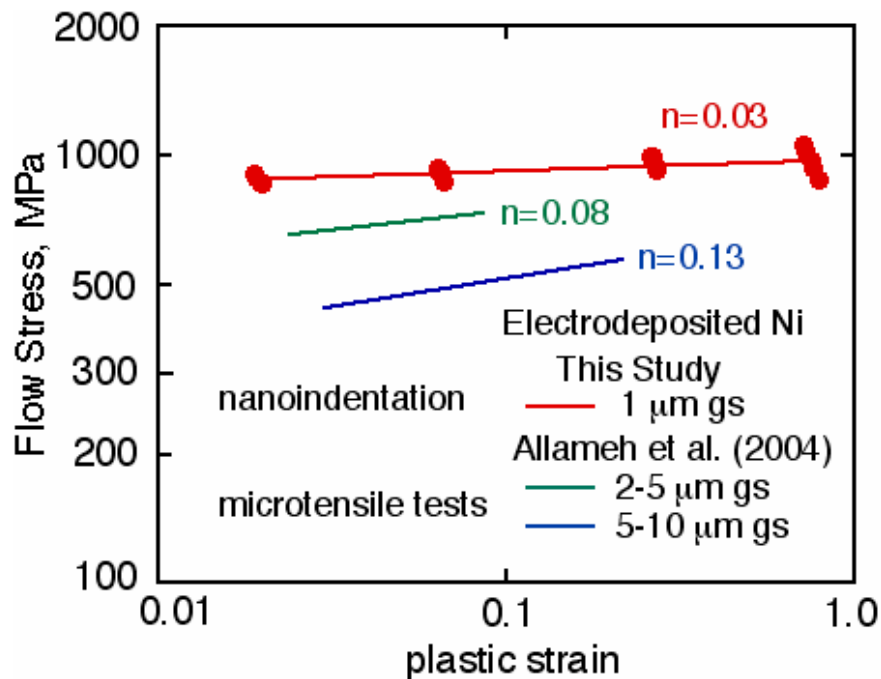
Figure 7.9. The work hardening coefficient determined from indentation response within the wear patterns follows the evolution of work hardening response with increasing yield strength and decreasing columnar width established from tensile tests on high strength electrodeposited nickel samples. [7.12] The size scales refer to column widths.

8. The Role of Subsurface Deformation on the Tribological Behavior of Coatings

8.1. Introduction

Tribological contacts between metallic materials often induce plastic deformation [8.1], may transfer material from one surface to another, and can result in the formation of metallic junctions and stick-slip behavior [8.2-8.4]. Additionally, most metals in their as-fabricated state exhibit frictional coefficients from 0.6 to 1.2. Therefore, tribological coatings are often required to increase the lifetime of an engineered surface. In addition to the intrinsic tribological behavior of a coating, substrate deformation (elastic, plastic or elasto-plastic) plays a crucial role in governing the friction response of the coated system. Consequently, an understanding of the stress state within both the tribobogical coating and the underlying metallic substrate is required to estimate the tribological reliability of a coated system. The purpose of this present study is to utilize simple finite element simulations as a method to determine the load (and corresponding stress state) at which the transition from elastic to plastic deformation occurs in either the tribological coating or the metallic substrate, and relate this transition to large changes in the coefficient of friction obtained on a standard ball-on-disc tribometer.

The reliability of tribological hard coatings is directly linked to the contact stresses experienced in both the film and substrate during mechanical contact. For many contact couples employing tribological coatings, the stresses are essentially elastic and the friction and wear behaviors are relatively well understood. Conversely, for conditions where either the film or the substrate to plastically deform, the friction and wear behavior can vary significantly from the elastic case. Additionally, when a surface is subjected to both a normal and sliding contact, the local stresses may generate acute strain gradients which can result in unintended modification of the topography, microstructure and mechanical properties of the device surface [8.5]. These combined normal and tangential contact stresses can also lead to debris generation in the contacting materials, often resulting in premature failure of the component. Consequently, one of the critical issues in the design of engineering systems with sliding surfaces involves understanding the stresses that are generated between and within the materials in contact.

During sliding, contact stresses are transmitted into the coating and substrate. If the frictional coefficients are high enough, significant stresses can build up and lead to an accumulation of plastic deformation in either the coating or the substrate. When these plastic strains exceed a threshold, hard tribological coatings can fracture, generating debris and potentially exposing the underlying material. Since the overall tribological performance is directly linked with both the mechanical properties of the materials in the system and the geometry of the contact, the development and tribological validation of new coatings and contact geometries has generally been subjected to an experimental "trial-and-error" approach. While this limited approach has been successful, modifications to the applied coatings or contact surfaces can alter performance and require additional testing for tribological validation. Consequently, considerable effort has been applied in the simulation and finite element analysis (FEA) of tribological contacts to more

fully understand the deformations processes occurring underneath static and sliding contacts [8.6 - 8.14]. Although much of the early work restricted the problem by considering only elastic or plastic deformation and generally limited the calculations to two-dimensional approximations, even these relatively simplistic computational simulations have allowed for significant insight into the deformation mechanisms in a tribological contact couple.

For the specific case of stress generation during sliding contacts, both two-dimension [8.8, 8.10, 8.13-8.14] and three-dimension [8.9, 8.11] computational studies have been performed with great success. These studies have shown the unique flexibility of FEA in the design of tribological systems by presenting insight into how changes in material properties and interfaces under various mechanical loading situations alter the tribological response. Obviously, most simulations require significant simplification with respect to real materials in order to numerically run within realistic timeframes. These simplifications often include: surface roughness effects (simulated surfaces are often ideally smooth), dimensionality (2D simplifications), and homogeneity (most materials have contaminants, 2nd phases, voids or other defects that arise during processing). Nevertheless, scaling arguments can often be made to account for most of the assumptions made.

One family of materials that has shown the required combination of mechanical and tribological properties for use as protective layers is diamond-like carbon (DLC). While different DLC films can vary greatly in specific composition, the films tend to be amorphous with mixed phases consisting of sp^2 (trigonal) and sp^3 (tetrahedral) bonding. DLC films can be deposited using numerous methods including DC and RF sputtering, ion beam deposition, laser ablation, and plasma-enhanced chemical vapor deposition (PECVD) [8.15]. Since the tribological properties of a given DLC film are directly linked to the structure of the film, the friction coefficients and wear rates generally depend upon the specific environment at the contact (contact pressure, environment, temperature, and sliding velocity). For example, hydrogenated DLC films show excellent tribological behaviors in dry or inert gas environments where frictional coefficients can be less than 0.01; however, with increasing humidity the coefficient of friction can increase toward 0.6 [8.16]. Conversely, hydrogen-free DLC coatings work exceptionally well in humid environments, where coefficients of friction for self-mated surfaces below 0.1 have been observed.

In an effort to generate a film that was tribologically useful in both dry and humid environments, a unique DLC was introduced by Dorfman where friction couples show coefficients around 0.05 in dry conditions and under 0.2 in humid environments [8.15, 8.17- 8.18]. These coatings, termed diamond-like nanocomposites (DLN) are comprised of interpenetrating amorphous diamond-like (a-C:H) and quartz-like (a-Si:O) networks [8.17, 8.19]. As these interpenetrated networks have limited bonding between them, the internal stresses generated during processing are typically small, generally 200-800 MPa compressive [8.18], allowing for good adhesion to a wide variety of substrates.

As model systems concerning the situation of a hard coating on a soft substrate, DLN-coated nickel and DLN-coated nickel-manganese are ideal for examining the contact stress-induced microstructural evolution mechanisms in both a soft (nickel) and somewhat hard (nickel-maganese) metallic substrate. In this type of hard coating on a soft substrate system, the friction-

contact stress relationships can vary greatly and diverge away from the behavior predicted by the Hertzian contact model. In order to determine and characterize the accumulated damage from wear tests, finite element simulations will be used to monitor the critical load for the generation of plastic deformation and the evolution of plastic damage beneath a spherical probe. In parallel, experimental friction tests will be performed with post testing characterization utilizing SEM, EDS and focused ion beam (FIB) techniques coupled with electron backscatter diffraction (EBSD) for microstructural evaluation.

8.2. Methods

8.2.1. Finite Element Simulations

Finite element simulations were performed using ABAQUS/Standard version 6.4 with ABAQUS/CAE employed in post simulation modeling visualization. The simulation setup is defined elsewhere [8.20], but briefly, a mesh was generated with a Visual Basic macro using the specific material geometries (with respect to the film thickness and counterface geometry defined below) as inputs. The different materials were modeled as isotropic, elastic-plastic solids, where the plastic boundary was defined using a Mises yield criterion. As the accuracy of FEM simulations depends heavily on the accuracy of the input material properties, the elastic and plastic responses of the DLN coating and nickel were determined by comparing the simulated indentation behavior to the experimental nanoindentation response. An iterative process of comparing the experimental indentation response with the predicted FEM simulations using differing material properties was performed until the simulated indentation response converged with the experimental data. Once the mechanical behavior of the bare nickel was established, the same process was used to determine the properties of the DLN coating. The simulations were run on either a 600 MHz Octane2 workstation or a 3.8 GHz Pentium 4 desktop and took between 5 and 30 minutes to run, depending on the mesh size and complexity.

8.2.2. Instrumented Indentation

To replicate the contact pressures generated during a friction test, a custom tip holder for a MicroMaterials NanoTest and MicroTest (Micro Materials Limited, Wrexham, United Kingdom) was manufactured to hold the same 3.125 mm diameter Si_3N_4 CERBEC spheres (Saint Gobain Ceramics, East Granby, Connecticut USA) that were used in the friction testing. Load-displacement indentation tests were then performed to peak loads ranging from 100 mN to 1000 mN corresponding to the deadweight loading conditions of the friction tests. Elastic modulus and indentation hardness tests were determined using the continuous stiffness method with a Berkovich diamond indenter tip in a MTS Nanoindenter XP (MTS Nano Instruments, Oak Ridge, Tennessee) on both the bare nickel substrate and the DLN-coated nickel.

Bulk nickel coupons were electroplated from a sulfamate bath using a process described elsewhere [8.21].   Briefly, the nickel was deposited into a square array of 10 mm by 10 mm micromolds defined by a 500 μm photoresist layer on a metallized silicon substrate. After

deposition, a surface lapping procedure was used to planarized the nickel surface. The photoresist was then dissolved and test coupons were diced. The resulting nickel microstructure is characterized by a columnar grain structure with highly twinned grains of approximately 1-2 μm in width [8.22]. The nickel-manganese coupons, deposited into circular-molds with a diameter of 3 mm, resulted in a much finer columnar grain structure with grains approximately 0.2 – 0.5 μm in width [8.23]. These nickel and nickel-manganese coupons were then coated with DLN using a PECVD process where the bare metal substrates were ultrasonically cleaned and loaded onto a rotatable substrate stage in a deposition chamber. DLN coatings were deposited to a thickness of 520 nm on the nickel coupons and 190 nm on the nickel-manganese samples. During the deposition, the substrates were not directly heated, however temperatures as high to 150 °C were possible during film growth due to radiative heating from a filament that generates the plasma [8.19].

8.2.3. Tribological Testing

Friction tests were performed on a custom-built unidirectional linear wear tester housed inside an environmental chamber. A dry nitrogen atmosphere with an oxygen content below 8 PPM and a dew point below -35 °C (relative humidity ~ 1.3%) was maintained during all tests. The same Si_3N_4 spheres used in the instrumented indentation testing were utilized as the counterface during the sliding tests. Si_3N_4 was selected to ensure that all plastic deformation was contained within the DLN film and metallic substrate. The Si_3N_4 ball holder was attached to a transducer to measure the tangential (frictional) loads. Friction tests at normal loads of 98, 245, 490 and 980 mN (corresponding to deadweight masses of 10, 25, 50 and 100 grams) were applied for 1000 cycles with a track length of about 3 mm and sliding speeds of approximately 7.5 mm/sec.

8.2.4. Microscopy

Scanning electron microscopy (SEM) of the wear surfaces was performed using a Zeiss Supra 55VP field emission SEM. A Rontec EDS *in-situ* energy dispersive x-ray spectroscopy detector was used to collect elemental maps of the wear regions. Cross-sections within the wear scars were prepared using an FEI DB 235 system containing both a high resolution scanning electron microscope (SEM) and focused ion beam (FIB). This duel beam configuration allows for sample imaging using the non-destructive electron beam without the damage associated with ion imaging. It was previously shown how a FIB could be used to prepare cross-sections for microstructural analysis at specific mechanical sites on a wear deformed surface [8.23]. Since the FIB combines accurate positioning for sample milling and does not alter the microstructure (the way that more aggressive steps like core drilling or diamond sawing do), sample preparation-induced changes to the wear-deformed microstructure are minimized. Platinum was selectively deposited over the wear surface prior to FIB micromachining to minimize damage to the wear surface from the ion beam. The cross-sections were milled using 30 kV gallium ions. For subsequent electron backscatter diffraction (EBSD) analysis, the cross-section samples were removed using a micromanipulator and were placed on a carbon coated transmission electron microscope support grid. The EBSD analysis was performed in the FEI DB 235 system using HKL Technology Channel 5 orientation mapping hardware and software. The samples were

tilted to 62° with respect to the electron beam during imaging. Orientation maps were generated by positioning cross-section beneath the electron beam and collecting an EBSD pattern pixel-by-pixel across an area using a pixel step size of 0.05 μm. Each EBSD pattern was automatically indexed and the crystallographic orientation was then determined [Humphreys (2001)]. One additional advantage of the FIB is the ability to obtain channeling contrast images from crystalline materials. The channeling of ions is a function of the lattice orientation. This effect can be used to obtain images which reflect the grain structure of the sample. Ion channeling images are produced by collected the secondary electron signal generated by the 30 kV Ga^+ ion beam as it rastered over the sample. The channeling of the Ga ions results in changes to the secondary electron yield resulting in images which highlight changes or differences in grain orientations.

8.3. Results

8.3.1. Instrumented indentation for FEM validation

In order to evaluate the stresses that are generated under the sliding Si_3N_4 ball, a series of instrumented indentation experiments were performed. Results from the indentation tests into the DLN-coated nickel using a 3.125 mm Si_3N_4 ball and both the Nanotest and Microtest are shown in Figure 8.1. This load-displacement data results from five separate indentation tests which have been binned every 10 nm where the error bars are contained within the markers. Since the Nanotest load cell is limited to peak forces of 450 mN, the Microtest transducer was employed for indents with loads above 250 mN, allowing for an overlap between the transducer experimental data.
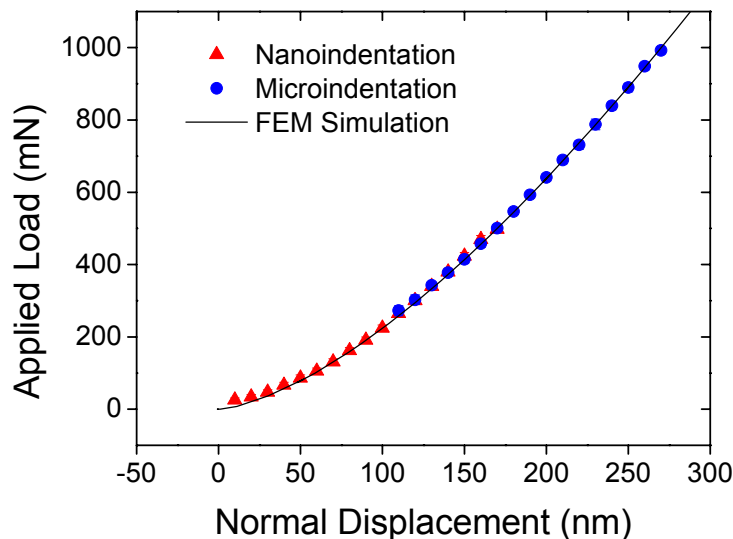
Figure 8.1. Experimental indentation data with finite element simulation overlayed on the data.

8.3.2. Finite Element Predictions

From the iterative process of comparing the FEM simulations with the experimental indentation results, the properties of the nickel substrate and DLN coating were determined (Table 8.1), where the nickel-manganese values were taken from previously published values [8.24]. The values for the DLN film are in good agreement with previous published data [8.15, 8.18]. Since the yield stress in the nickel and nickel-manganese are so much lower than that of the hard DLN coating, it is expected that the generation of permanent strain will be accommodated primarily by dislocation plasticity in the nickel substrate rather than plastic flow in the amorphous DLN coating The predicted load-displacement response for a 3.125 mm Si_3N_4 ball indenting the DLN-coated nickel is overlaid on the experimental indentation data showing the fit between the predicted load-displacement response and the experimental behavior (Fig. 8.1.).

Table 8.1. Mechanical properties of substrate materials.

	Elastic Modulus (GPa)	Yield Stress (MPa)	Hardness (GPa)
Nickel	195 ± 3.2	540 ± 23.4	1.3 ± 0.2
Nickel-Manganese	190	860	-
DLN	98.2 ± 3.3	7180 ± 20.3	13.3 ± 0.5

Using the FEM simulation on the DLN-Ni shown in Fig. 8.1, snapshots of accumulated plastic strain at loads corresponding to the previous friction tests are shown in Figure 8.2. An applied load of 98 mN (Fig 8.2a) generates no plastic strain in either the DLN coating or the nickel substrate. The onset of plasticity in the nickel substrate occurs at a load of 280 mN (not shown). When the load is increased to 490 mN a well-defined volume of plastic deformation beneath the tip in the nickel is formed (Fig. 8.2b). This plastic volume both expands and increases in intensity when the load is increased to 980 mN (Fig. 8.2c). Similarly, snapshots of the DLN-NiMn simulations are shown in Fig. 8.3. Again, there is no evidence of plastic deformation in either the DLN coating or the NiMn substrate at 98 mN (not shown) or 245 mN (Fig 8.3a). Coincidentally, the onset of plastic deformation occurs around a load of 490 mN (Fig 8.3b). As expected, the plastic zone expands when the load is increased to 980 mN (Fig 8.3c).
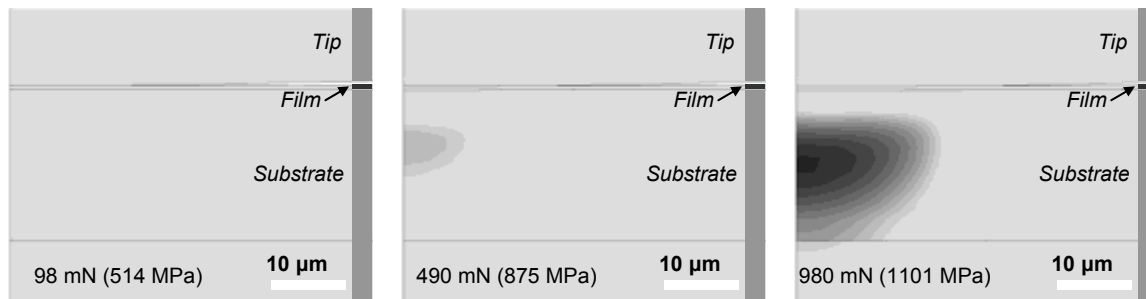
Figure 8.2. FEM simulations of the generation of plastic strain under 1/8" Si_3N_4 ball on DLN-coated Ni.
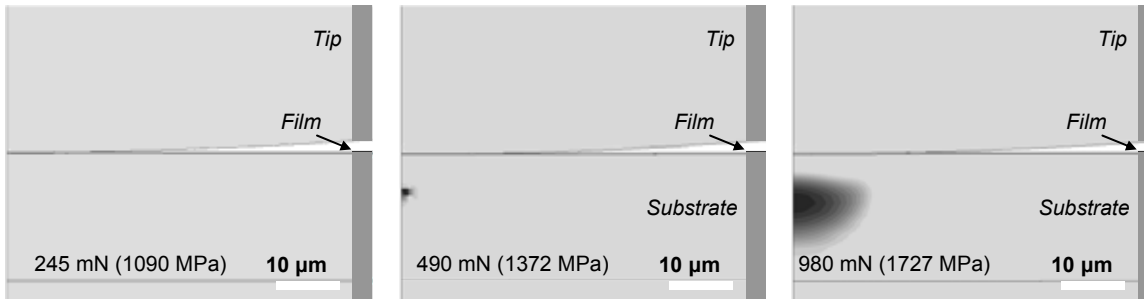
Figure 8.3. FEM simulations of accumulated plastic strain on DLN-coated NiMn under 1/16"
Si$_3$N$_4$ ball. Note the increased contact stress as compared to the contact stress in Figure 8.2
(which used a 1/8" Si$_3$N$_4$ sphere).

8.3.3. Friction Tests

The typical friction response of the uncoated and DLN-coated nickel and DLN-coated nickel-
manganese are shown in Figure 8.4. As shown in Fig. 8.4a, the friction tests using a 3.125 mm
diameter Si$_3$N$_4$ sphere on both the uncoated nickel and the DLN-coated nickel show that the
frictional coefficient varies significantly as a function of the applied load. At a normal load of 98
mN, corresponding to a contact stress of 514 MPa, the addition of the DLN coating clearly
reduces the steady-state frictional coefficient from the bare nickel value of 0.451 ± 0.022 down
to 0.061 ± 0.002. Increasing the load to 490 mN (875 MPa) results in a slightly higher friction
coefficient of 0.094 ± 0.014. The friction trace is also somewhat more diffuse, possibly implying
a breakdown of the film or stick-slip response during the sliding. At an applied load of 980 mN
(1101 MPa), the friction coefficient at the end of the test is approximately 0.283 ± 0.020 and is
trending toward the value of the bare nickel. In Fig 8.4b, the response of the DLN-coating on the
harder NiMn substrate is shown for smaller 1.563 mm diameter Si$_3$N$_4$ spheres. When the normal
load is increased from 98 mN (804 MPa) to 245 mN (1090 MPa), the frictional coefficient
decrease from 0.097 ± 0.009 to 0.041 ± 0.013. Nevertheless, with subsequent load increases of
490 mN (1372 MPa) and 980 mN (1727 MPa), the coefficients of frictional deviate from the
Hertzian model and increase to 0.199 ± 0.010 and 0.364 ± 0.020 respectively.
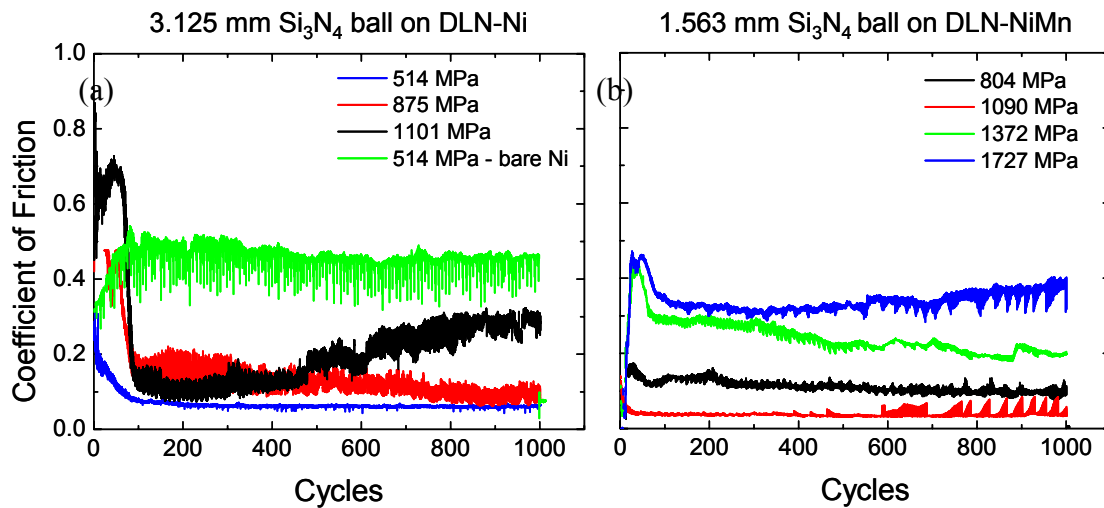
Figure 8.4. Friction data on the DLN-coated Ni and NiMn samples.

8.3.4. SEM and EBSD

SEM micrographs of wear surfaces on the bare nickel show significant damage even at 98 mN (Fig 8.5a); however, the DLN-coated nickel shows minimal damage with only minute wear debris present outside of the wear track (Fig. 8.5b). The micrograph of the wear surface formed from the 490 mN normal load (Fig. 8.6a) shows a more heavily damaged DLN coating, with noticeable grooving in the coating and the generation of large particles. The EDS elemental map shows distinct nickel-rich and silicon-rich regions within and around the wear scar (Fig. 8.6b). In these maps, blue corresponds to nickel (the substrate) and the red corresponds to silicon (the DLN coating). The nickel-rich regions are likely comprised of either exposed Ni or greatly thinned DLN coating.

After 1000 wear cycles at 980 mN (Fig. 8.6c), the coating is severely worn and large areas of the DLN coating have failed, exposing continuous strips of the nickel (Fig. 8.6d).

Typical ion induced secondary electron images from FIB cross sections are shown in Fig. 8.7 for the DLN-coated nickel. The two featureless layers at the top of the figures correspond to the amorphous DLN coating and to platinum that was deposited to protect the DLN and nickel from damage during the ion milling procedure. In these images, the samples are tilted 45° to the detector, resulting in an under emphasis of the microstructure in the vertical direction. At the lowest load of 98 mN (514 MPa), the DLN coating is essentially undamaged and there is no evidence of plastic deformation in the substrate (Fig. 8.7a). When the load is increased to 490 mN (contact stress of approximately 866 MPa), the DLN is essentially undamaged but the nickel grains have been plastically deformed, with significant grain bending in the direction of the sliding Si_3N_4 ball. At a normal load of 980 mN (corresponding to a contact stress of 1090 MPa) the DLN coating is heavily fractured and the nickel substrate has undergone significant plastic deformation (Fig. 8.7c). This behavior is even more evident when these cross-sections are imaged using the EBSD automated orientation (Fig. 8.8). In these images, the generation of plastic deformation at higher applied loads leads to a significant degree of grain rotation and recrystallization in the high-shear regions near the surface.

The microstructural response of the DLN-coated NiMn to the sliding probe is similar to that of the DLN-Ni system; however, since the NiMn substrate has a higher yield stress the damage threshold is shifted to higher contact stresses. Nevertheless, the microstructural evolution observed from the cross-sections within the wear scars on the DLN-NiMn sample show that at the lowest contact stress of 1090 MPa (Fig 8.9a) the coating is intact and uniform across the surface. As the contact stress increases to 1372 MPa (Fig 8.9b), the thin coating breaks down into finely divided segments, which are incorporated into the exposed Ni-Mn surface, resulting in a surface of both DLN particles and exposed NiMn. At the highest contact stress of 1727 MPa, the DLN coating has been completely removed, and the subsurface deformation has clearly formed into two distinct zones, characterized by a zone of equiaxed nanocrystalline grains at the surface, with a zone of columnar grain bending below (Fig 8.9c).
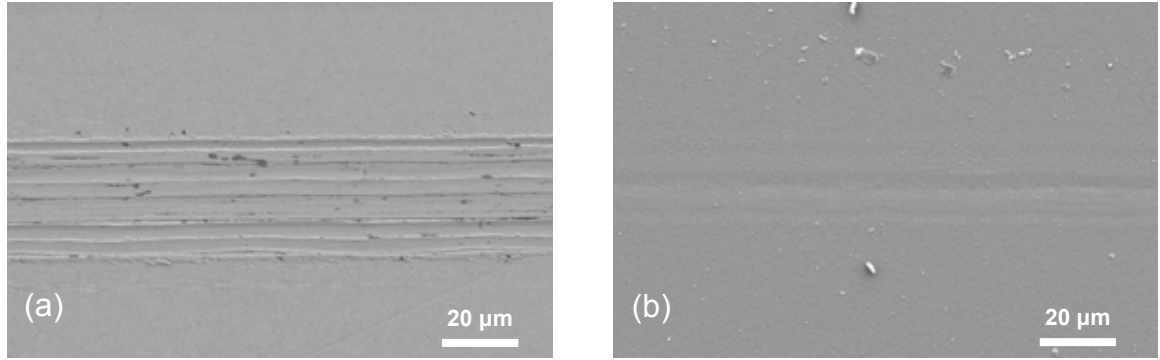
Figure 8.5. SEM of wear scars at 98 mN (514 MPa) on (a) bare nickel and (b) DLN-coated nickel.
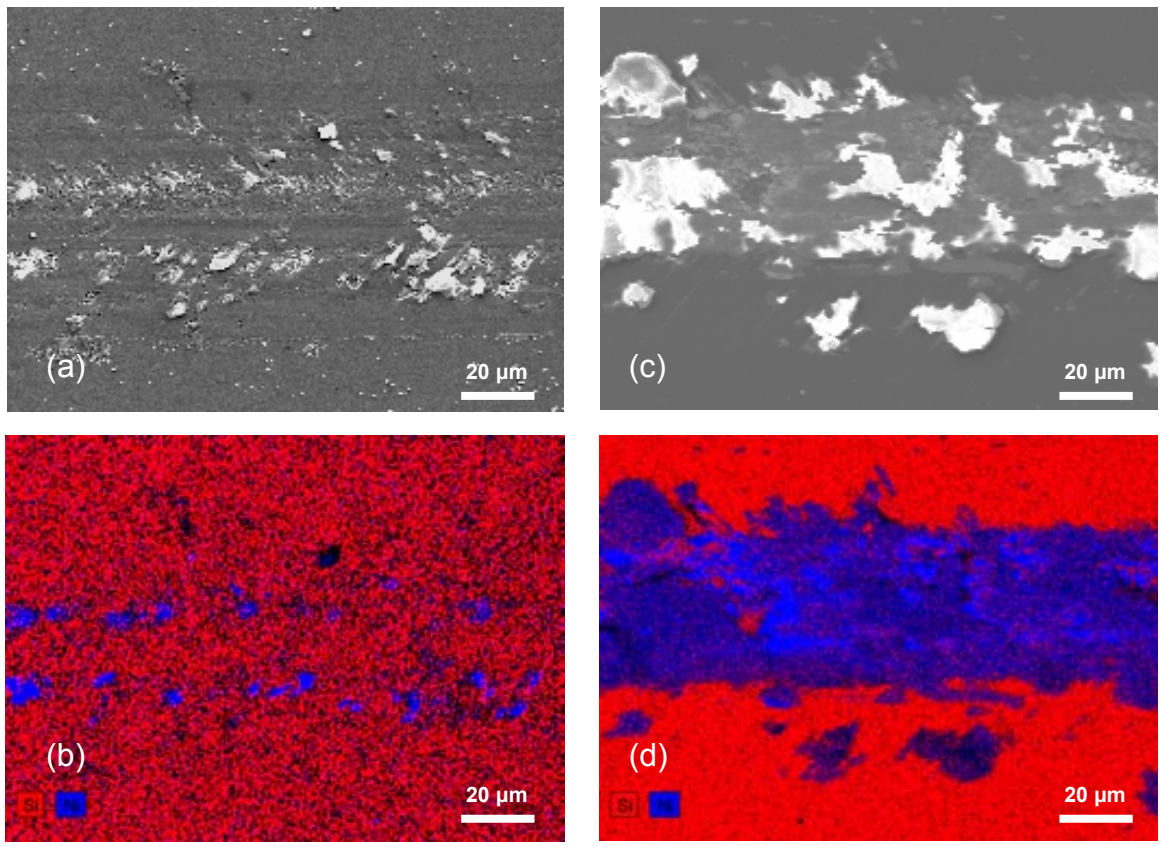
Figure 8.6. Secondary electron image and energy dispersive spectroscopy (EDS) elemental maps of wear scars on DLN-coated nickel showing (a,b) initial generation of wear debris at 490 mN and (c,d) breakdown and failure of the DLN coating at 980 mN.

98 mN (514 MPa)   490 mN (875 MPa)   980 mN (1101 MPa)

(a)   (b)   (c)
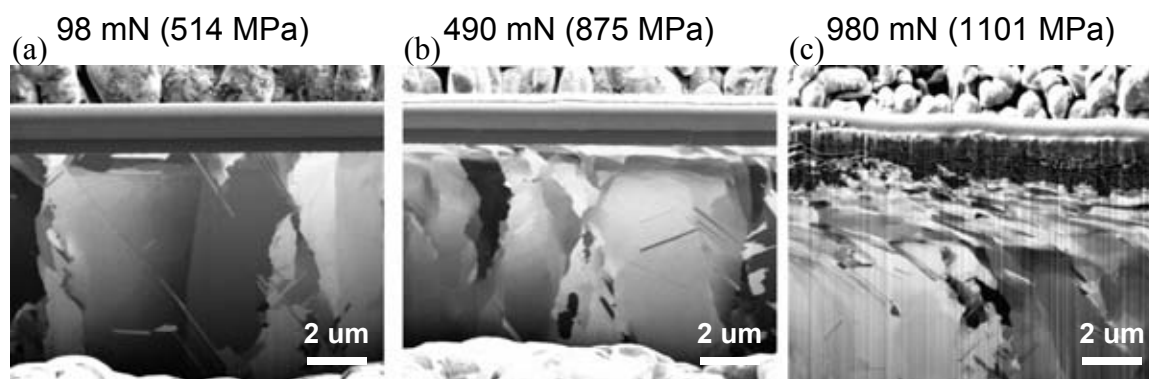
Figure 8.7. Ion-induced secondary electron images of DLN-Ni friction test cross-sections.

98 mN (514 MPa)   490 mN (875 MPa)   980 mN (1101 MPa)

(a)   (b)   (c)
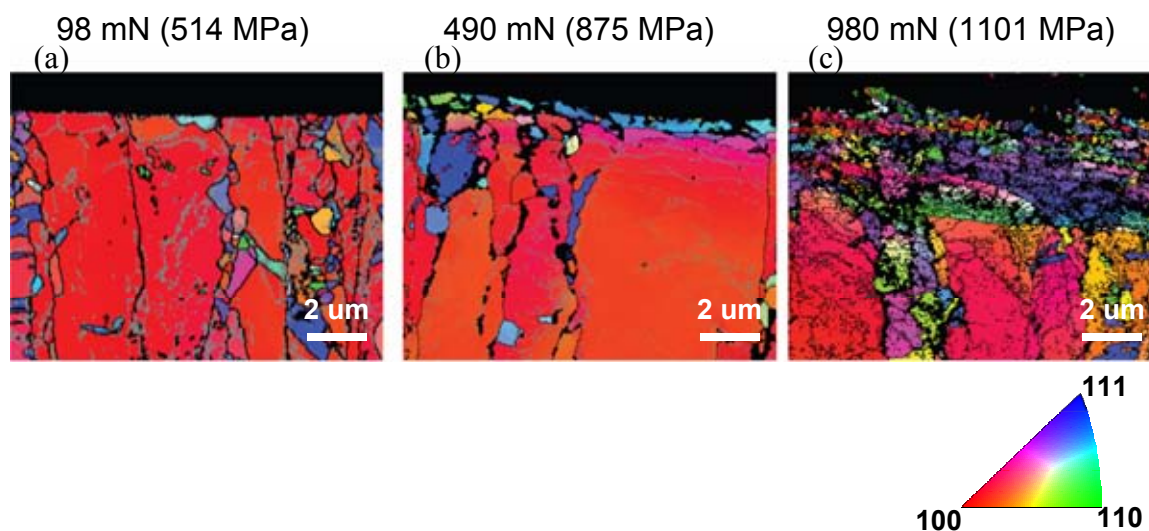
Figure 8.8. EBSD results from DLN-Ni friction test cross-sections.

245 mN (1090 MPa)   490 mN (1372 MPa)   980 mN (1727 MPa)

(a)   (b)   (c)

Figure 8.9. Ion-induced secondary electron images of DLN-NiMn friction test cross-sections

8.4. Discussion

For the case of solid lubricant films where the macroscopic stresses are elastic, non-Amontonian friction behavior has been extensively explored [8.15, 8.25]. In these studies, the coefficient of friction has been shown to be a function of the applied load, L, through the equation,

$$\mu = S_0 \pi \left(\frac{3R}{4E} \right)^{2/3} L^{-1/3} + \alpha, \qquad (8.1)$$

where μ is the coefficient of friction, S_0 is interfacial shear strength, R is the ball radius, E is the composite elastic modulus and α represents the lowest attainable friction coefficient of the friction couple. This equation can be simplified by substituting the load term with the mean Hertzian contact pressure of the contact, P, to the expression,

$$\mu = \frac{S_0}{P} + \alpha. \qquad (8.2)$$

This method has been used to describe the frictional behavior of solid lubricants including MoS_2 and WS_2 where the interfacial shear strengths were reported as 22 and 25 MPa respectively. Previous friction and wear studies on DLN-coatings deposited onto hard silicon substrates have shown that the Hertzian model accurately predicts the coefficient of friction under a similar range of contact stresses [8.15]. Undoubtedly, in this type of hard film - hard substrate system, all contact stresses would be completely elastic (ignoring asperity contacts which almost certainly exceed their plastic-threshold).

For the case in this study of DLN films deposited on softer metallic substrates, the increase in the coefficient of friction with increasing contact stress, which deviates from the predicted Hertzian behavior, is clearly due to the generation of plasticity in the ductile substrate (Fig. 8.10). On both the DLN-Ni and DLN-NiMn samples, at the contact stress where the FEM 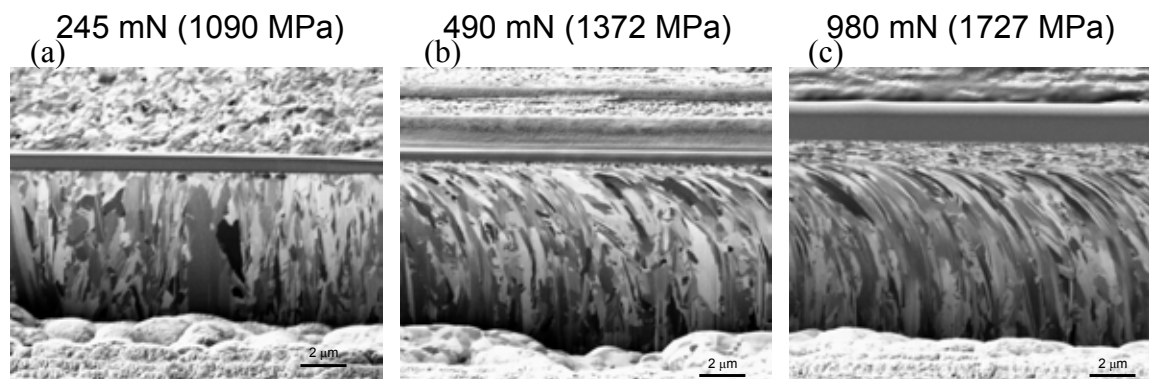simulation indicate only elastic deformation, the measured experimental frictional coefficients were low and the corresponding microscopy showed only minimal wear with a pristine microstructure. Additionally, the increasing elastic contact stress results in a decrease in the measured frictional coefficient in agreement with Equation 8.2; however, in both the DLN-coated Ni and the DLN-coated NiMn, when the finite element simulations predicted that the loading conditions would exceed the elastic-plastic threshold, the experimental coefficients of friction increased and the corresponding wear surfaces showed wear damage and debris.

While the quasi-static FEM simulations presented here are not entirely representative of a sliding contact, the pronounced similarities between the plastic deformation predicted in the quasi-static simulations and the observed microstructural changes in the experimental samples, indicate that these simple simulations can adequately predict when friction regime changes may occur. This provides a powerful tool in the selection of appropriate material combinations for specific contact stress environments. Additionally, prior to generation of plasticity in the substrate, the low frictional coefficients of the DLN coating in the elastic regime ($\mu < 0.1$) will not either dramatically increase or shift the stress distribution beneath the contact [8.13]. Consequently, the quasi-static simulations could be viewed as a best-case condition, where the generation of plasticity in the simulation would almost certainly guarantee failure of the system during sliding.
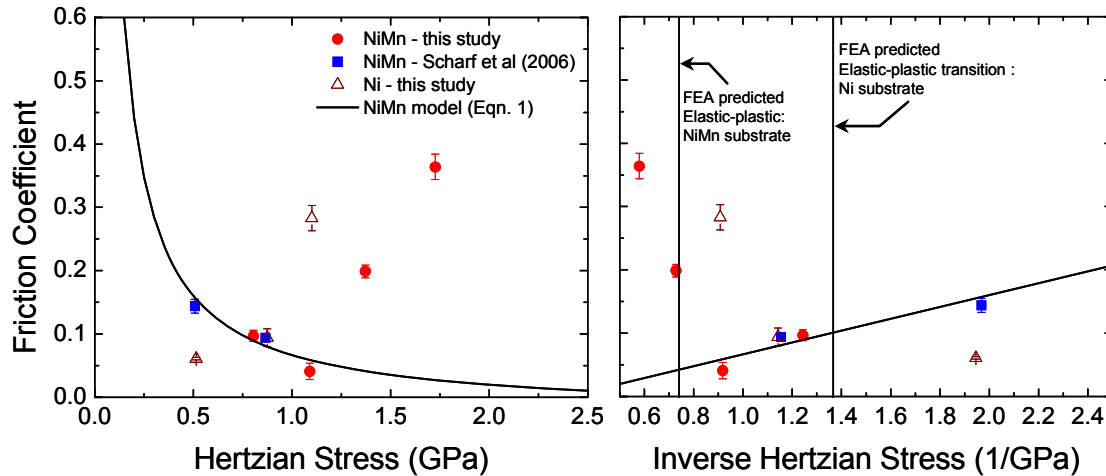
Figure 8.10. Fit of Hertzian contact friction model with experimental friction data.

An additional simplification between the simulations and the experimental conditions arise from the real surface roughness of the samples. The simulations assume that the surfaces are completely smooth; however, the DLN-coated samples have an RMS roughness of ~ 24 nm and the Si_3N_4 balls have a RMS roughness of ~ 10 nm. The practical consequence of this roughness is that at very low loads, where the real area of contact and Hertzian contact area are very different, the simulation results will not accurately predict the stresses beneath the probe. However, for the geometries used in these experiments the tip displacement at the lowest load of 98 mN is approximately 59 nm, almost a factor of three greater. Additionally, the surface asperities on the DLN coating are almost certainly above the flow stress due to the very high local contact pressures. Consequently, the combined roughness of the film and Si_3N_4 sphere are dominated by the overall geometry of the contact and can be well represented by the ideal-case simulations. Additionally, since plastic generation in the DLN-Ni system is not generated until a load of 280 mN, corresponding to a displacement of ~120 nm, real contact area most likely approaches that of geometric (or apparent) contact area.

The wear-induced nickel and nickel-manganese microstructures are seen in the cross-section images of Fig. 8.7 and Fig. 8.9. The smaller grains of the nickel-manganese result in increased observed strength due to a Hall-Petch hardening mechanism. Nevertheless, both the nickel and nickel-manganese microstructures show similar deformation evolutions, albeit at different contact stress levels. At the lowest (elastic) contact pressure, the grains are almost perfectly columnar and accommodate the sliding probe elastically. As the contact stress exceeds the flow stress of the substrate, the substrate accommodates the stress by grain bending in the direction of the sliding ball. Eventually, this mechanism cannot accommodate additional deformation and a zone of equiaxed nanocrystalline grains is formed. This equiaxed zone allows for subsequent deformation via in-plane "rolling" of these grains beneath the sliding probe.

It is reasonable to assume that the plastic deformation produces significant strains at the coating-substrate interface, producing large concentrated stresses that drive local fracture in the DLN coating. Once a flaw is introduced, the tensile stress field that trails behind the sliding Si_3N_4 sphere can extend the crack towards the surface. With this process occurring throughout the entirety of the wear track, and the repeating every cycle, individual cracks can coalesce, resulting

in the generation of free particles and subsequent removal of the coating. When enough of the coating had been removed, direct contact with the metallic substrate could be achieved, allowing for adhesive processes between the sliding tip and metallic substrate.

As observed from the changes in the coefficient of friction with increasing stress, the generation of plastic deformation in the substrate introduces a significant variation away from the well-described Hertzian contact prediction. While this is not surprising, the mechanism for the increase in friction is the breakdown and fracture of the DLN coating. Evidence for this proposed mechanism can be seen in the SEM images and EDS maps. At the highest load the SEM micrographs show a severely worn wear scar and the corresponding EDS map indicates distinct regions of nickel, implying that the nickel substrate is exposed to the surface. Since subsequent sliding across regions of this exposed nickel could result in transfer of nickel to the tip through an adhesive mechanism, an increase in the frictional coefficient towards the value of the bare nickel would be expected.

The FIB-milled cross sections allow for direct imaging of the DLN coating, the grain structure, and the induced deformation beneath the wear track. In these figures, the escalating contact stress is clearly related to increasing plastic strain at the interface between the DLN coating and the metallic substrate. Where the simulations predict only elastic contact to occur, the grain structure is essentially pristine. As the contact stresses increase, plastic deformation in the form of grain bending accumulates at the coating-substrate interface. Eventually, the coating deteriorates under the accumulated strain as shown in Fig 8.8c, where the contact stress of 1101 MPa shows significant cracking in the DLN coating and the corresponding friction data indicates that the coefficient is approaching the value of an uncoated sample. The size of the plastic zone from the FEM simulations matches well with the plastic zone observed in the ion channeling images. Interestingly, around 500 cycles there is a shift in the sliding response from a relatively smooth behavior to a more serrated response, possibly indicating an accumulation of damage in the film or substrate resulting in coating fracture and breakdown.

8.5. Summary and Conclusions

Finite element simulations have been used to elucidate contact stress-induced plasticity resulting in the deviation of the coefficient of friction away from Hertzian models. It is proposed that at the contact stresses where plastic deformation is induced, accumulated plastic strain at the coating-substrate interface can lead to film breakdown which results in a dramatic increase in the frictional coefficient. For conditions mirroring actual tribological tests on a coated material, the load (and subsequent contact stress) at which the elastic-plastic threshold occurred was approximated using simple finite element simulations. Comparing these results with cross-sections of wear scars on both DLN-coated soft nickel and hard nickel-manganese substrates showed that above the FEM predicted elastic-plastic limit, accumulated plastic deformation in the metallic substrate at the coating-substrate interface lead to fracture and subsequent coating removal, exposing the underlying substrate. With the removal of the tribological coating, an increase in the coefficient of friction was noted. The agreement between the FEM simulations and the experimentally observed plastic accumulation suggest that these simple simulations can serve as an approach to quickly determine the reliability of hard tribological coating on plastically deformable substrates.

9. References

1.1. Rigney, D.A., and Hirth, J. P. *Wear* 53 (1979) 345.

1.2. Prasad, S.V., Michael, J.R., and Christenson, T.R. , *Scripta Mater.* **48** (2003) 255-260

2.1. S.V. Prasad, J.R. Michael and T.R. Christenson, *Scripta Mater.* **48** (2003) 255-260.

2.2. T.L. Matteson, S.W. Schwartz, E.C. Houge, B.W. Kempshall and L.A. Giannuzzi, *J. Electronic Mater.* **31** (2002) 33-39.

3.1. Z N. Farhat, *Wear* **250** (2001) 401-408.

3.2. D.R. Wheeler, and D.H. Buckley, *Wear* **33** (1975) 10.

3.3. J.P. Hirth and D.A. Rigney, in Dislocations in Solids, F.R. Nabarro ed. (North Holland, 1983) p. 10.

3.4. A.T. Gwathmey, H. Leidheiser, G.P. Smith, *Proc. Roy. Soc. London* **A312** (1952) 464.

3.5. K.L. Johnson, Contact Mechanics, (Cambridge University Press, 1985).

5.1. R.J. Asaro and J.R. Rice, "Strain Localization in Ductile Single Crystals," *J. Mech. Phys. Solids* **25** (1977) 309.

5.2. D.A. Hills, D. Nowell, and A. Sackfield, Mechanics of Elastic Contacts (Oxford 1993) pp 76-7.

5.3. http://en.wikipedia.org/wiki/Tensor_product

5.4. A. Godfrey and D.A. Hughes, "Scaling of the Spacing of Deformation Induced Dislocation Boundaries," *Acta Mater.* **48** (2000) 1897.

5.5. R. Raj and M.F. Ashby, "Grain Boundary Sliding and Diffusion Creep," *Met. Trans.* **2** (1971) 1113.

6.1. Glaeser WA, Friction and wear, *IEEE Transactions on Parts, Hybrids, and Packaging*, **PHP-7**, (1971) 99.

6.2. Rigney DA, *Wear*, **245** (2000) 1.

6.3. Heilmann P, Clark WAT, Rigney DA, *Acta Metallurgica,* **31** (1983) 1293.

6.4. Rigney DA, Fu XY, Hammerberg JE, Holian BL, Falk ML, *Scripta Materialia*, **49** (2003) 977.

6.5. Heilmann P, Don J, Sun TC, Rigney DA, Glaeser WA, *Wear*, **91** (1983) 171.

6.6. Lepper K, James M, Chashechkina J, Rigney DA, *Wear*, **203** (1997) 46.

6.7. Prasad SV, Michael JK, Christenson TR, *Scripta Materialia*, **48** (2003) 255.

6.8. Heilman P, Don J, Sun TC, Rigney DA, Glaeser WA, *Wear*, **91** (1983) 171.

6.9. Rigney DA, *Materials Research Innovations*, **1** (1998) 231.

6.10. Rigney DA, *Wear*, **175** (1994) 63.

6.11. Dufrane KF, Glaeser WA, *Wear*, **37** (1976) 21.

6.12. Glaeser WA, *Wear*, **123** (1988) 155.

6.13. Tabor D, The Hardness of Metals. New York, Oxford University Press, 1951.

6.14. Oliver WC, Pharr GM, *Journal of Materials Research*, **7** (1992) 1564.

6.15. Bobji MS, Biswas SK, *Journal of Materials Research*, **14** (1999) 2259.

6.16. Joslin DL, Oliver WC, *Journal of Materials Research*, **5** (1990) 123.

6.17. Page TF, Pharr GM, Hay JC, Oliver WC, Lucas BN, Herbert E, Riester L, in Fundamentals of Nanoindentation and Nanotribology, Moody NR, Gerberich WW, Baker SP, Burnham N, eds., *Mater. Res. Soc. Symp. Proc.*, **522** (1998) 53.

6.18. Hokkirigawa K, Kato K, *Tribology International*, **21** (1988) 51.

6.19. Harvey S, Huang H, Venkataraman S, Gerberich WW, *Journal of Materials Research*, **8** (1993) 1291.

6.20. Allameh SM, Lou J, Kavishe F, Buchheit T, Soboyejo WO, *Materials Science Engineering A*, **371** (2004) 256.

7.1. Prasad SV, Michael JR, Christenson TR, *Scripta Materialia*, **48** (2003) 255-260.

7.2. Rigney DA, Hirth JP, *Wear*, **53** (1979) 345-370.

7.3. Hruby J, *MRS Bull*, **26** (2001) 337.

7.4. Buchheit TE, LaVan DA, Michael JR, Christenson TR, Leith SD, *Metallurgical and Materials Transactions A*, **33A** (2002) 539-554.

7.5. Safranek WH, The Properties of Electrodeposited Metals and Alloys, A Handbook, 2nd ed., American Electroplaters Society, Orlando, FL, 1986.

7.6. Dini JW, Electrodeposition, The Materials Science of Coatings and Substrates, Noyes Publications, Park Ridge, NJ, 1993.

7.7. Buchheit TE, Christenson TR, Schmale DT, LaVan DA, Materials Science of Microelectromechanical Systems, *Mater. Res. Soc. Symp. Proc.* **546** (1998) 121-26.

7.8. Landa V, Vitek, Neumann J, *Plating Surface Finishing*, **68**, (1987) 128-33.

7.9. Leith SD, Schwartz DT, *J. Microelectromech. Sys*., **8** (1999) 384-392.

7.10. Xie ZL, Pan D, Last H, Hemker KJ, in Materials Science of Microelectromechanical Systems (MEMS) Devices II, M.P. deBoer, A.H. Heuer, S.J. Jacobs, E. Peeters, eds., *Mater. Res. Soc. Symp. Proc.* **605** (2000) 197-202.

7.11. Cho HS, Babcock WG, Last H, Hemker KJ, in Materials Science of Microelectromechanical Systems (MEMS) Devices III, deBoer M, Judy M, Kahn H, Spearing SM, eds., *Mater. Res. Soc. Symp. Proc.* **657** (2001) EE5231–EE5236.

7.12. Allameh SM, Lou J, Kavishe F, Buchheit T, Soboyejo WO , *Materials Science and Engineering,* A, **371** (2004) 256-266.

7.13. Heilman P, Clark WAT, Rigney DA, *Acta metallurgica*, **31** (1983) 1293-1305.

7.14. Bobji MS, Biswas SK, *J. Mater. Res.,* **14** (1999) 2259-2268.

7.15. Glaeser WA, *Wear*, **123** (1988) 155-169.

7.16. Rigney DA, *Mat Res Innovat*., **1** (1998) 231-234.

7.17. Rigney DA, *Wear*, **245** (2000) 1-9.

7.18. Rigney DA, Divakar R, Kuo SM, *Scripta Metallurgica*, **27** (1992) 975-980.

7.19. Rigney DA, Fu XY, Hammerberg JE, Holian BL, Falk ML, *Scripta Materialia*, **49** (2003) 977-983.

7.20. Rigney DA, Naylor MGS, Divakar R, Ives LK, *Materials Science and Engineering*, **81** (1986) 409-425.

7.21. Hughes DA, Hansen N, *Physical Review Letters*, **87** (2001) 135503(4).

7.22. Kuo SM, Rigney DA, *Materials Science and Engineering* A, **157** (1992) 131–143.

7.23. Hughes DA, Hansen N, *Philosophical Magazine*, **83** (2003) 3871–3893.

7.24. Rigney DA, *Wear*, **175** (1994) 63-69.

7.25. Christenson TR, in MEMS Handbook, M. Gad-el-Hak, ed., CRC Press, 2001.

7.26. Oliver WC, Pharr GM, *J. Mater. Res*., **7** (1992) 1564-1583.

7.27. Rigney DA, Chen LH, Naylor MGS, *Wear*, **100** (1984) 195 - 219.

7.28. Lim SC, Ashby MF, Brunton JH, *Acta metallurgica*, **35** (1987) 1343-1348.

7.29. Greenwood JA, Williamson JBP, *Proc. Royal Soc. London*, **A295** (1966) 300-330.

7.31. Page TF, Pharr GM, Hay JC, Oliver WC, Lucas BN, Herbert E, Riester L, in Fundamentals of Nanoindentation and Nanotribology, edited by Moody NR, Gerberich WW, Baker SP, Burnham N, eds., *Mater. Res. Soc. Symp. Proc.* **522** (1998) 53-64.

7.30. Joslin DL, Oliver WC, *J. Mater. Res.*, **5** (1990) 123-126.

7.32. Harvey S, Huang H, Venkataraman S, Gerberich WW, *J. Mater. Res.* **8** (1993) 1291-1299.

7.33. Gerberich WW, Tymiak NI, Kramer DE, Daugela A, Jungk J, Li M, *Phil. Mag.* A, **82** (2002) 3349-3360.

7.34. Cordill MJ, Hallman DM, Moody NR, Adams DP, W.W. Gerberich WW, *Metallurgial and Materials Transactions A*, 2006, in press.

8.1. Prasad, S. V., Michael, J. R. and Christenson, T. R., *Scripta Materialia* **48** (2003) 255-260.

8.2. Bowden , F. P. and Tabor, D., The friction and lubrication of solids, Clarendon Press, Oxford 1986.

8.3. Sarkar, A. D. Friction and Wear, Academic Press, London 1980

8.4. Prasad, S. V. and K. R. Meckleburg, *Lubrication Engeering* **50** (1994) 511.

8.5. Bobji, M. S., and Biswas, S. K., *Journal of Materials Research*, **14**, (1999) 2259.

8.6. Bhattacharya, A.K., Nix, W.D., *International Journal of Solids and Structures*, **27** (1988) 1047-1058.

8.7. Bourciur, R.J., Follstaedt, D.M., Dugger, M.T., Myers, S.M., *Nuclear Instruments & Methods in Physics Research, Section B: Beam Interactions with Materials and Atoms*, **59-60** (1991) 905..

8.8. Djabella, H., Arnell, R., *Thin Solid Films*, **213** (1992) 205-219.

8.9. Holmberg, K., Laukkanen, A., Ronkainen, H., Wallin, K., *Tribology International*, **38** (2005) 1035-1049.

8.10. Komvopoulos, K., *Journal of Tribology Trans ASME*, **111** (1989) 430-439.

8.11. Kral, E. R., Komvopoulos, K., *Journal of Applied Mechanics*, **63** (1996) 365-375.

8.12. Laursen, T.A., Simo, J.C., *Journal of Materials Research*, **7** (1992) 618-626.

8.13. Tian, H., Saka, N., *Wear*, **148** (1991) 261-285

8.14. Zheng L, Ramalingam S., *Journal of Vacuum Science and Technology*, **A13** (1995) 2390–2398.

8.15. Scharf et al (2006)?

8.16. Erdemir, A., Eryilmaz, O., Fenske, G., *Journal of Vacuum Science and Technology, Part A: Vacuum, Surfaces and Films*, **18** (2000) 1987-1992.

8.17. Dorfman, V.F., *Thin Solid Films* **212** (1992) 267-273.

8.18. Kester,D.J., Brodbeck, C.L., Singer, I.L., Kyriakopoulos, A., *Surface and Coatings Technology*, **113** (1999) 268-273.

8.19. Neerinck, D., Persoone, P., Sercu, M., Goel, A., Venkatraman, C., Kester, D., Halter, C., Swab, P., Bray, D., *Thin Solid Films* **317** (1998) 402-404.

8.20. Knapp, J.A., Follstaedt, D.M., J*ournal of Materials Research*, **19** (2004) 338-346.

8.21. Buchheit, T. E., LaVan, D. A., Michael, J. R., Christenson, T. R., and Leith, S. D., *Metallurgical and Materials Transactions A* **33A** (2002) 539-.

8.22. Prasad, S. V., Michael, J. R., and Christenson, T. R. *Scripta Materialia*, **48** (2003) 255-.

8.23. Goods, S.J., Kelly, J.J., Yang, N.Y.C, *Microsystem Technologies* **10** (2004) 498-505.

8.24. Humphreys, F.J., *Journal of Materials Science* **36** (2001) 3833-3854.

8.25. Singer, I.L. *Solid Lubrication Processes*. in *Fundamentals of Friction: Macroscopic and Microscopic Processes*. 1992: Kluwer Academic Publishers, Dordrecht: p. 237-261.

8.26. Scharf, T.S., Private Communication.

Distribution

# Copies	MS	Name	Department
4	MS0889	Prasad, Somuri	1824
1	MS0889	Custer, Jonathan	1824
1	MS0889	Dugger, Michael	1824
2	MS0889	Jungk, John	1824
4	MS0886	Michael, Joseph	1822
1	MS1411	Brewer, Luke	1822
1	MS0886	Kotula, Paul	1822
1	MS0886	Goehner, Ray	1822
4	MS1411	Battaile, Corbett	1814
1	MS1411	Fang, Elliot	1814
1	MS1411	Holm, Elizabeth	1814
1	MS0885	Salzbrenner, Richard	1820
1	MS0885	Johannes, Justine	1810
4	MS9402	Moody, Neville	8759
1	MS9409	Jones, Reese	8776
1	MS9402	Bammann, Doug	8776
1	MS 9402	Chen, Er-Ping	8776
1	MS 9004	Hruby, Jill	8100
1	MS 9402	Lee, Jean	8759
1	MS 9161	Pontau, Art	8750
1	MS 9404	Kwon, Davina	8770
4	MS0824	Hermina,Wahid	1510
1	MS0188	LDRD Office	1030
2	MS0899	Technical Library	4536
2	MS9018	Central Tech Files	8944
1		Majumdar, Bhaskar	New Mexico Institute of Mining and Tech
1	MS0331	Vanecek, Charles W	2619
1	MS0311	Petersen, Daniel E	2614
1	MS0311	Benavides, Gilbert L	2614
1	MS0311	Greenwood, William	2614
1	MS0311	Wild, Ron	2614